Türkiye Bilimler Akademisi GEBİP Ödülü 2. Aktivite Raporu (2011 Aralık-2012 Mayıs)

Yrd. Doç. Dr. İbrahim Burç Mısırlıoğlu

Ferroelektrik ve magnetoelektrik ince filmlerde kaçak akımın ikincil element katkılandırmasına bağlılığı ve $SrTiO_3$ filmlerde elektrokalorik etki: Hesaplamalı ve deneysel çalışmalar

Sabancı Üniversitesi, Mühendislik ve Doğa Bilimleri Fakültesi, Tuzla/Orhanlı 34956

Özet

Bu raporda 2. altı aylık dönemde yürütülen bilimsel çalışmalara ait çıktılar verilmiştir. Rapor son 6 ila aylık süreçte odaklanılan üç çalışma ve bunların sonuçlarına odaklanmıştır. İlk olarak katkılandırılmış $BiFeO_3$ filmlerinde kaçak akım davranışını inceleyen deneysel çalışmayı $SrTiO_3$ ince filmlerin yüksek elektrik alanlar altında elektrokalorik özelliklerine yönelik hesaplamalı diğer bir çalışmanın sonuçları verilmiştir. Üçüncü çalışmamız ise düzlem boyunca paternlenmiş bir $BaTiO_3$ filmin domen yapılarının benzetim yolu ile eldesine yönelik olmuştur. Her üç çalışma da makaleye dönüşen çalışmalar olup basılmış ve basılmakta olan ham halleri ek olarak sunulmuştur. Bunların yanında önceki raporda henüz hakem değerlendirmesinde olan ve geçtiğimiz 6 ay içinde kabul edilip basılmış bir makale de ektedir.

1. Giriş

Son dönemde ferroelektrik ve manyetik iç düzenlenme gösteren malzemelere yönelik büyük bir ilgi oluşmuştur. Burada temel olarak güdülen amaç birbiriyle kristal latis vasıtası ile eşli elektriksel ve manyetik dipollerin konfigürasyonlarını elektrik veya manyetik alanlar sayesinde değiştirmek ve bu yolla çoklu-işlevsel malzemeleri özellikle entegre devrelerde kullanabilmek olmuştur. Bu şekilde "çok durumlu" dijital hafızaların geliştirilmesinin mümkün olabileceği tezi ortaya atılmıştır. Manyetoelektrik diye adlandırılan bu malzemelerde manyetik dipoller ile elektrik dipoller arasında latis deformasyonları aracılığı ile bir eşleşme söz konusudur ve bu eşleşmenin mekanizması ilk defa kuramsal olarak Dzyaloshinkii ve Moriya tarafından yaklaşık 50 yıl kadar önce ortaya konmuştur [1, 2]. Bu çalışmaları sonradan belirtilen türden malzeme sistemlerinin keşfi takip etmiştir. Genellikle perovskit oksit olan bu malzemeler helisel veya sprial türden bir manyetik iç düzenlenmeye sahiptir ve manyetik atomlar arasındaki etkileşimin anisotropisi latiste çok hafif asimetrik atomsal yerdeğiştirmelere sebep olmaktadır [3-4]. İyonik veya kovalen bağlı atomlar arasında çok küçük de olsa belirtilen türden asimetrik yer değiştirmeler elektrik dipollerinin oluşmasını sağlamaktadır. Böylece manyetizmaya bağlı gelişen bir ferroelektrik davranış ortaya çıkmaktadır.

Manyetoelektrik özellik gösteren birçok oksit malzeme içinde $BiFeO_3$ son onyıl içinde en çok ilgiyi gören sistemlerden biri olmuştur [5-14]. Bunun nedeni $BiFeO_3$ kristalinin, yukarıda bahsedilen mekanizmanın yerine ilk olarak yaklaşık 830°C civarında paraelektrik-ferroelektrik geçişini yapması ve soğutma esnasında yaklaşık 280°C

civarında da Fe konumlarında antiferromanyetik düzenlenmeye uğramasıdır. Ferroelektrik ve antiferromanyetik durum arasında bir eşleşme olduğu farklı çalışmalarda dile getirilmiştir ve çok işlevli bileşen kullanımı olarak $BiFeO_3$ birçok araştırma grubunun gündemine girmiştir [5-14]. Ancak bu malzeme sisteminde hem toz halde hem de ince film halinde iken kabul edilemez miktarlarda kaçak akım problemi vardır [14-20]. Çok ideal şartlarda yürütülmüş bazı çalışmalarda $BiFeO_3$'in manyetoelektrik ve faz geçişi özellikleri dile getirilmiştir fakat uygulamaya yönelik üretim ve film büyütme proseslerinde bu türden çalışmaların fazla bir anlamı olmadığı bilinmektedir. Dolayısı ile $BiFeO_3$ sisteminde kaçak akımın düşürülmesi bazı grupların üzerinde çalıştığı bir konu haline gelmiştir. Sabancı Üniversitesi'ndeki grubumuzun Romanya'nın Magurele şehrindeki National Institute of Materials Physics yarı-iletken araştırma grubu ile ortaklaşa yürüttüğü çalışmada $BiFeO_3$ ince filmlerin kaçak akım miktarının Gd katkılandırılması ile bir nebze kontrol edilebileceğinin gösterildiği bir deneysel çalışmamız bu raporun girdilerinden birini oluşturmaktadır. Bu çalışmanın çıktılarının bir kısmı 2012 Nisan ayı içinde makale olarak Applied Physics Letters dergisine gönderilmiş ve kısa sürede hakem değerlendirmesinde olumlu not almıştır, bazı düzeltmelerin ardından basılması beklenmektedir.

Geçtiğimiz rapor döneminde (1. rapor dönemi) hakem değerlendirmesinde olan bir hesaplamalı çalışmamız 2012 Şubat ayında Journal of Applied Physics dergisinde basıma kabul edilmiştir. Bu çalışmanın detayları yine önceki rapor döneminde verilmişti ve bu rapor döneminde makalenin basılmış hali eke konmuştur.

Kısmi zamanlı olarak danışmanlığını yaptığım ve 2006 yılında doktoramı aldığım grupta çalışan Jialan Zhang isimli doktora öğrencisi ile kendisinin 2011 yazında Sabancı Üniversitesi'nde, Prof. G. A. Rosetti ve Prof. S. P. Alpay'ın danışmanlığında yaptığı çalışma da Applied Physics Letters dergisinde basıma kabul edilmiştir. Bu çalışma $SrTiO_3$ ince filmlerin elektrokalorik etkisinin içgerilmelere bağlılığını incelemektedir ve makalenin ham hali raporun ekindedir. Jialan Zhang 2012 yazını da Tübitak bursu ile Sabancı Üniversitesi'nde geçirecek, ferroelektrik-paraelektrik süperlatislerde ısı kapasitesi ve elektrokalorik etkiyi içeren hesaplamalı çalışmalarını devam ettirecektir.

Son olarak Moskova'daki Moscow Institute of Radioengineering, Electronics and Automation'dan araştırma grubu ve Prof. Arkadi P. Levanyuk ile gerçekleştirilen bir benzetim çalışmasından da özetle bahsedilmiştir. Bu çalışma "Düzlem boyunca paternlenmiş ferroelektrik bir filmde domen yapıları" başlığı altında kısaca özetlenmiştir. Bu çalışmada paternlenmiş ferroelektrik filmin karmaşık domen yapıları incelenmiştir ve bazı eğilimler tespit edilmiştir.

2. Yöntem: Deneysel ve Hesaplamalı Çalışmalar:

2.1. $BiFeO_3$ İnce filmlerde ikincil element katkılandırmasının elektriksel özelliklere etkisi

Bu çalışmada ilk raporda detayları verilen döner tabla metodu ile Nb-$SrTiO_3$ iletken tek kristal altlıklar üzerine büyütülen $Bi_{1-x}A_xFeO_3$ (A: Gd, Sm, La) filmlerin yapısal ve elektriksel özellikleri karakterize edilmiştir. Yapısal karakterizasyon deneyleri X-ışınları kırınımı (XRD) ile gerçekleştirilmiştir ve filmlerin altlıklar üzerinde epitaksiyele yakın şekilde büyüdükleri tespit edilmiştir. Nb-$SrTiO_3$ altlıklar filmlerin elektriksel karakterizasyonu için alt elektrotları teşkil etmiştir, bu filmler Romanya'ya

yollanmış ve orada Pt üst elektrotlar kaplanmış ve paternlenmiştir. Elektriksel karakterizasyona uygun hale getirilen numuneler üzerinde kapasitans-voltaj (C-V), kutuplaşma-voltaj (P-V) ve akım-voltaj (I-V) ölçümleri yapılmıştır. P-V ve C-V ölçümlerinde yüksek kaçak akımın varlığının tespiti üzerine I-V ölçümleri üzerine eğilinmiş ve sıcaklığa bağlı I-V ölçümleri sayesinde limit proseslerin tespiti yoluna gidilmiştir. Bu çalışmanın detayları Applied Physics Letters dergisine yollanan makalede (Bkz. Ek) verilmiş olup Sonuçlar ve Tartışma kısmında da kısaca özetlenmiştir.

Filmler için hazırlanan (Metot için Bkz. Rapor 1) çözeltilerden aynı zamanda toz numuneler de elde edilmiştir. Halihazırda toz numunelerin XRD çıktıları ile DTA analizleri yapılmıştır. Burada amaçlanan katkılandırmaya ve katkı elementine bağlı olarak tozların yapılarındaki değişimlerin faz geçiş sıcaklıkları ile kıyaslanması ve latis yapısı-geçiş sıcaklığı arasındaki ilişkinin anlaşılması olmuştur. Gd ve La katkılı $BiFeO_3$ tozlar için yapılan XRD ölçümler, ve DTA analizleri Sonuçlar ve Tartışma kısmında özetlenmiştir.

2.2. Düzlem boyunca paternlenmiş ferroelektrik bir filmde domen yapıları

Bu çalışma esasen Moscow Institute of Radioengineering, Electronics and Automation'dan Prof. Mishina'nın grubunun dielektrik sabiti ayarlanabilir fotonik kristal büyütme çalışmalarının bir ürünü olarak kooperatif olarak ortaya çıkmıştır. Tarafımdan yapılan sayısal benzetimlerde delikli paternlenmiş ve MgO tek kristal altlıklar üzerinde büyütülmüş $BaTiO_3$ ince filmlerin tek bir polarizasyon yönlenmesine sahip olamayacağı ve filmlerin çok karmaşık domen yapılarına ayrışacağı ortaya konmuştur. Bu sebep ile düşünülen "ayarlanabilir dielektrik özellikler" hedefinin tutturulmasının bir nevi güç bir hedef olduğu anlaşılmıştır. Benzetimlerde takip edilen metot ekte Journal of Applied Physics makalesinde tanımlanan sayısal metot ile aynıdır, sadece filmin geometrisi, altlık türü ve film içinde paternlenmiş delikler de hesaba alınmıştır. Çalışılan geometri Şekil 1'de verilmiştir. Film kalınlığı yaklaşık 100 nm olup delik çapları mikron mertebesindedir.

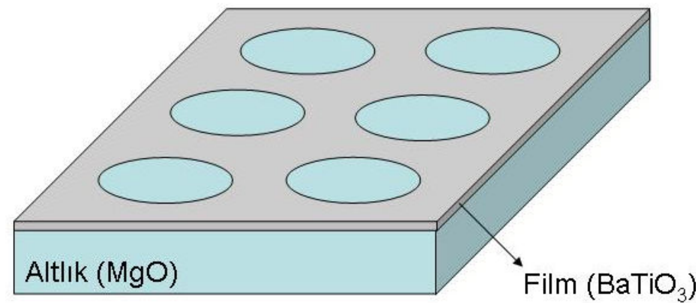

Şekil 1. Delikli paternlenmiş, MgO üzerinde büyütülmüş $BaTiO_3$ film.

2.3. $SrTiO_3$ ince filmlerde elektrokalorik etki

Bu çalışmada Landau-Ginzburg faz geçişleri teorisi kullanılarak $SrTiO_3$ kristalinin farklı içgerilmeler ve sıcaklıklarda göstermesi beklenen elektrokalorik tepkisi hesaplamalı olarak incelenmiştir. $SrTiO_3$ yaklaşık -180°C'de yapısal bir faz geçişi, -

250°C civarında da paraelektrik-ferroelektrik bir faz geçişine uğramaktadır ve bu faz geçiş sıcaklıkları içgerilmelere güçlü şekilde bağlıdır. Bu çalışmada takip edilen metot aşağıdaki gibidir:
(001) atom düzlemleri (001) kübik bir tek kristal altlık üzerine büyütülmüş $SrTiO_3$ film hesaba alınmıştır. Film düzleminde iki yönde eşit olan uyumsuzluk gerilmeleri u_m ve dışarıdan uygulanan elektrik alan E_i, varlığında filmin düzenlenme parametresine bağlı kısmının serbest enerjisi şu şekilde yazılabilir [21]:

$$\begin{aligned} G(P_i, q_i, u_m, E_i, T) = G_0 &+ \tilde{a}_1(P_1^2 + P_2^2) + \tilde{a}_3 P_3^2 + \tilde{a}_{11}(P_1^4 + P_2^4) + \tilde{a}_{33} P_3^4 + \tilde{a}_{12} P_1^2 P_2^2 \\ &+ \tilde{a}_{13}(P_1^2 + P_2^2) P_3^2 + \tilde{b}_1(q_1^2 + q_2^2) + \tilde{b}_3 q_3^2 + \tilde{b}_{11}(q_1^4 + q_2^4) \\ &+ \tilde{b}_{33} q_3^4 + \tilde{b}_{12} q_1^2 q_2^2 + \tilde{b}_{13}(q_1^2 + q_2^2) q_3^2 - \tilde{t}_{11}(P_1^2 q_1^2 + P_2^2 q_2^2) \\ &- \tilde{t}_{33} P_3^2 q_3^2 - \tilde{t}_{12}(P_1^2 q_2^2 + P_2^2 q_1^2) - \tilde{t}_{13}(P_1^2 + P_2^2) q_3^2 \\ &- \tilde{t}_{31} P_3^2 (q_1^2 + q_2^2) - t_{44} P_1 P_2 q_1 q_2 - \tilde{t}_{44}(P_1 P_3 q_1 q_3 + P_2 P_3 q_2 q_3) \\ &+ (C_{11} + C_{12} - 2C_{12}^2 / C_{11}) u_m^2 - E_1 P_1 - E_2 P_2 - E_3 P_3 \end{aligned} \quad (1)$$

Burada G_0 paraelektrik kübik fazın serbest enerjisi, P_i kutuplaşma vektörünün bileşenleri, q_i TiO_6 oktahedrasının dönüşlerini karakterize eden parametre, ve C_{ij} Voigt gösteriminde sabit P_i ve q_i altında elastic sabtilerdir. (1)'de renormalize edilmiş $\tilde{a}_i$ ve $\tilde{a}_{ij}$, $\tilde{b}_i$ ve $\tilde{b}_{ij}$, ve $\tilde{t}_{ij}$ ise şu şekildedir [21]:

$$\tilde{a}_1 = a_1 - \left(g_{11} + g_{12} - 2\frac{C_{12}}{C_{11}} g_{12} \right) u_m, \quad \tilde{a}_3 = a_1 + 2\left(\frac{C_{12}}{C_{11}} g_{11} - g_{12} \right) u_m, \quad (2a)$$

$$\tilde{a}_{11} = a_{11} - \frac{g_{12}^2}{2C_{11}}, \quad \tilde{a}_{33} = a_{11} - \frac{g_{11}^2}{2C_{11}}, \quad (2b)$$

$$\tilde{a}_{12} = a_{12} - \frac{g_{12}^2}{C_{11}}, \quad \tilde{a}_{13} = a_{12} - \frac{g_{11} g_{12}}{C_{11}} - \frac{g_{44}^2}{2C_{44}}, \quad (2c)$$

$$\tilde{b}_1 = b_1 - \left(\lambda_{11} + \lambda_{12} - 2\frac{C_{12}}{C_{11}} \lambda_{12} \right) u_m, \quad \tilde{b}_3 = b_1 + 2\left(\frac{C_{12}}{C_{11}} \lambda_{11} - \lambda_{12} \right) u_m, \quad (2d)$$

$$\tilde{b}_{11} = b_{11} - \frac{\lambda_{12}^2}{2C_{11}}, \quad \tilde{b}_{33} = b_{11} - \frac{\lambda_{11}^2}{2C_{11}}, \quad (2e)$$

$$\tilde{b}_{12} = b_{12} - \frac{\lambda_{12}^2}{C_{11}}, \quad \tilde{b}_{13} = b_{12} - \frac{\lambda_{11}\lambda_{12}}{C_{11}} - \frac{\lambda_{44}^2}{2C_{44}}, \quad (2f)$$

$$\tilde{t}_{11} = t_{11} + \frac{g_{12}\lambda_{12}}{C_{11}}, \quad \tilde{t}_{33} = t_{11} + \frac{g_{11}\lambda_{11}}{C_{11}}, \quad (2g)$$

$$\tilde{t}_{12} = t_{12} + \frac{g_{12}\lambda_{12}}{C_{11}}, \quad \tilde{t}_{13} = t_{12} + \frac{g_{12}\lambda_{11}}{C_{11}}, \quad (2h)$$

$$\tilde{t}_{31} = t_{12} + \frac{g_{11}\lambda_{12}}{C_{11}}, \quad \tilde{t}_{44} = t_{44} + \frac{g_{44}\lambda_{44}}{C_{44}}, \quad (2i)$$

Bu ilişkilerde sırası ile a_i ve a_{ij}, b_i ve b_{ij}, ve t_{ij} gerilimsiz ve tek domen halindeki dielektrik sıkılık sabitleri, yapısal düzenlenme parametersi, permitivite sabitleri, ve P_i ile q_i arasındaki eşleşme sabitleridir. Voigt gösteriminde g_{ij} elektrostriktif sabitleri ve λ_{ij} ise şekil değişimi ile q_i arasındaki eşleşme sabitleridir. (1) ve (2) numaralı ilişkiler kullanılarak $\partial G/\partial P_i = 0$ ve $\partial G/\partial q_i = 0$ durum denklemleri E_i=0 altında elde edilmiştir. STO için fenomenolojik değerler 21 numaralı kaynaktan alınmıştır. Yapılan çalışma sonunda tek domen epitaksiyel STO için $u_m - T$ faz diyagramı elde edilmiştir (Bkz. Pertsev'in çalışması, Kaynak 21). Bu faz diyagramında mümkün olan fazlar ve düzenlenme parametreleri şu şekildedir: HT (High temperature phase/Yüksek sıcaklık fazı): $P_1=P_2=P_3=0$, $q_1=q_2=q_3=0$; ST (Structural order only/Sadece yapısal düzenlenme): $P_1=P_2=P_3=0$, $q_1=q_2=0$, $q_3\neq 0$; FTI (Ferroelectric tetragonal phase 1/Ferroelektrik tetragonal faz 1): $P_1=P_2=0$, $P_3\neq 0$, $q_1=q_2=q_3=0$; FTII (Ferroelectric tetragonal phase 2/Ferroelektrik tetragonal faz 2): $P_1=P_2=0$, $P_3\neq 0$, $q_1=q_2=0$, $q_3\neq 0$; FOI (Ferroelectric orthorhombic phase/Ferroelektrik ortorombik faz): $|P_1|=|P_2|\neq 0$, $P_3=0$, $q_1=q_2=q_3=0$. Sonrasında adyabatik sınırda ferroelektrik faz için ΔT olan sıcaklık değişimi şu şekilde hesaplanabilir [22] (Detaylar için Bkz. Ek):

$$\Delta T(T, E_i, u_m) = \sum_{i=1}^{3}\left(- \int_{E_a}^{E_b} \frac{T}{C_E^0(T, E_i, u_m)} \left(\frac{\partial P_i^0(T, E_i, u_m)}{\partial T} \right)_{E_i} dE_i \right) \quad (3)$$

ve burada $P_i^0(T, E_i, u_m)$ denge kutuplaşma, ile denge yapısal düzenlenme parametresi $q_i^0(T, E_i, u_m)$ durum denklemlerinden elde edilmiştir. E_a ve E_b elektrik alan aralığını vermektedir ve $\Delta E = \tilde{E}_a - E_b$. (3) numaralı denklemde verilen hacimsel özgül ısı, yani $C_E^0(T, E_i, u_m)$ latisten olan katkının deneysel ölçümlerinden alınmıştır ve arka plan latis ısı kapasitesi datasını da içermektedir. Bu bilgi de 23 numaralı kaynaktan edinilmiştir ve hesaplara alınmıştır. Yukarıda tanımları verilen fazların 1 ve 2 numaralı denklemler vasıtası ile hesaplanmış kararlılık diyagramı Şekil 2'dedir. Burada içgerilmelerin esasen film kalınlığına bağlı olarak değişmekte olduğu düşünüldüğünde Kaynak 24'te verilen "efektif iç gerilme" parametresi olarak da düşünülebilir.

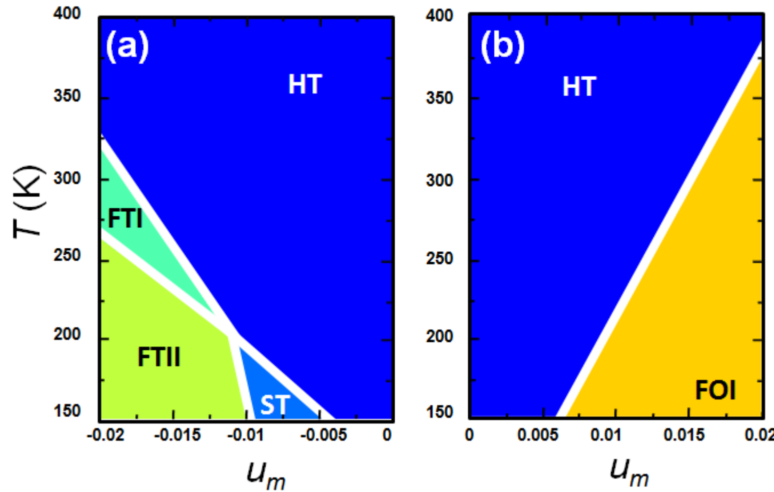

Şekil 2. (a) Düzlemle baskı gerilmeleri için ve (b) çekme gerilmeleri için hesaplanmış sıcaklık-iç gerilme faz kararlılık diyagramı. En yüksek elektrokalorik etki HT-FT, yani kübik-polar faz geçişlerinde gözlemlenmektedir.

3. Sonuçlar ve Tartışma

3.1. $BiFeO_3$ İnce filmlerde ikincil element katkılandırmasının elektriksel özelliklere etkisi

Bu çalışmada yoğun bir deneysel gayretin varolması sonuçların diğer çalışmalara gore daha detaylı sunumunu gerektirmiştir. C-V eğrileri verilen filmlerde baskın bir kaçak akım davranışı olduğunun kesinleşmesi üzerine aynı filmler üzerinde akım-voltaj (I-V) ölçümleri gerçekleştirilmiştir. Bu ölçümler ayrıca sıcaklığa bağlı olarak da yapılmıştır. Bunun sebebi ise kaçak akım mekanizmasının aktivasyon enerjisi hakkında fikir edinmektir. Nb-$SrTiO_3$ altlıkla üzerinde büyütülmüş saf filmlerin temsili I-V ölçümü sonuçları Şekil 2'de verilmiştir. Saf ve katkılandırılmış filmler üzerinde sıcaklığa bağlı olarak yapılan ölçümlerin film içindeki kaçak akım oluşum mekanizmalarına ışık tutması beklenmiştir ve bu konuda literatürde bilinmezlikler göze çarpmıştır. Örneğin filmlerde Schottky türü kaçak akım ile uzay yükü kontrollü akımların (Space charge limited currents) aktivasyon enerjileri farklıdır: Schottky türü kaçak akım mekanizmaları sıcaklıkla üstel bir değişim gösterirken uzay yükü kontrollü akımlarda sıcaklığa bağlı çok belirgin bir değişim olmamaktadır. İkinci durumda kaçak akım özellikle kalınlığa bağlı hale gelmektedir. Safsızlıkların olduğu yalıtkan kristallerde bir diğer "iletkenlik" mekanizması da Poole-Frenkel mekanizmasıdır. Bu türden bir iletkenlik oluşumunda sıcaklığa güçlü şekilde bağlılık yoktur ve iletkenlik daha ziyade uygulanan elektrik alan ve yük taşıyıcıların safsızlık atomlarındaki "boş durumlar (empty states)"ı kullanarak kristal içinde ilerlemesi ile ortaya çıkar. Gd katkılı filmler üzerinde yapılan I-V ölçümlerinin sonuçları ilerleyen kısımlarda verilmiştir.

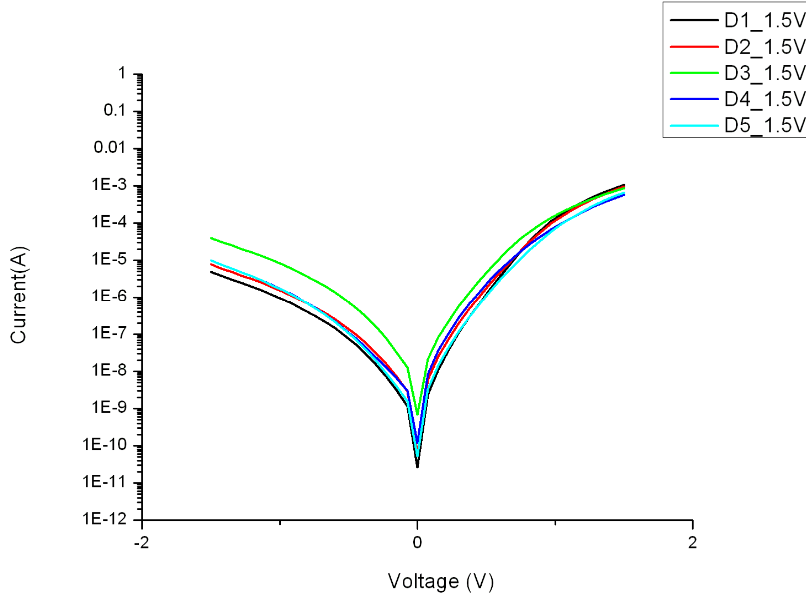

Şekil 3. Nb-$SrTiO_3$ altlıklar üzerine büyütülmüş $BiFeO_3$ filmin oda sıcaklığında I-V davranışı. Farklı D değerleri (örneğin D1, D2 vb.) farklı kontak noktalarında yapılmış ölçümlere işaret etmektedir.

I-V ölçümlerinde özellikle Gd katkılı filmlere ayrı bir önem verilmiştir. Bunun sebebi ise Gd'un latis içinde çözündüğü andan itibaren 7/2 toplam spin sayısına sahip olmasıdır ki bu gayet büyük bir atomik manyetik momente denk gelmektedir. Yani Gd iyonu $BiFeO_3$ içinde manyetik bir iyondur ve spin-spin saçılmasının kaçak akıma karşı bir direnç oluşturabileceği düşünülmüştür. Eğer latis içinde La, Gd ve Sm gibi Bi iyonu ile yakın boyutlara sahip atomların valans enerji seviyelerine ve elektron dizilimlerine bakacak olursak:

La: [Xe] $5d^1$ $6s^2$
Gd: [Xe] $4f^7$ $5d^1$ $6s^2$
Sm: [Xe] $6s^2$ $4f^6$

Gd iyonunun 7/2 spinine bağlı manyetik momenti Hund kuralına göre ayrı ayrı paralel şekilde yönlenen 4f bandı elektronlarından gelmektedir. Bilindiği üzere, kristaller içinde iletkenliği zorlaştıran etkenlerden en iyi bilinenleri latisteki deformasyonlar, yapısal hatalar, yüklü iyonlar, rasgele atom dizilimi ve manyetik safsızlıklar olarak sıralanabilir. Yukarıda Gd için olan manyetik momentin kaçak akıma belirli bir engel oluşturacağı düşünülmüştür ancak oda sıcaklığı ölçümlerinden net bir kanıt elde edilememiştir. Bunun üzerine Gd elementinin sıcaklığa bağlı I-V ölçümleri yapılmıştır. Yine özellikle Gd üzerinde durulmasının sebebi bu iyonun manyetik yapısının kaçak akıma bir etkisi olup olmadığının anlaşılması olmuştur. Bu ölçümleri La ve Sm katkılı filmler üzerindeki ölçümlerin takip etmesi planlanmaktadır. Bu katkı elementlerinin kaçak akımı düşürdüğü üzerine raporlarla karşılaşılmıştır.

I-V ölçümlerinde sıcaklığa bağlı davranış genellikle farklı aktivasyon enerjilerinin belirlenmesine yönelik kullanışlı veriler sağlar. Üçüncü altı ayda bu yönde girişimler yapılmıştır ve katkılandırmanın elektrot-film arayüzeyindeki "bariyer" yüksekliğini bulmak ana motivasyon olmuştur. Sıcaklığa bağlı I-V ölçümleri Gd katkılı filmlerden önce saf $BiFeO_3$ filmleri için yapılmıştır. Saf $BiFeO_3$ için sıcaklıpa bağlı yapılmış I-V ölçümlerine güzel bir örnek Şekil 4'tedir.

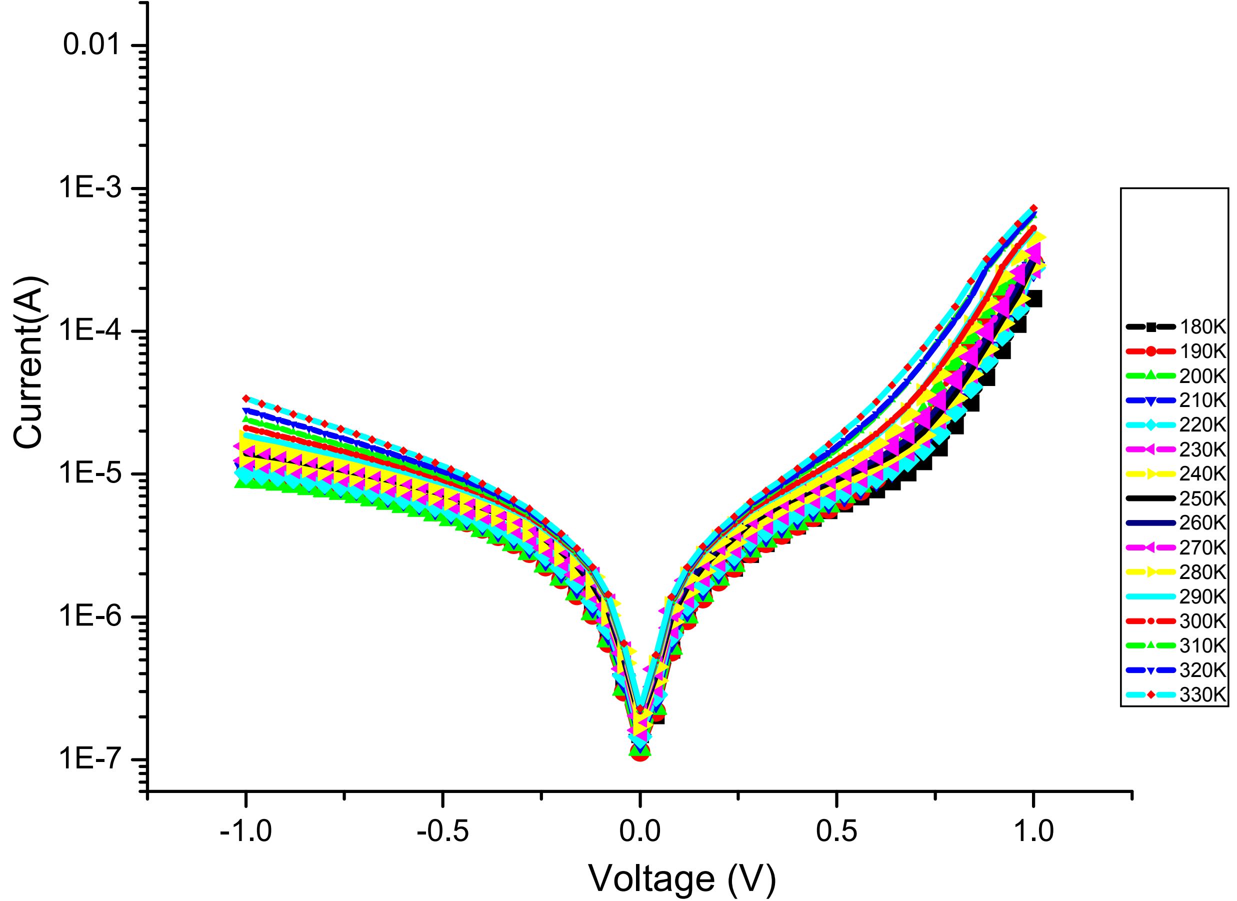

Şekil 4. Saf $BiFeO_3$ filmi üzerinde yapılan sıcaklığa bağlı I-V ölçümleri. Her iki voltaj polaritesinde de 330K'den 180K' e inildiğinde kaçak akımda yaklaşık 10 kat azalma gözlemlenmiştir. Pozitif polaritede kaçak akım miktarı negatife göre daha yüksektir.

Saf $BiFeO_3$ filmleri için ölçülen kaçak akım miktarları oldukça yüksektir. Ferroelektrik dipollerin kutuplaşmasının ölçülebilmesi için kaçak akıma bağlı yük miktarının dipol kutuplaşmasına bağlı yük yoğunluğundan çok daha az olması beklenir. Bunun da ötesinde kaçak akımın yüksek olması film içinde veya arayüzeylerde etkili bir iletkenlik mekanizmasının varlığına işaret etmektedir. Pozitif voltaj polaritesinde akımın çok daha yüksek olması bir diyot (diode) davranışı gibi gözükse de eldeki aktivasyon enerjisi verileri Schottky türü bir iletkenliğe uymamaktadır. Bu konu halen üzerinde çalışılan bir noktadır.

%5 ve %10 Gd katkılı $BiFeO_3$ filmlerin I-V ölçüm sonuçları aşağıda (Şekil 5-6) verilmiştir.

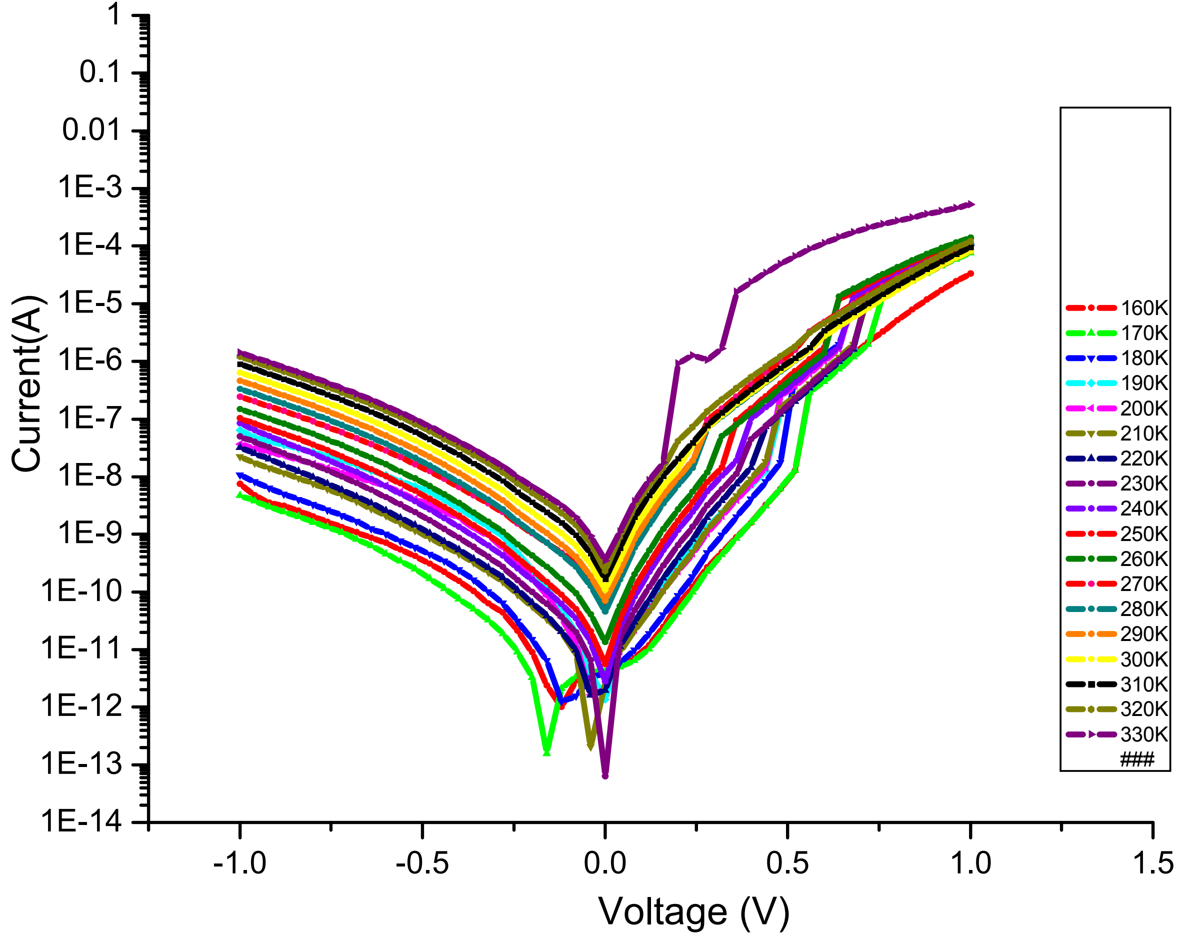

Şekil 5. %5 Gd katkılı $BiFeO_3$ film için sıcaklığa bağlı I-V eğrileri. Ölçümler 160K ile 330K arasında yapılmıştır.

Şekil 4 ile 5 kıyaslandığında Gd katkılı $BiFeO_3$ filmin kaçak akım miktarının, özellikle düşük sıcaklıklarda, belirgin şekilde azaldığı görülmektedir. Fakat Gd katkılı filmlerde de negatif ve pozitif polarite iletkenliğinde bir asimetri göze çarpmaktadır ki bunun yine üst-alt elektrot asimetrisinden kaynaklandığı yüksek ihtimaldir. Gd katkısının artırılması ile I-V davranışında sıcaklığa bağlı muhtemel değişimi görmek için yapılan %10 Gd katkılı filmin sonuçları Şekil 5'tedir.

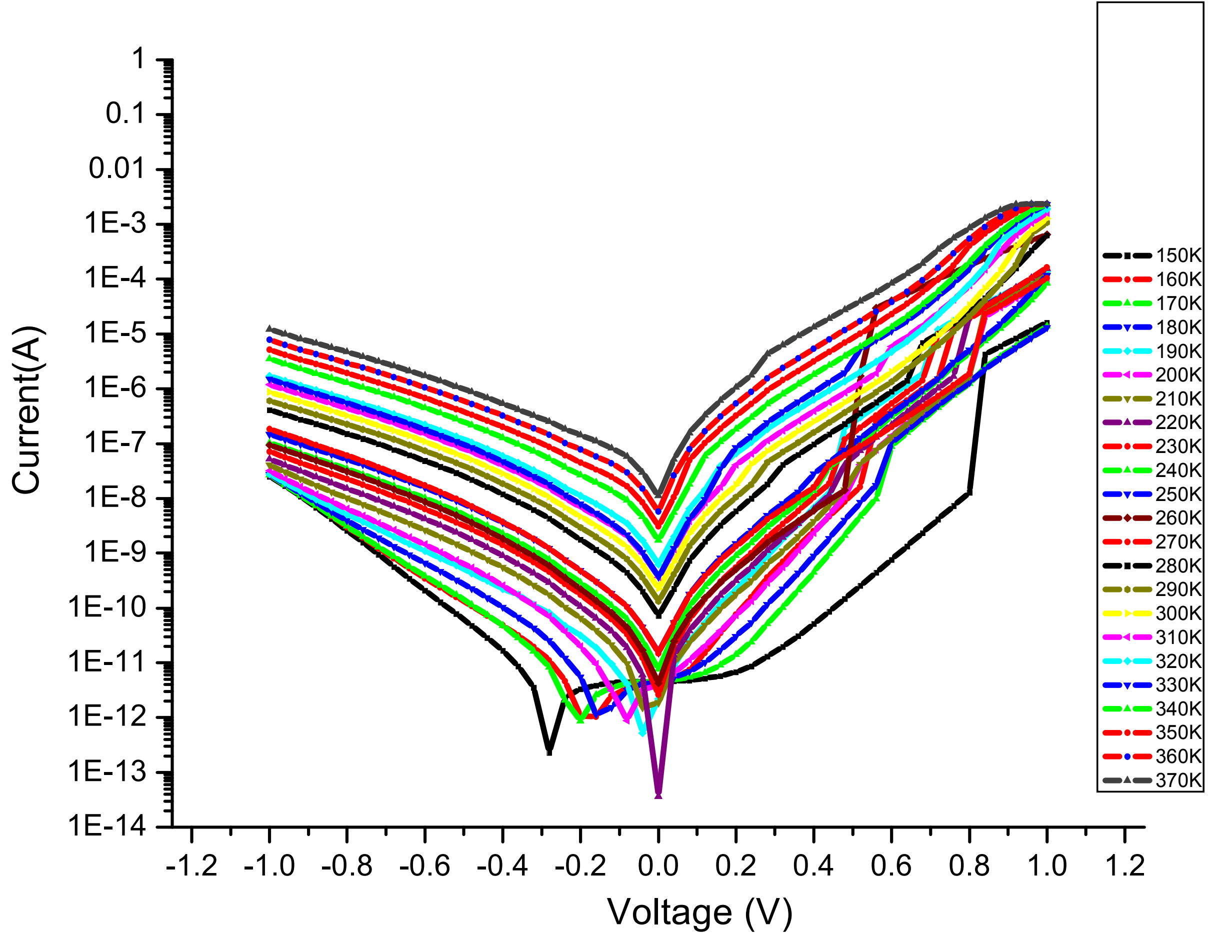

Şekil 6. %10 Gd katkılı $BiFeO_3$ filmin sıcaklığa bağlı I-V davranışı.

%10 Gd katkılı $BiFeO_3$ filminde %5'e göre çok belirgin bir kaçak akım azalması tespit edilmemiştir, bunun için yeni ölçümler ile bu eğilimin teyit edilmesi gerekmektedir. Saf ve katkılı filmlerin pozitif ve negatif polaritelerdeki sıcaklığa bağlı akım değerlerinden muhtemel iletkenlik mekanizmasının aktivasyon enerjisi için hesaplamalar raporun teslim etme tarihinden kısa süre içinde başlamıştır. Bunun yanında araştırmalarımız sırasında bulunan bir makalede Nb-$SrTiO_3$ altlıklar üzerine büyütülmüş ve Pt üste elektrodu ile temaslanmış saf $BiFeO_3$ filmlerin proses esnasında Bi kaybına uğradığı (Bi uçucu bir elementtir) ve buna bağlı olarak da bir nevi diyot gibi davranabileceği rapor edilmiştir [14-20]. Bu yayınlardaki bulgulara gore $BiFeO_3$ Bi kaybını takiben p-tipi bir geniş-bant yarıiletken gibi davranmaktadır. Benzer bir çalışmayı farklı Gd katkılandırması oranlarında grubumuz da yürütmüş ve sonucunda Applied Physics Letters dergisine yollanan bir makale çıkmıştır (Bkz Ek). Makale olumlu tepki görmüştür ve istenen düzeltmeler yapıldıktan sonra yeniden değerlendirmeye yollanmıştır.

3.2. Düzlem boyunca paternlenmiş ferroelektrik bir filmde domen yapıları

Ferroelektrik ve manyetik yapılarda Maxwell denklemlerinin sağlanması önemli noktalardan birini teşkil etmektedir ve malzemenin makroskopik davranışını belirleyici olmaktadır. Bu çalışmada esas olarak ortaya konan sonuç paternlenmiş bir ferroelektrik kristalin son derece karmaşık ancak kararlı bir elektriksel domen yapısına erişeceği ve ferroelektrik dipollerin film düzlemi boyunca peryodik olarak açılmış deliklere paralel bir konfigürasyona gitmek isteyeceğidir. Kutuplaşmayı bastırıcı alanın şiddeti nedeni ile benzetimlerde elde edilen dipol konfigürasyonlarının dışarıdan uygulanan bir elektrik alan vasıtası ile bozulması çok zor gözükmektedir. Çalışma bu açıdan paternlenmiş ferroelektrik kristallerin muhtemel fotonik kristal uygulamalarında son derece "tahmin edilemeyen veya kontrol edilemeyen" özelliklere sahip olacağına dair bir gayret olarak kalmıştır. Bu çalışma fiziksel açıdan domen yapılarının nasıl karmaşık şekillerde olabileceğini ve paternlenmiş delik sayısı ile film boyutlarına nasıl kuvvetle bağlı olduğunu göstermiştir. Bu çalışmanın detayları Physics of the Solid State dergisine yollanmış makalemizde anlatılmıştır (Bkz. Ek).

3.3. $SrTiO_3$ ince filmlerde elektrokalorik etki

Bu çalışmada özet olarak $SrTiO_3$ ince filmlerin uyumsuzluk gerilmeleri altında sıcaklığa ve uygulanan elektrik alanın şiddetine gore elektrokalorik tepkileri hesaplanmıştır. Detayları önceki kısımda verilen bir Landau-Ginzburg-Devonshire potansiyelinden elde edilen durum denklemleri sıcaklığa, uyumsuzluk gerilmelerine ve farklı kristal oryantasyonlarında uygulanan elektrik alan değerlerine bağlı olarak çözümlenmiştir. Film düzlemi boyunca baskı içgerilmelerinin valığında elektrokalorik etkinin sandviç kapasitör geometrisinde metal-dielektrik-metal bir sistemde Şekil xx'de haritada belirtilen HT-FTII faz geçişi civarında en yüksek değere ulaştığı tespit edilmiştir. Yaklaşık 1000 kV/cm elektrik alan değerlerinde 5K kadar sıcaklık değişimlerinin oluşabileceği hesaplanmıştır. Düzlem boyunca çekme gerilmelerine sahip filmlerde de parmak elektrot geometrisi altında HT-FOI geçişi civarında, yani kübik fazdan polar ortorombik faza geçişte yüksek elektrokalorik etki edle edilebileceği öngörülmüştür.

Kaynakça

1. Dzyaloshinskii I., Soviet Physics JETP 10, 628, (1959),
2. Moriya T., Physical Review 120, 91 (1960).
3. Katsura H., Nagaosa N. and Balatsky A. V., "Spin current and magnetoelectric effect in noncollinear magnets", Physical Review Letters, 95, 057205, 2005.
4. Katsura H., Balatsky A. V. and Nagaosa N., "Dynamical magnetoelectric coupling in helical magnets", Physical Review Letters, 98, 027203, 2007.
5. Fiebig M., Lottermoser Th., Frohlich D., Goltsev A. V. and Pisarev R. V.,"Observation of coupled electrical and magnetic domains", Nature, 419, 818-820, 2002.
6. Zhao T., Scholl A., Zavaliche F., Lee K., Barry M., Doran A., Cruz M. P., Chu Y. H., Ederer C., Spaldin N. A., Das R. R., Kim D. M., Baek S. H., Eom C. B. and

Ramesh R., "Electrical control of antiferromagnetic domains inmultiferroic BiFeO3 films at room temperature", Nature, 5, 823-829, 2006.

7. Yaing-Hao Chu, Lane W. Martin, Mikel B. Holcomb, Martin Gajek, Shu-Jen Han, Qing He, Nina Balke, Chan-Ho Yang, Donkoun Lee, Wei Hu, Qian Zhan, Pei-Ling Yang, Arantxa Fraile-Rodr´iguez, Andreas Scholl, Shan X. Wang, R. Ramesh, "Electric-field control of local ferromagnetism using a magnetoelectric multiferroic", Nature Materials, 7, 478-482, 2006.
8. Scott J. F., "Multiferroic Memories", Nature Materials, Vol. 6, 256-257, 2007.
9. Sang-Wook Cheong and Maxim Mostoyov, "Multiferroics: A magnetic twist for ferroelectricity", Nature Materials, 6, 13-20, 2007.
10. Tokura Y., "Multiferroics-toward strong coupling between magnetization and polarization in a solid", Journal of Magnetism and Magnetic Materials, 310, 1145-1150, 2007.
11. Ramesh R. and Spaldin N., "Multiferroics: Progress and prospects in thin films", Nature Materials, Vol. 6, 21-29, 2007.
12. Chiba D., Sawicki M., Nishitani Y., Nakatani Y., Matsukura F., Ohno H., "Magnetization vector manipulation by electric fields", Nature, 455, 515-518, 2008.
13. Martin L. W., Crane S. P., Chu Y.-H, Holcomb M. B., Gajek M., Huijben M., Yang C.-H Balke, N. and Ramesh R., "Multiferroics and magnetoelectrics: Thin films and nanostructures", Journal of Physics: Condensed Matter, 20, 434220-13, 2008.
14. Catalan G., Scott J. F., Physics and Applications of Bismuth Ferrite, Advanced Materials, 21, 2463-2485, (2009).
15. Yakovlev S., Zekonyte J., Solterbeck C.-H., Es-Souni M., Interfacial effects on the electrical properties of multiferroic BiFeO3/Pt/Si thin film heterostructures, Thin Solid Films, 493, 24-29 (2005) and YAKOVLEV S., Solterbeck C.-H., Kuhnke M., and Es-Souni M.,"Multiferroic $BiFeO_3$ films processed via chemical solution deposition: Structural and electrical characterization", Journal of Applied Physics, 97, 094901-6, (2005).
16. Clark S. J., Robertson J., Band gap and Schottky barrier heights of multiferroic $BiFeO_3$, Applied Physics Letters, 90, 132903-3, (2007).
17. Fruth V., Popa M., Calderon-Moreno J. M., Anghel E. M., Berger D., Gartner M., Anastasescu M., Osiceanu P., Zaharescu M., Chemical solution deposition and characterization of BiFeO3 thin films, Journal of the European Ceramic Society 27, 4417-4420 (2007).
18. Pintilie L., Dragoi C., Chu Y.H., Martin L.W., Ramesh R., Alexe M., Orientation-dependent potential barriers in case of epitaxial Pt-BiFeO(3)-SrRuO(3) capacitors, Applied Physics Letters, 94, 232902-3, (2009).
19. Qu T. L., Zhao Y. G., Xie D., Shi J. P., Chen Q. P., Ren T. L., Resistance switching and white-light photovoltaic effects in $BiFeO_3$/Nb-$SrTiO_3$ heterojunctions, Applied Physics Letters, 98, 173507-3, (2011).
20. Yang H., Luo H.M., Wang H., Usov I.O., Suvorova N.A., Jain M., Feldmann D.M., Dowden P.C., DePaula R.F., Jia Q.X., Rectifying current-voltage characteristics of BiFeO3/Nb-dopedSrTiO3 heterojunction, Applied Physics Letters, 92, 102113-3 (2008).

21. Pertsev N. A., Tagantsev A. K., and Setter N., Phase transitions and strain-induced ferroelectricity in SrTiO3 epitaxial thin films, Physical Review B **61**, R825 (2000).
22. Zhang J., Heitmann A. A., Alpay S. P., and Rossetti G. A. Jr., Electrothermal properties of perovskite ferroelectric films, Journal of Materials Science. **44**, 5263.
23. Ligny D. Ligny and Richet P., High-temperature heat capacity and thermal expansion of $SrTiO_3$ and $SrZrO_3$ perovskites, Physical Review B **53**, 3013 (1996).
24. Speck J. S., Seifert A., Pompe W., and Ramesh R., Domain configurations due to multiple misfit relaxation mechanisms in epitaxial ferroelectric thin films 2: Experimental verification and implications Journal of Applied Physics **76**, 466 (1994).

3. Bilimsel Yayınlar ve Konferans Katılımları (2011 Aralık- 2012 Mayıs)

Bilimsel Yayınlar:

- I. B. Misirlioglu, H. N. Coloğlu and M. Yildiz, "Thickness Dependence of Stability of Electrical Domains in Ferroelectric Films with Depletion Charge" Journal of Applied Physics (2012).
- J. Zhang, I. B. Misirlioglu, G. A. Rosetti and S. P. Alpay, "Electrocaloric Properties of Epitaxial Strontium Titanate Films", Applied Physics Letters dergisinde basıma kabul edildi.
- H. Khassaf, C. Dragoi, I. Pintilie, I. B. Misirlioglu and L. Pintilie, "Potential barrier engineering via Gd doping of $BiFeO_3$ layers in Nb:$SrTiO_3$-$BiFeO_3$-Pt structures displaying diode-like behavior", Applied Physics Letters, hakem değerlendirmesinden olumlu sonuç alındı, düzeltme aşamasında.
- E. Mishina, A. Sigov, I. B. Misirlioglu and A. P. Levanyuk, "Effects of depolarizing field in perforated film of two-axial ferroelectric", Physics of the Solid State dergisinde basım için değerlendirilmekte.

Konferans Katılımları:

- Konuşmacı olarak katılımcı: "Dramatic effect of the near-electrode configurations on the phase transition characteristics of ferroelectric-paraelectric superstructures", A. P. Levanyuk, I. B. Misirlioglu. American Physical Society March Meeting, Boston, 2012.
- Materials Research Society Fall 2012 Meeting in Boston konferansına olumlu tepki almış "Potential barrier engineering via Gd doping in $BiFeO_3$ films displaying diode-like behavior" başlıklı bir adet özet sunum için gönderilecektir. Bu sunumun içeriği değerlendirmede olan Applied Physics Letters Makalesinin içeriği ile yaklaşık aynıdır (Bkz. Ek).
- Materials Research Society Fall 2012 Meeting in Boston konferansına "Dramatic Reduction in the Paraelectric-Ferroelectric Phase Transition Temperature of $BiFeO_3$ upon A-site Doping" başlıklı bir adet özet sunum için gönderilecektir. Bu çalışma henüz tamamlanmamıştır ancak eldeki mevcut bilgiler ile bir resim ortaya çıkmaya başlamış, özet oluşturulmuş ve bu özet aşağıda verilmiştir.

Dramatic Reduction in the Paraelectric-Ferroelectric Phase Transition Temperature of $BiFeO_3$ upon A-site Doping

H. Khassaf [1], M. Khodabakhsh [1], I. B. Misirlioglu [1], E. M. Alkoy [2] and S. Alkoy [3]
M. A. Gulgun [1]

[1] *Faculty of Engineering and Natural Sciences, Sabanci University, Tuzla/Orhanli 34956 Istanbul, Turkey*
[2] *Faculty of Engineering, Maltepe University, 2011 Marmara Eğitim Köyü 34857 Maltepe, İstanbul, Turkey*
[3] *Materials Science and Engineering Department, Gebze Institute of Technology, Cayirova, 41400 Gebze, Kocaeli, Turkey*

Abstract

Pure and doped $Bi_{1-x}A_xFeO_3$ (A: La, Sm, Gd) powders have been prepared following a metalorganic precursor method at various dopant concentrations. Dopants with smaller ionic radii that go to A-sites in the perovskite structure of $BiFeO_3$ have a dramatic impact on the phase transition temperatures determined by differential thermal analysis. There is a direct correlation between the ionic radius and the extent of reduction in the transition temperature for a given dopant concentration. While our Scanning Electron Microscope observations indicate that the dopants with smaller radius than Bi (Sm and Gd) inhibit grain growth even at small concentrations (<5%), the grain size for all doped powders is still well above the limits where apparent size effect in powders are reported by prior works for similar systems. Thus we rule out the size effect in doped $BiFeO_3$ powders as the driving force behind the reduction in the phase transition temperatures. The room temperature X-ray diffraction patterns indicate a shift of the rhombohedral $BiFeO_3$ lattice towards a cubic state with slight peak broadening for samples doped with Sm and Gd while this effect is minimal in powders doped with La, concurrent with the thermal analysis results. We explain the dramatic reduction in the transition temperatures of doped $BiFeO_3$ with local lattice strains around unitcells containing dopants that create gradients in polarization. It is quantiatively well understood that polarization gradients are the source of depolarizing fields, which can drastically suppress the paraelectric-ferroelectric transition temperature even in grains much above the reported critical sizes. We conclude that even small concentrations of dopants in $BiFeO_3$ can apparently suppress ferroelectricity through the long-range Coulomb interactions especially when the dopant ionic radius is less than that of Bi, capable of creating local lattice strains.

4. Gelecek Dönemde Planlanan Aktiviteler

Aralık 2011-Mayıs 2012 dönemi içinde bir adet Tübitak 1001 projesi ve bir adet de Türkiye-Romanya ikili işbirliği projesi sunulmuştur. Bunun yanında kollaborasyon yaptığım Profesör Arkadi P. Levanyuk'un Sabancı Üniversitesi'nde yaklaşık 2 aylık bir araştırma kalışı için Tübitak 2221 Konuk Bilim İnsanı destekleme programına başvurulmuştur ve bu başvuru başarı ile sonuçlanmıştır. Önümüzdeki dönemde bilimsel aktivitelerin bir kısmının, kabul edilmesi halinde, bahsedilen projelerin içeriğine yönelik olması beklenmektedir. Bunun yanında henüz başlamış olan ve aşağıda belirtilen aktiviteler de devam edecektir. Bu aktiviteler şunlardır:

- Katkılandırılmış ve sol-jel metodu ile sentezlenmiş $BiFeO_3$ tozlarının faz geçişi sıcaklıklarının katkılandırma türüne ve miktarına göre tespiti ve değişimlere sebep olan mekanizmaların anlaşılması. Bu konuda eldeki veriler yadımı ile bir adet makalenin yazımına başlanmıştır (Özet için Bkz. Ek).
- Katkılandırılmış $BiFeO_3$ taneciklerinde katkı elementi dağılımının geçirimli elektron mikroskobu (TEM) yardımı ile incelenmesi (Max Planck Institute of Microstructure Physics Halle'de Prof. Dietrich Hesse'nin grubu ile kollaborasyon içinde gerçekleştirilmesi öngörülmüştür).
- Çok ince ferroelektrik filmlerde dinamik uzay yüklerinin histerisiz eğrileri ve dielektrik sabiti üzerindeki etkilerinin hesaplamalı olarak incelenmesi.
- Çok katmanlı ferroelektrik-dielektrik yapılarda dielektrik sabitinin tabaka sayısına bağlı olarak davranışının hesaplamalı olarak incelenmesi.
- $KNbO_3$ filmlerinin yapısal ve elektriksel özelliklerini incelemeyi konu alan bir adet Tübitak 1001 projesi gönderilmiştir (Mart 2012). Bu projenin kabul edilmesi halinde bu yönde aktivitelerin başlaması beklenmektedir.
- Prof. Arkadi P. Levanyuk'un Sabancı Üniversitesi'nde 2 ay süre ile kalışı için Tübitak'tan 2221 Konuk Bilim İnsanı Ağırlama Programı'ndan destek alınmıştır ve bu kalış sırasında ferroelektrik-paraelektrik süperlatislerin düşük sıcaklık domen yapıları ve faz geçişi anomalileri üzerine çalışmalar öngörülmektedir.

5. Yayınlar (Basımda olan veya yeni kabul edilmiş makaleler verilmemiştir)

1. **Misirlioglu I. B.**, Cologlu H. N. & Yildiz M. (2012), "Thickness driven stabilization of saw tooth-type domains in ferroelectric films with depletion charge", Journal of Applied Physics, **111**, 064105 (Atıf sayısı: 0).

2. **Misirlioglu I. B.** & Yildiz M. (2012), "Polarization Retention and Switching in Ferroelectric Nano Capacitors with Defects on Tensile Substrates", Solid State Electronics, **67**, 38 (Atıf sayısı: 0).

3. Levanyuk A. P.& **Misirlioglu I. B.** (2011), "Phase transitions in ferroelectric-paraelectric superlattices", Journal of Applied Physics, **110**, 114109 (Atıf sayısı: 0).

4. **Misirlioglu I. B.**, Okatan M. B.& Alpay S. P. (2011), "Effect of Asymmetrical Interface Charges on the Hysteresis and Domain Configurations of Ferroelectric Thin Films", Integrated Ferroelectrics, **126**, 142 (Atıf sayısı: 0).

5. Okatan, M. B., **Misirlioglu, I. B.**, Alpay, S. P. (2010) Contribution of space charges to the polarization of ferroelectric superlattices and its effect on dielectric properties. Phys. Rev. B **82**, 094115 (Atıf sayısı: 4).

6. **Misirlioglu, I. B.**, Okatan M. B. & Alpay, S. P. (2010) Asymmetric hysteresis loops and smearing of the dielectric anomaly at the transition temperature due to space charges in ferroelectric thin films. J. Appl. Phys. **108**, 034105 (Atıf sayısı: 4).

7. **Misirlioglu, I. B.**, Pintilie, L., Alexe, M., & Hesse, D. (2009) Influence of long-range dipolar interactions on the phase stability and hysteresis shapes of ferroelectric and antiferroelectric multilayers. DOI 10.1007/s10853-009-3451-6, special issue of J. Mat. Sci. (Atıf sayısı: 3).

8. **Misirlioglu, I. B.** (2009) Stability of a ferroelectric phase with electrical domains in multilayers, Appl. Phys. Lett. **94**. 172907 (Atıf sayısı: 3).

9. Geske, L., **Misirlioglu, I. B.**, Vrejoiu, I., Alexe, M. & Hesse, D. (2009) Impact of misfit relaxation and a-domain formation on the electrical properties of tetragonal Pb $Zr_{0.4}$ $Ti_{0.6}O_3$ / Pb $Zr_{0.2}$ $Ti_{0.8}O_3$ thin film heterostructures: Experiment and theoretical approach. J. Appl. Phys. **105**, 061607 (Atıf sayısı: 9).

10. Akcay, G., **Misirlioglu, I. B.** & Alpay, S. P. (2009) Phase transformation characteristics of Barium Strontium Titanate films on anisotropic substrates with (110)//(001) epitaxy. Integ. Ferro. **101**, 29 (Atıf sayısı: 0).

11. **Misirlioglu, I. B.**, Akcay, G. & Alpay, S. P. (2009) Low-temperature monoclinic phase in epitaxial (001) Barium Titanate on (001) cubic substrates. Integ. Ferro. **101**, 4. (Atıf sayısı: 0)

12. Zhang, L. C., Vasiliev, A.L., **Misirlioglu, I. B.**, Alpay, S. P., Aindow, M., and Ramesh, R. (2008) Cation ordering in epitaxial lead zirconate titanate films. Appl. Phys. Lett., **93**, 262903 (Atıf sayısı: 1).

13. Boldyreva, K., Pintilie, L., Lotnyk, A., **Misirlioglu, I. B.**, Alexe, M., Hesse, D. (2008) Ferroelectric/Antiferroelectric Pb(Zr0.8Ti0.2)O3/PbZrO3 Epitaxial Multilayers: Growth and Thickness-Dependent Properties. Ferroelectrics, **370**, 140 (Atıf sayısı: 1).

14. Report: 2008 Fiscal Year Annual Report of Office of Fossil Energy, U. S. Department of Energy: III.A.7 Local Electronic Structure and Surface Chemistry of SOFC Cathodes - III.A SECA Research & Development / Cathode Development.

15. **Misirlioglu, I. B.**, Pintilie, L., Boldyreva, K., Alexe, M. and Hesse, D. (2007) Antiferroelectric hysteresis loops with two exchange constants using the two dimensional Ising model. Appl. Phys. Lett., **91**, 202905 (Atıf sayısı: 1).

16. Boldyreva, K., Pintilie, L., Lotnyk, A., **Misirlioglu, I. B.**, Alexe, M. and Hesse, D. (2007) Thickness driven antiferroelectric-to-ferroelectric phase transition of thin PbZrO3 layers in PbZrO3/PbZr0.8Ti0.2O3 multilayers. Appl. Phys. Lett., **91**, 122915 (Atıf sayısı: 16).

17. **Misirlioglu, I. B.**, Alexe, M., Pintilie, L. and Hesse, D. (2007) Space charge contribution to the apparent enhancement of polarization in ferroelectric bilayers and multilayers. Appl. Phys. Lett., **91**, 022911 (Atıf sayısı: 18).

18. Alpay, S. P., **Misirlioglu, I. B.** & Nagarajan, V. (2007) Comment on Simulation of interface dislocations effect on polarization distribution of ferroelectric thin films. Appl. Phys. Lett., **88**, 092903 (Atıf sayısı: 3).

19. Akcay, G., **Misirlioglu, I. B.** & Alpay, S. P. (2007) Dielectric and pyroelectric properties of Barium Strontium Titanate films on orthorhombic substrates with (110)//(100) epitaxy. J. Appl. Phys., **101**, 104110 (Atıf sayısı: 11).

20. **Misirlioglu, I. B.**, Akcay, G., Zhong, S. and Alpay, S. P. (2007) Interface effects in ferroelectric bilayers and heterostructures. J. Appl. Phys., (101), 036107 (Atıf sayısı: 10).

21. Akcay, G., **Misirlioglu, I. B.**, Alpay, S. P. (2007) Response to comment on Dielectric tunability of ferroelectric thin films on anisotropic substrates. Appl. Phys. Lett. 90, 036101 (Atıf sayısı: 1).

22. **Misirlioglu, I. B.**, Akcay, G. and Alpay, S. P. (2006) Polarization variations due to different dislocation configurations in ferroelectric heterostructures. Integ. Ferro., **83**, 67 (Atıf sayısı: 1).

23. Akcay, G., **Misirlioglu, I. B.**, Alpay, S. P. (2006) Dielectric tunability of ferroelectric thin films on anisotropic substrates. Appl. Phys. Lett., **89**, 042903 (Atıf sayısı: 7).

24. **Misirlioglu, I. B.**, Alpay, S. P., He, F. & Wells, B. O. (2006), Stress induced monoclinic phase in epitaxial BaTiO3 on MgO. J. Appl. Phys., **99**, 104103 (Atıf sayısı: 14).

25. **Misirlioglu, I. B.**, Aindow, M., Alpay, S. P. & Nagarajan, V. (2006) Thermodynamic and electrostatic analysis of threading dislocations in epitaxial ferroelectric films. Appl. Phys. Lett., **88**, 102906 (Atıf sayısı: 16).

26. **Misirlioglu, I. B.**, Vasiliev, A. L., Aindow, M. & Alpay, S. P. (2006) Defect microstructures in epitaxial PbZr0.2Ti0.8O3 films grown on (001) SrTiO3 by pulsed laser deposition. J. Mat. Sci., **41**, 697 (Atıf sayısı: 16).

27. Nagarajan, V., Jia, C. L. , Kohlstedt, H., Waser, R., **Misirlioglu, I. B.**, Alpay, S. P. and Ramesh, R. (2005) Misfit dislocations in nanoscale ferroelectric heterostructures, Appl. Phys. Lett., **86**, 192910 (Atıf sayısı: 74).

28. **Misirlioglu, I. B.**, Vasiliev, A. L., Aindow, M., Alpay, S. P. (2005), Strong degradation of physical properties and formation of a dead layer in ferroelectric films due to interfacial dislocations, Integ. Ferro., **71**, 67 (Atıf sayısı: 4).

29. Alpay, S. P., **Misirlioglu, I. B.**, Nagarajan, V., Ramesh, R., (2004) Can interface dislocations degrade ferroelectric properties?, Appl. Phys. Lett., **85**, 2044 (Atıf sayısı: 83).

30. Alpay, S. P., **Misirlioglu, I. B.**, Sharma, A., Ban, Z.-G. (2004) Structural characteristics of ferroelectric phase transformations in single-domain epitaxial films, J. Appl. Phys., **95**, 8118 (Atıf sayısı: 56).

31. **Misirlioglu, I. B.**, Vasiliev, A. L., Aindow, M., Alpay, S. P., Ramesh, R. (2004) Threading dislocation generation in epitaxial (Ba, Sr)TiO3 films grown on (001) LaAlO3 by pulsed laser deposition, Appl. Phys. Lett., **84**, 1742 (Atıf sayısı: 23).

32. Mantese, J. V. , Schubring, N. W., Micheli, A. L., Thompson, M. P., Naik, R., Auner, G. W., **Misirlioglu, I. B.** and Alpay, S. P. (2002) Stress-induced polarization-graded ferroelectrics, Appl. Phys. Lett., **81**, 1068 (Atıf sayısı: 37).

EK DOSYALAR

1.“Potential barrier engineering via Gd doping of $BiFeO_3$ layers in Nb:$SrTiO_3$-$BiFeO_3$-Pt structures displaying diode-like behavior”, Applied Physic Letters dergisinde değerlendirmede.
2. “Electrocaloric Properties of Epitaxial Strontium Titanate Films”, Applied Physics Dergisi’nde basıma Kabul edildi.
3. “Effects of depolarizing field in perforated film of two-axial ferroelectric”, Physics of the Solid State dergisinde değerlendirmede.
4. “Thickness driven stabilization of saw-tooth–like domains upon phase transitions in ferroelectric thin films with depletion charges”, Journal of Applied Physics Dergisi’nde 22 Mart 2012 tarihinde basıldı.

Potential barrier engineering via Gd doping of $BiFeO_3$ layers in Nb:$SrTiO_3$-$BiFeO_3$-Pt structures displaying diode-like behavior

H. Khassaf [1], G. A. Ibanescu [2], I. Pintilie [2], I. B. Misirlioglu [1], L. Pintilie [2]

[1]*Faculty of Engineering and Natural Sciences, Sabancı University, Orhanlı/Tuzla 34956 Istanbul, Turkey*

[2]*National Institute of Materials Physics, Atomistilor 105bis, Magurele, 077125 Romania*

Abstract

The rectifying properties of Nb:$SrTiO_3$-$Bi_{1-x}Gd_xFeO_3$-Pt structures (x=0, 0.05, 0.1) displaying diode-like behavior were investigated via current-voltage characteristics at different temperatures. The potential barrier was estimated for negative polarity assuming a Schottky-like thermionic emission with injection controlled by the interface and the drift controlled by the bulk. The height of the potential barrier at the Nb:$SrTiO_3$-$Bi_{1-x}Gd_xFeO_3$ interface increases with Gd doping. The results are explained by the partial compensation of the *p*-type conduction due to Bi vacancies with Gd doping in addition to the shift of the Fermi level towards the middle of the bandgap with increasing dopant concentration.

Owing to its multiferroic behavior at room temperature (RT), $BiFeO_3$ (BFO) has attracted a considerable interest for application in microelectronics, especially for non-volatile memories with electric writing and magnetic reading or utilization of multiple memory states resulting from different orientation of polarization and magnetization in the crystal lattice. [1-8] It has also been considered as a candidate to replace lead-based piezoelectric ceramics. [9,10] Despite all these attractive functionalities, one major problem hindering the applications based on BFO thin films is the presence of high leakage currents that screen the applied field in addition to obscuring the current peaks associated with polarization reversal in this system. [11-14] Among the methods to reduce leakage was doping with iso- or heterovalent atoms replacing Bi or Fe in the BFO lattice, such as La, Nb, Ca, Mn, Cr, Gd or alloying with other perovskites. [15-21] Particularly Gd is of interest due to the fact that, owing to its high valence spin state, it may induce some ferromagnetic activity which is more attractive for applications compared to the antiferromagnetic order specific for pure BFO. Reduction in leakage was reported for Gd doped BFO films deposited by metal organic decomposition on platinized Si wafers.[22] On the other hand it was demonstrated that the leakage current in epitaxial BFO layers deposited by pulsed laser deposition (PLD) on single crystal $SrTiO_3$ substrates with $SrRuO_3$ electrodes can be manipulated by via control of the orientation of the BFO layer. [23] BFO deposited directly on Nb doped conducting $SrTiO_3$ single crystal substrates (Nb:$SrTiO_3$, or shortly STON) with Pt top electrode also leads to a structure with diode-like behavior. [24] Despite the very recent interest in such structures, to our knowledge, there are no studies reporting neither on the height of the potential barrier at the STON-BFO interface nor the dopant dependence of the potential barrier and whether this barrier could be engineered by doping the BFO layer.

In the present study we report on control of the barrier height by Gd doping of the BFO layer in a Nb:$SrTiO_3$-$Bi_{(1-x)}Gd_xFeO_3$-Pt (STON-BFGO-Pt) structure with [001] direction of STON perpendicular to the plane (x=0, 0.05, 0.1). The BFGO layer was prepared by sol-gel deposition on (001) STON substrates having 0.7 % Nb doping. X-ray diffraction analysis showed that the layer grows

quasi-epitaxially on the single crystal substrate at a thickness of around 100 nm with the (001) and (002) film peaks appearing right on the left side of (001) and (002) STON peaks respectively with other bulk BFO peaks being absent. The top Pt contacts of 0.1x0.1 mm^2 were deposited by magnetron RF-sputtering through a shadow mask. The electric measurements were performed at different temperatures by inserting the samples in a cryogenic probe station from LakeShore (model CPX-VF). The capacitance of the samples were measured with a Hioki LRC bridge, the leakage current with a Keithely 6517 electrometer and the hysteresis loop with a TF2000 ferroelectric tester from AixAcct.

Polarization-applied field measurements showed that the hysteresis loops both in pure and doped BFO were severely distorted by the leakage current even at temperatures lower than RT. The ferroelectric behavior of the BFO layers could be confirmed only by capacitance-voltage (C-V) characteristics as shown in Figure 1. The C-V characteristic in Figure 1 presents the butterfly shape specific for ferroelectrics. The shift between the sweep-up and sweep-down characteristics is small, suggesting a small coercive field. Moreover, the fact that the switching takes place only in one polarity indicates the presence of a considerable internal electric field, probably due to highly asymmetric charge accumulations at each interface, [25] similar to the one reported recently for $SrRuO_3$-Pb(Zr,Ti)O_3-Ta Schottky like diodes.[26] Following the C-V measurements, we focused on the current-voltage (I-V) characteristics with the aim to obtain information about the dominant conduction mechanism and to evaluate the potential barrier(s) in the STOM-BFGO-Pt structure. The RT I-V characteristics are presented in the Figure 2 for pure and doped BFO (5 and 10%).

The heavy asymmetry in the RT I-V curve in Figure 2 shows that the STON-BFO-Pt structure has a diode like behavior, being forward biased for positive voltages applied on the top Pt contact and reverse biased for negative voltages applied on Pt. Apparently the current magnitude does not vary much with the Gd doping. The rectification ratio is not very large for this case, being around 40 at +/- 1 V. In order to gain further insight, the I-V characteristics at different temperatures were performed on pure and doped BFO layers. The results are given in Figure 3.

From Figure 3, it is clear that, for the negative polarity there is a great temperature dependence of the leakage current, of about 2 orders of magnitude or more at a voltage of -1 V. On the positive polarity side, the temperature dependence is more evident at low voltages, below 0.6 V. At higher voltages the temperature dependence diminishes, and the steps occurring in the I-V characteristics at certain voltages support the hypothesis that the leakage current for forward bias at high voltages is dominated by space charge limited currents (SCLC) possibly with an exponential distribution of traps.[27] In the following paragraphs, only the negative part of the I-V characteristics will be analyzed in detail in order to extract information regarding the dominant conduction mechanism for reverse bias. The rectifying behavior of the STON-BFO-Pt structure suggests that thermionic emission over a potential barrier may be responsible for the leakage current in reverse bias. The question is the following: Is the potential barrier located at the STON-BFO interface or at the BFO-Pt interface? It could be that potential barriers exist at both interfaces but one of them is more permeable to charge injection than the other, thus leading to the diode-like I-V behavior. Another unknown is the conduction type of BFO in bulk of the film. Previous reports suggest *p*-type conduction due to Bi losses during PLD deposition or during crystallization annealing in the case of sol-gel deposited films. [24,28] Work of Guo *et*. al. on a similar pseudocubic perovksite ($LiNbO_3$) shows that $LiNbO_3$ exhibits a p-type conductivity due to Li losses during fabrication. [29] Therefore, assuming that the BFO films in the present study are also *p*-type, the reverse bias occurs when the negative voltage is applied on the top Pt electrode, meaning positive polarity on the bottom single crystal STON substrate. Therefore, it can be concluded that the reverse biased Schottky contact is located at the bottom STON-BFO interface while the top BFO-Pt interface behaves as a quasi-ohmic contact.

With the above proposition in mind, the temperature dependence of the negative part of the I-V characteristics in Figure 3 was analyzed considering a conduction mechanism in which the injection of charge is controlled by the potential barrier existing at the STON-BFO interface while the drift

throughout the ferroelectric film is controlled by the bulk. The Schottky-Simmons equation was used [30]:

$$J = 2q\left(\frac{2\pi m_{eff} kT}{h^2}\right)^{3/2} \mu E \exp\left(-\frac{q}{kT}\left(\Phi_B^0 - \sqrt{\frac{qE_m}{4\pi\varepsilon_0\varepsilon_{op}}}\right)\right) \quad (1)$$

q is the electron charge, h is the Planck's constant, m_{eff} is the effective mass, k is the Boltzmann's constant, μ is the mobility of electrons in the conduction band of BFO, E is the electric field in the bulk of BFO, T is the temperature, Φ_B^0 is the potential barrier at zero bias, E_m is the maximum field at the interface if a Schottky-like contact is present (with a depletion region having a voltage dependent width), ε_0 is the vacuum permittivity and ε_{op} is the dielectric constant at optical frequencies. E_m is given by [31]:

$$E_m = \sqrt{\frac{2qN_{eff}(V + V_{bi})}{\varepsilon_0\varepsilon_{st}}} + \frac{P}{\varepsilon_0\varepsilon_{st}} \quad (2)$$

Here N_{eff} is the effective density of charge in the depleted region of the Schottky type contact, P is the ferroelectric polarization, V_{bi} is the built-in potential (including the contribution of ferroelectric polarization), and ε_{st} is the static dielectric constant. Depending on the term dominating the value of E_m the current density J from Eqn. 1 will be a function of either the square root or ¼th power of applied voltage. If the polarization term is dominant ($\sqrt{2qN_{eff}(V + V_{bi})/\varepsilon_0\varepsilon_{st}} << P/\varepsilon_0\varepsilon_{st}$) then $\log J \propto V^{1/2}$ and the potential barrier at zero volt Φ_B^0 is drastically reduced by the ferroelectric polarization. If the polarization term is negligible in Eqn. 2 then $\log J \propto V^{1/4}$. It must be noted that Eqn. 2 applies if the ferroelectric film is only partially depleted in the voltage range employed for electrical measurements. Referring to the samples studied in this work, it is clear that pure and doped BFO layers are partially depleted in the voltage range used for C-V measurements (See Figure 1) as the capacitance varies continuously with the applied voltage. In the case of a fully depleted film the capacitance should converge towards a constant value with increasing the voltage, which is definitely not the case.

Moreover, considering the difficulty to record a polarization hysteresis and small voltage difference between the maxima of the sweep-up and sweep-down curves in C-V measurements, it can be assumed that remnant polarization is small in the BFO layer and that the *P* term in Eqn. 2 is negligible. Another contribution comes from the possibly large value of ε_{st} in our films which is often reported to be large in sol-gel films due to texturing and N_{eff} is also usually larger than in epitaxial films. Therefore, it is reasonable to consider the case $\log J \sim V^{1/4}$. The data were analyzed in the following way: 1) the $\log(J/T^{3/2})$ was plotted as a function of 1000/T (Arrhenius plot) for a certain applied voltage, and from the slope the potential barrier at the relevant bias voltage was estimated (including the Schottky effect); the potential barriers at several applied voltages were then plotted as a function of $V^{1/4}$ and the potential barrier at zero volt was estimated from the intercept at the origin. Here, the better is the linear fit the more accurate is the estimate of Φ_B^0. However, an error up to 0.1 eV is possible while applying this method. The $V^{1/4}$ dependence of the potential barrier is presented in Figure 4 for the BFO samples with different Gd content.

The intercept at the origin yields the following values for the potential barrier at zero volt: 0.32 eV at zero doping; 0.45 eV for 5 % Gd doping; 0.60 eV for 10 % Gd doping. The results show that the height of the potential barrier increases with increasing the Gd content in the BFO film. This is a very interesting result which can be explained assuming a compensation mechanism of the holes, introduced by the presence of Bi vacancies, by the electrons introduced via Gd doping. In the undoped BFO films the conduction is predominantly *p*-type, the Fermi level is closer to the valance band, thus the potential barrier for holes is not very high. The Gd doping can compensate the *p*-type conduction, thus the Fermi level moves towards the middle of the forbidden band leading to an increase of the potential barrier for holes. However, despite the significant increase of the potential barrier, the magnitude of the leakage current on the negative side of the I-V characteristics does not vary significantly with the Gd doping. Referring to the equation (1) it can be seen that a quantity which may impact significantly the apparent potential barrier and the carrier injection into the ferroelectric layer is the maximum field at the

interface E_m. There are several quantities which can vary with the Gd content, such as N_{eff}, P, V_{bi} and ε_{st}. Therefore, it is hard to decide which of these quantities is contributing the most to the partial compensation of the increased barrier height.

Some useful information can be extracted from the C-V characteristics, assuming that the BFO film behaves as a wide gap semiconductor. The $1/C^2$-V representation can be used to extract information about the density of the free carriers. Figure 5 shows the above representation for the case of pure BFO film. Similar results were obtained for the films doped with 5 % and 10 % Gd. In Figure 5 one has to notice that the intercept at origin on the voltage axis, giving the built in potential V_{bi}, is not the same for sweep up and sweep down. This fact is a finger print for the presence of the ferroelectric polarization, which is changing the band-bending at the interface depending on the sign of the polarization charge.[31] The slope of the $1/C^2$~V dependence was used to estimate the density of the free carriers n, and the intercept was used to extract the built-in potential V_{bi}. The results are presented in the Table 1. It can be seen that the density of the free carriers is slightly decreasing with increasing Gd doping, supporting the hypothesis of the compensation of the p-type conduction by introducing electrons from the doping. However, it has to be underlined that N_{eff} is not the same with n, as N_{eff} accounts for the density of the fixed charge, namely ionized impurities, in the depletion region of the Schottky contact. N_{eff} can be larger than n because of the trapped charges in the depleted region. The difference in n for sweep up and sweep down can give an estimate for 2P, considering that this is the charge compensating the polarization. The obtained value for 2P is between 6 and 11 $\mu C/cm^2$, confirming that the "measurable" polarization is very low because of the screening produced by the high density of free carriers.

In conclusion it was shown that the potential barrier at the STON-BFO interface can be engineered by Gd doping. The height of the potential barrier and the built-in bias increases with Gd doping. While the concentration of the free carriers in the BFO layer decreases, the leakage current remains still too large to record a hysteresis loop. This is because the reduction of the barrier height and

the increase of the built-in potential have opposite effects on the current density according to the equations (1) and (2). Further studies are needed to fully elucidate the origin of the high conductivity in pure BFO films. Only in this way the compensation mechanism by doping can be effective in the reduction of the leakage current.

Acknowledgements

H. K. and I. B. M. acknowledge the funding provided by TUBITAK through grant 109M686. I. B. M. also acknowledges the support provided by the Turkish Academy of Sciences-GEBIP program.

References

1. G. Catalan and J.F. Scott, Adv. Mat. 21, 2463 (2009).
2. J.F. Scott, Nat. Mat. 6, 256 (2007).
3. W. Eerenstein, N.D. Mathur, and J.F. Scott, Nature 442, 759 (2006).
4. R. Ramesh and N.A. Spaldin, Nat. Mat. 6, 21 (2007).
5. J. Wang, J.B. Neaton, H. Zheng, V. Nagarajan, S.B. Ogale, B. Liu, D. Viehland,V. Vaithyanathan, D.G. Schlom, U.V. Waghmare, N.A. Spaldin, K.M. Rabe, M. Wuttig, R. Ramesh, Science 299, 1719 (2003).
6. T. Zhao, A. Scholl, F. Zavaliche, K. Lee, M. Barry, A. Doran, M.P. Cruz, Y.H. Chu,C.Ederer, N.A. Spaldin, R.R. Das, D.M. Kim, S.H. Baek, C.B. Eom, R. Ramesh, Nat. Mat. 5, 823 (2006).
7. X. Qi, J. Dho, M. Blamire, Q. Jia, J.S. Lee, S. Foltyn, J.L. MacManus-Driscoll, J. Mag. Mag. Mat. 283, 415 (2004).
8. Y.H. Chu, L.W. Martin, M.B. Holcomb, and R. Ramesh, Materials Today 10, 16 (2007).
9. R.J. Zeches, M.D. Rossell, J.X. Zhang, A.J Hatt, Q. He, C.-H Yang, A. Kumar, C.H. Wang, A. Melville, C. Adamo, G. Sheng, Y.-H. Chu, J.F. Ihlefeld, R. Erni, C. Ederer, V. Gopalan, L.Q. Chen, D.G. Schlom, N.A. Spaldin, L.W. Martin, R. Ramesh, Science 326, 977 (2009).

10. S. Fujino,M. Murakami, V. Anbusathaiah, S.-H. Lim, V. Nagarajan, C.J. Fennie, M. Wuttig, L. Salamanca-Riba, I. Takeuchi, Appl. Phys. Lett. 92, 202904 (2008).
11. J. Seidel, L.W. Martin, Q. He, Q. Zhan, Y.-H. Chu, A. Rother, M.E. Hawkridge, P. Maksymovych, P. Yu, M. Gajek, N.Balke, S.V. Kalinin, S. Gemming, F. Wang, G. Catalan, J.F. Scott, N.A.Spaldin, J. Orenstein, R.Ramesh, Nat. Mat. 8, 229 (2009).
12. Y.P. Wang, L. Zhou, M.F. Zhang, X.Y. Chen, J.M. Liu, Z.G. Liu, Appl. Phys. Lett. 84, 1731(2004).
13. S.K. Singh and H. Ishiwara, Jap. J. Appl. Phys. 44, L734 (2005).
14. D. Lebeugle, D. Colson, A. Forget, and M. Viret, Appl. Phys. Lett. 91, 022907 (2007).
15. A.Z. Simoes,E.C. Aguiar, A.H.M. Gonzalez, J. Andres, E. Longo, J.A. Varela, J. Appl. Phys. 104, 104115 (2008).
16. Z.X. Cheng, XL Wang, Y. Du, and SX Dou, J. Phys. D: App. Phys. 43, 242001 (2010).
17. Y.H. Lin, Q. Jiang, Y. Wang, C.W. Nan, L. Chen, J. Yu, Appl. Phys. Lett. 90, 172507 (2007).
18. A.Z. Simoes, F. Gonzalez Garcia and C.S. Riccardi, J. Alloys. Com. 493, 158 (2010).
19. Q.H. Jiang, C.W. Nan, and Z.J. Shen, J. Am. Cer. Soc. 89, 2123 (2006).
20. V.R. Palkar, D.C. Kundaliya, S.K. Malik, and S. Bhattacharya, Phys. Rev. B. 69, 212102 (2004).
21. M. A. Khan, T. P. Comyn and A. J. Bell, Appl. Phys. Lett. 92, 072908 (2008).
22. G. D. Hu, X. Cheng, W. B. Wu, and C. H. Yang, Appl. Phys. Lett. 91, 232909 (2007).
23. L. Pintilie, C. Dragoi, Y.H. Chu, L.W. Martin, R. Ramesh, M. Alexe, Appl. Phys. Lett. 94, 232902 (2009).
24. H. Yang, H.M. Luo, H. Wang, I.O.Usov, N.A. Suvorova, M. Jain, D.M. Feldmann, P.C. Dowden, R.F. DePaula, Q.X. Jia, Appl. Phys. Lett. 92, 102113 (2008).
25. I. B. Misirlioglu, M. B. Okatan, and S. P. Alpay, J. Appl. Phys. 108, 034105 (2010).
26. L. Pintilie, V. Stancu, L. Trupina, and I. Pintilie, Phys. Rev. B 82, 085319 (2010).

27. D. S. Shang, L. D. Chen, Q. Wang, W. Q. Zhang, Z. H. Wu, and X. M. Li, Appl. Phys. Lett. 89, 172102 (2006).

28. R. Mazumder and A. Sen, J. Alloys Comp. 475, 577 (2009).

29. S.M. Guo, Y.G. Zhao, C.M. Xiong, and P.L. Lang, Appl. Phys. Lett. 89, 223506 (2006).

30. L. Pintilie, I. Vrejoiu, D. Hesse, G. Le Rhun, and M. Alexe, Phys. Rev. B75, 104103 (2007).

31. L. Pintilie and M. Alexe, J. Appl. Phys. 98, 123103 (2005).

Table and Figure Captions

Table 1. The estimated values for the density of free carriers n and for the built-in potential V_{bi} for different values of the Gd doping. The estimates were performed considering a thickness of about 200 nm for the BFO films and a value of 800 for the static dielectric constant. The last value is based on the fact that the capacitance value at -1 V is about the same for all samples.

Figure 1. C-V characteristic at RT for single phase BFO layer. Measurement performed at 100 kHz with an amplitude of 0.1 V for the a.c. signal.

Figure 2. I-V characteristics at RT for different Gd doping of the BFO layer.

Figure 3. I-V characteristics at different temperatures for BFO films with no Gd doping (a), with 5 % Gd doping (b) and with 10 % Gd doping (c).

Figure 4. The voltage dependence of the potential barrier in the case of BFO films with different Gd doping, on STON substrates. The confidence factor for the linear fit is in all cases higher than 0.99.

Figure 5. The $1/C^2$ vs. voltage representation for the pure BFO film.

Table 1.

Gd doping	0 %		5 %		10 %	
	n (cm^{-3})	V_{bi} (V)	n (cm^{-3})	V_{bi} (V)	n (cm^{-3})	V_{bi} (V)
Sweep up	$1.44x10^{19}$	0.26	$1.43x10^{19}$	0.4	$1.13x10^{19}$	0.46
Sweep down	$1.23x10^{19}$	0.06	$1.08x10^{19}$	0.015	$8.9x10^{18}$	0.026

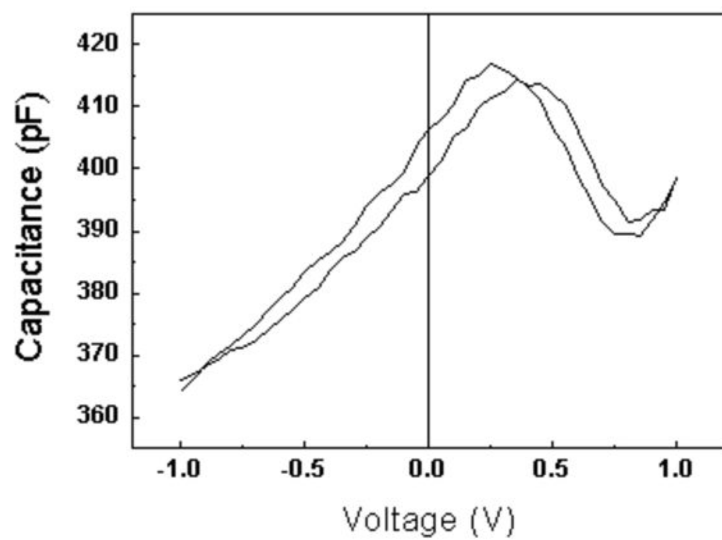

Figure 1.

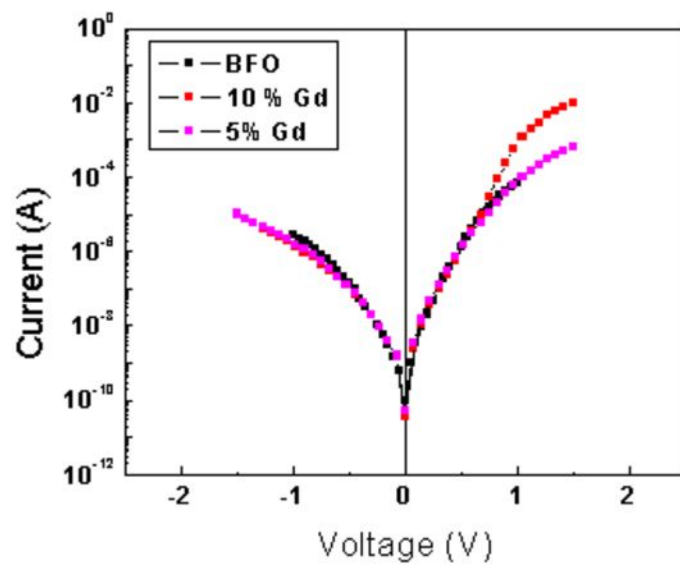

Figure 2.

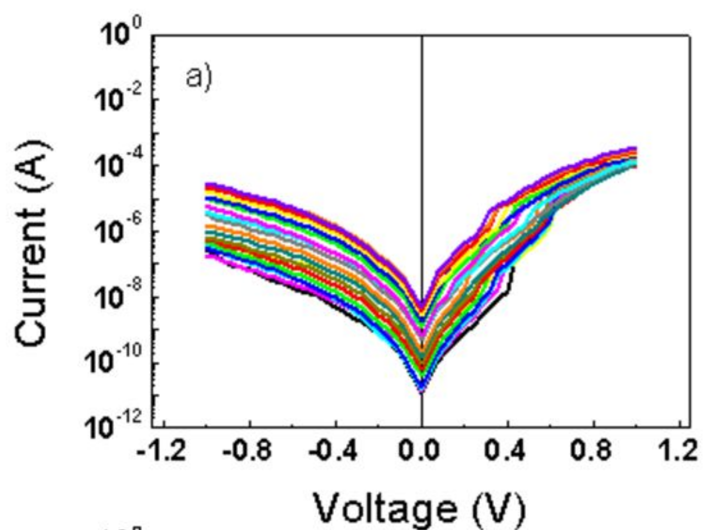

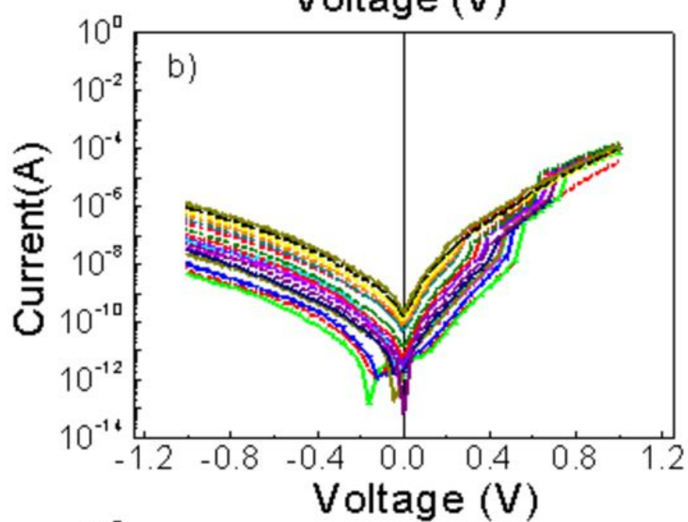

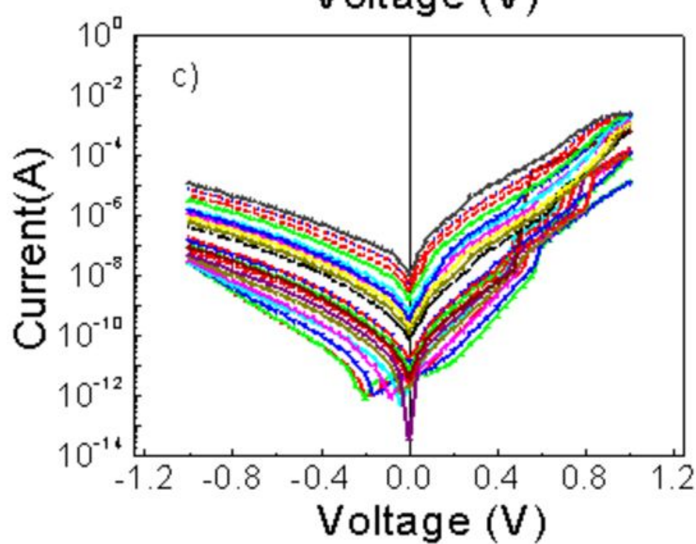

Figure 3.

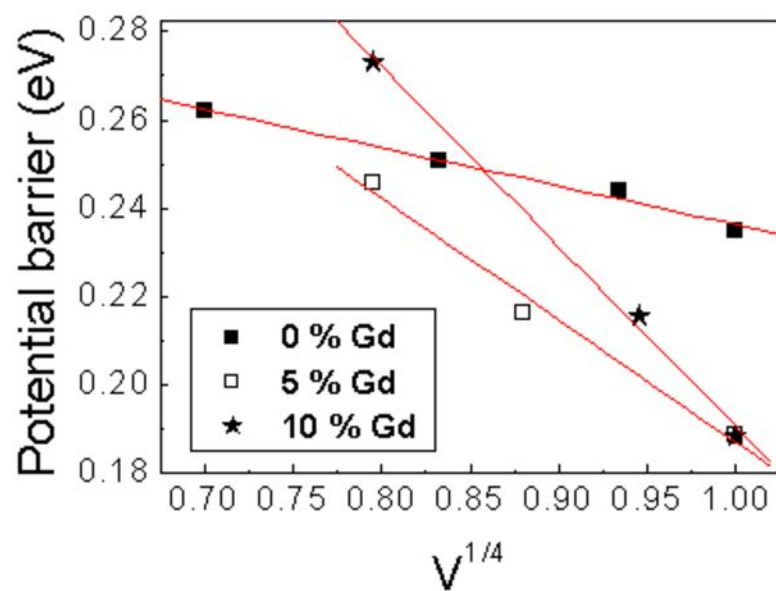

Figure 4.

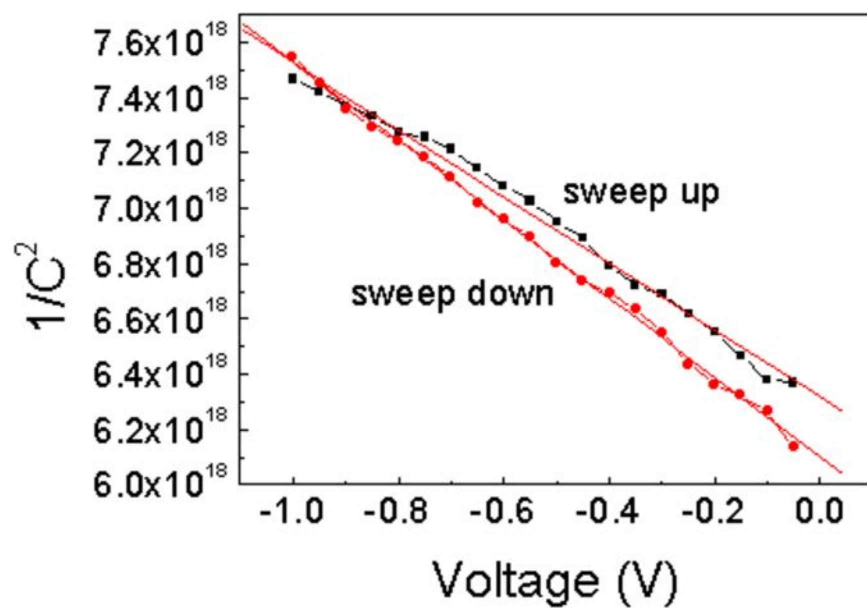

Figure 5.

Electrocaloric Properties of Epitaxial Strontium Titanate Films

J. Zhang, [1] I. B. Misirlioglu, [2] S. P. Alpay, [1,3] and G. A. Rossetti, Jr. [1,a]

[1] *Materials Science and Engineering Program and Institute of Materials Science, University of Connecticut, Storrs, CT 06269, USA*

[2] *Faculty of Engineering and Natural Sciences, Sabancı University, Tuzla-Orhanlı, 34956, Istanbul, Turkey*

[3] *Department of Physics, University of Connecticut, Storrs, CT 06269, USA*

Abstract

The electrocaloric (EC) response of strontium titanate thin films is computed as a function of misfit strain, temperature, electric field strength, and electrode configuration using a nonlinear thermodynamic theory. For films in a capacitor configuration on compressive substrates, the transition between paraelectric and strain-induced ferroelectric tetragonal phases produces a large adiabatic temperature change, ΔT = 5K, at room temperature for electric field changes ΔE =1200 kV/cm. For films on tensile substrates, the transition between the paraelectric and strain-induced ferroelectric orthorhombic phases can also be accessed using inter-digitated electrodes (IDEs). The maximum EC response occurs for IDEs with a [110] orientation.

The pyroelectric and electrocaloric (EC) effects in polar dielectric solids result from the coupling between the electrical and thermal properties. In the EC effect, an adiabatic change in temperature (ΔT) is produced in response to a change in the applied electric field (ΔE).[1-3] Recent research shows that several thin film ferroelectric (FE) systems [including $Pb(Zr,Ti)O_3$ (PZT),[4,5] $PbMg_{1/3}Nb_{2/3}O_3 - PbTiO_3$ (PMN–PT),[6-8] co-polymers,[9] and $SrBi_2Ta_2O_9$[10]] may yield very large adiabatic temperature changes (ΔT >10 K), one to two orders of magnitude greater than in monolithic FEs.[11] Thermodynamic models combining the Maxwell relations and the Landau theory of phase transformations,[12-15] molecular dynamics,[16] phase-field approaches,[17] Monte Carlo simulations,[18] and first-principles calculations [19] have all been used to understand the origins of the EC effect in different types of FE materials and to model their EC properties under different choices of electrical, thermal and mechanical boundary conditions.

One interesting class of materials with EC properties that have so far not been explored is incipient FEs such as $SrTiO_3$ (STO). STO undergoes a ferroelastic phase transition from the prototypical cubic perovskite [$Pm\bar{3}m$] to a tetragonal [$I4/mcm$] structure at 105 K due to the rotations of TiO_6 octahedra about the pseudo-cube axes. Although STO crystals or polycrystalline ceramics remain paraelectric down to 0 K, the FE phase can be induced by uniaxial stress,[20] an external electrical field,[21] or by doping.[22] A thermodynamic analysis by Pertsev *et al.* [23,24] has shown that it is possible to induce a variety of different FE phases in epitaxial thin films of STO that are not stable in monolithic single-crystal or polycrystalline forms. Following this work, ferroelectricity at room temperature (RT ≅ 300 K) in epitaxial (001) STO thin films was observed experimentally by carefully adjusting the equi-biaxial in-plane misfit strain. [25] One of the important features of the Pertsev phase diagram is that it shows that the misfit strain can be used to access two or three different FE phases depending on the

temperature (between ~150 K < T < ~350 K). By adjusting the sign and magnitude of the misfit strain, it was predicted that FE states with out-of-plane or in-plane spontaneous polarizations (along [001] and [100]/[010] of the STO film, respectively) can be generated.[22-23] Because the derivative of the FE polarization with respect to temperature typically shows a sharp maximum near a paraelectric to FE phase transitions, an enhancement in the EC response can be expected. Here we show that the RT adiabatic temperature change ΔT of epitaxial (001) STO films can be controlled by the misfit strain and by varying the thermal and electrical boundary conditions. Depending on the electrode configuration [uniform metal-insulator-metal (MIM) or inter-digitated electrodes (IDE)] and on the field strength, the results demonstrate that a RT ΔT of 1 – 5 K can be achieved in STO films on *both tensile and compressive substrates*.

We consider here a (001) monodomain epitaxial STO film on a thick (001) cubic substrate. Taking into account the equi-biaxial in-plane misfit strain u_m and an applied electrical field E_i, the free energy density of the film by can be expressed as: [23,24]

$$\begin{aligned} G(P_i, q_i, u_m, E_i, T) = G_0 &+ \tilde{a}_1(P_1^2 + P_2^2) + \tilde{a}_3 P_3^2 + \tilde{a}_{11}(P_1^4 + P_2^4) + \tilde{a}_{33} P_3^4 + \tilde{a}_{12} P_1^2 P_2^2 \\ &+ \tilde{a}_{13}(P_1^2 + P_2^2) P_3^2 + \tilde{b}_1(q_1^2 + q_2^2) + \tilde{b}_3 q_3^2 + \tilde{b}_{11}(q_1^4 + q_2^4) \\ &+ \tilde{b}_{33} q_3^4 + \tilde{b}_{12} q_1^2 q_2^2 + \tilde{b}_{13}(q_1^2 + q_2^2) q_3^2 - \tilde{t}_{11}(P_1^2 q_1^2 + P_2^2 q_2^2) \\ &- \tilde{t}_{33} P_3^2 q_3^2 - \tilde{t}_{12}(P_1^2 q_2^2 + P_2^2 q_1^2) - \tilde{t}_{13}(P_1^2 + P_2^2) q_3^2 \\ &- \tilde{t}_{31} P_3^2 (q_1^2 + q_2^2) - t_{44} P_1 P_2 q_1 q_2 - \tilde{t}_{44}(P_1 P_3 q_1 q_3 + P_2 P_3 q_2 q_3) \\ &+ (C_{11} + C_{12} - 2C_{12}^2 / C_{11}) u_m^2 - E_1 P_1 - E_2 P_2 - E_3 P_3 \end{aligned} \quad (1)$$

where G_0 is the free energy density of the paraelectric cubic phase, P_i are the components of the polarization vector, q_i are the structural order parameters describing the rotation of the TiO_6 octahedra, and C_{ij} are the elastic moduli at constant P_i and q_i in Voigt notation. The re-normalized coefficients $\tilde{a}_i$ and $\tilde{a}_{ij}$, $\tilde{b}_i$ and $\tilde{b}_{ij}$, and $\tilde{t}_{ij}$ entering Eq. (1) are given by: [23,24]

$$\tilde{a}_1 = a_1 - \left(g_{11} + g_{12} - 2\frac{C_{12}}{C_{11}} g_{12} \right) u_m, \quad \tilde{a}_3 = a_1 + 2\left(\frac{C_{12}}{C_{11}} g_{11} - g_{12} \right) u_m, \quad (2a)$$

$$\tilde{a}_{11} = a_{11} - \frac{g_{12}^2}{2C_{11}}, \qquad \tilde{a}_{33} = a_{11} - \frac{g_{11}^2}{2C_{11}}, \tag{2b}$$

$$\tilde{a}_{12} = a_{12} - \frac{g_{12}^2}{C_{11}}, \qquad \tilde{a}_{13} = a_{12} - \frac{g_{11}g_{12}}{C_{11}} - \frac{g_{44}^2}{2C_{44}}, \tag{2c}$$

$$\tilde{b}_1 = b_1 - \left(\lambda_{11} + \lambda_{12} - 2\frac{C_{12}}{C_{11}}\lambda_{12}\right)u_m, \qquad \tilde{b}_3 = b_1 + 2\left(\frac{C_{12}}{C_{11}}\lambda_{11} - \lambda_{12}\right)u_m, \tag{2d}$$

$$\tilde{b}_{11} = b_{11} - \frac{\lambda_{12}^2}{2C_{11}}, \qquad \tilde{b}_{33} = b_{11} - \frac{\lambda_{11}^2}{2C_{11}}, \tag{2e}$$

$$\tilde{b}_{12} = b_{12} - \frac{\lambda_{12}^2}{C_{11}}, \qquad \tilde{b}_{13} = b_{12} - \frac{\lambda_{11}\lambda_{12}}{C_{11}} - \frac{\lambda_{44}^2}{2C_{44}}, \tag{2f}$$

$$\tilde{t}_{11} = t_{11} + \frac{g_{12}\lambda_{12}}{C_{11}}, \qquad \tilde{t}_{33} = t_{11} + \frac{g_{11}\lambda_{11}}{C_{11}}, \tag{2g}$$

$$\tilde{t}_{12} = t_{12} + \frac{g_{12}\lambda_{12}}{C_{11}}, \qquad \tilde{t}_{13} = t_{12} + \frac{g_{12}\lambda_{11}}{C_{11}}, \tag{2h}$$

$$\tilde{t}_{31} = t_{12} + \frac{g_{11}\lambda_{12}}{C_{11}}, \qquad \tilde{t}_{44} = t_{44} + \frac{g_{44}\lambda_{44}}{C_{44}}, \tag{2i}$$

where a_i and a_{ij}, b_i and b_{ij}, and t_{ij} are the stress-free, monodomain dielectric stiffness coefficients, structural order parameter susceptibility coefficients, and coupling coefficients between the polarization P_i and the structural order parameter q_i, respectively. In Voigt notation, g_{ij} are the electrostrictive constants and λ_{ij} are the coupling coefficients between the strain and q_i.

Using Eqs. (1) and (2), the equations of state $\partial G / \partial P_i = 0$ and $\partial G / \partial q_i = 0$ at E_i=0, and the values of the property coefficients for STO given in Ref. [23], we obtain the identical misfit $u_m - T$ phase diagram of epitaxial monodomain STO films as given by Pertsev *et al*.. [24] Figure 1 shows the stability regions of various phases for 150 K < T < 400 K and –0.02 < u_m < 0.02. The possible phases and their corresponding order parameters that appear in Fig. 1a and b are: HT:

P_1=P_2=P_3=0, q_1=q_2=q_3=0; ST: P_1=P_2=P_3=0, q_1=q_2=0, q_3≠0; FTI: P_1=P_2=0, P_3≠0, q_1=q_2=q_3=0; FTII: P_1=P_2=0, P_3≠0, q_1=q_2=0, q_3≠0; FOI: $|P_1|$=$|P_2|$ ≠0, P_3=0, q_1=q_2=q_3=0. We limit ourselves to these ranges of T and u_m since lower operating temperatures are not of great interest for EC cooling devices and misfit strains larger than 2% in magnitude (depending on the substrate material and film thickness) would be partially or completely relaxed via the formation of two-dimensional periodic arrays of interfacial dislocations.[26] The effect of misfit dislocations can certainly be incorporated into the model using an "effective" substrate lattice parameter,[27] but this would unnecessarily complicate the physical interpretation of the results and would obscure the effect of u_m.

Figure 1 shows that, depending on u_m and T, three FE phases (FTI, FTII, and FOI) can be stabilized by the lattice mismatch between the film and the substrate. For example, at T=225 K and 0.0127 < u_m < 0.0106, the HT phase is stable. The HT phase is a tetragonally distorted but non-polar variation of the parent cubic ($Pm\overline{3}m$) phase. The tetragonality [i.e., $(c-a)/a$ where c, a are the lattice parameters of the HT phase] is positive (negative) for u_m<0 (u_m>0) and is zero for u_m=0 for which c=a=a_0 where a_0 is the lattice parameter of unconstrained STO. For tensile misfit strains u_m>0.0106, the FE FOI phase (which has an equi-biaxial in-plane spontaneous polarization) stabilizes, while for compressive misfit strains u_m<− 0.0127, the FE FTI phase is stabilized with an out-of-plane spontaneous polarization along the [001] direction. At this temperature, a transition to the FTII phase occurs for compressive misfit strains u_m<− 0.0144. This transformation involves the rotation of the TiO_6 octahedra characterized by the structural order parameter q_i and produces a change in the magnitude of polarization along the [001] direction. Hence, the magnitude of the polarization in any of the three FE phases depends on both u_m and T.

The adiabatic temperature change ΔT for the FE phases can be explicitly calculated from the relation: [14]

$$\Delta T(T,E_i,u_m)=\sum_{i=1}^{3}\left(-\int_{E_a}^{E_b}\frac{T}{C_E^0(T,E_i,u_m)}\left(\frac{\partial P_i^0(T,E_i,u_m)}{\partial T}\right)_{E_i}dE_i\right) \quad (3)$$

where the equilibrium polarization $P_i^0(T,E_i,u_m)$ and the equilibrium structural parameter $q_i^0(T,E_i,u_m)$ are obtained from the equations of state for P_i and q_i. The integration limits E_a and E_b define the magnitude of the field change, $\Delta E = E_a - E_b$. Here, the volumetric specific heat $C_E^0(T,E_i,u_m)$ was estimated by adding the computed zero-field values of the excess specific heat to the lattice contributions taken from experimental data.[28]

A MIM construct having a (001) epitaxial STO film sandwiched between uniform metallic electrodes is considered first. For this configuration, E_i=[0,0,E_3] and it is assumed that the bottom electrode is grown pseudomorphically onto the substrate so that both the sign and magnitude of u_m are entirely controlled by the mismatch between the film and the substrate. As can be appreciated from Figure 1, compressive misfit strains favor the FE phases FTI and FTII while tensile misfit strains favor the FE phase FOI. Because both the HT and ST phases are non-polar, and because the component of polarization P_3= 0 is parallel to the field direction E_3, the region of interest is restricted to compressive misfit strains $u_m < -0.01$. This is illustrated in Figure 2(a), which shows a two-dimensional pseudo-color plot of the adiabatic temperature change ΔT as a function of u_m and T for a particular choice of bias field E_a= 50 kV/cm and field change ΔE=120 kV/cm. As expected for conventional FE materials such as $BaTiO_3$ and $PbTiO_3$,[14] the largest EC response occurs near the paraelectric to FE (HT–FTII) phase transition (T = 350 K) where the $P_3(T)$ curve experiences an inflection point and the derivative $\partial P_3/\partial T$ passes through a

steep minimum. However, at the comparatively low field level of 120 kV/cm, the maximum adiabatic temperature change is modest, ΔT< 1 K. The reason for this can be understood from Figure 2(b) where it is seen that the polarization induced along [001] by a field E_3=120 kV/cm is quite small. It is further apparent that the EC response is not significantly enhanced near the FTI-FTII phase boundary, because at this transition $P_3(T)$ shows only a small change in slope that is accompanied by comparatively small but discontinuous change in $\partial P_3/\partial T$. It is evident from Figure 2 that to obtain a larger ΔT, the field strength and/or bias field must be increased. Figure 3 shows how ΔT varies as a function of field change ΔE at RT. It is seen in this figure that for field changes ΔE=1200 kV/cm, a large ΔT of ~5 K can be achieved in STO films at RT. As a point of reference, at these field levels, the EC response for [001] STO in a MIM configuration is closely comparable to that observed in high-quality relaxor PMN-PT films [7] near the temperature of the Curie maximum (~350 K). From this it can be concluded that, as shown for $BaTiO_3$,[14] a relatively small bias field (~50 kV/cm) is sufficient to destroy the discontinuity in polarization at the HT–FTII transition.

Finally, we show that by using an IDE configuration, it is possible to apply in-plane electric fields [29] and by so doing access the HT-FOI phase transformation that occurs under tensile misfit strains. Two IDE configurations are considered, one for which E_i=[E_1,0,0] (or [0,E_2,0]) oriented along [100] (or [010]) and a second for which $E_i=[E_1/\sqrt{2}, E_1/\sqrt{2}, 0]$ oriented along [110]. Pseudo-color plots of the adiabatic temperature change as functions of misfit strain and temperature are shown in Figures 4 and 5 under the same conditions as the MIM configuration shown in Figure 2 (bias field E_a = 50 kV/cm and field change ΔE= 120 kV/cm). As seen in Figure 4, the largest EC response (ΔT = 0.9 K) for the configuration with E_i=[E_1,0,0] occurs near the HT-FOI phase transformation, due to the strong coupling between the in-plane

electrical field and the in-plane spontaneous polarization P_1 or (P_2) of the FOI phase. For an IDE configuration with $E_i=[E_1/\sqrt{2},E_1/\sqrt{2},0]$, the largest EC response (ΔT = 1.2 K) is about 30% higher than for the configuration with $E_i=[E_1,0,0]$. This can be explained by the fact that for the FOI phase with [100] or [010] IDEs, the electric field only induces polarization along one of the components (P_1 or P_2), while for [110] IDEs, the applied field induces polarization in both components P_1 and P_2 with a magnitude of $|P|=\sqrt{P_1^2+P_2^2}$. Comparing the results presented in Figures 2, 4, and 5 it is seen that, under equivalent electrical boundary conditions, both MIM and IDE configurations have comparable EC responses (ΔT ~ 1 K) at RT if the misfit strain is adjusted such this temperature lies near either the HT-FTI or the HT-FOI phase transformation. The EC response as a function ΔE for the two IDE geometries is compared with that of the MIM configuration in Figure 3. As seen in the figure, all three configurations can produce a large ΔT (~ 5 K) at fields greater than 1000 kV/cm. As expected, the response is slightly larger for the [110] configuration compared with the [100] IDE or MIM.

In summary, we have computed the EC response of STO films as a function of the misfit strain, temperature, applied electric field strength, and electrode configuration. It was shown that for STO films on compressive substrates the EC response can be enhanced in a MIM configuration with uniform electrodes by exploiting the HT-FTI transition. At fields of ~ 1000 kV/cm the computed temperature change ΔT = 5 K is comparable to FE films near the Curie point. Alternatively, for STO films on tensile substrates the EC response can be enhanced by using an IDE configuration that exploits the HT-FOI transition, with the maximum response occurring for a [110] IDE orientation. Compared with MIM configurations, STO films utilizing an IDE configuration may offer possibilities to increase the EC response while minimizing the

dead volume of electrodes. These results show that the strain-induced EC properties of incipient FEs are closely comparable to the measured EC response of conventional or relaxor FEs.

J. Z. would like to thank the Scientific and Technological Research Foundation of Turkey (TÜBITAK) for the Research Fellowship Award for Foreign Citizens that supported her stay at the Sabancı University in Istanbul, Turkey. I. B. M. thanks Turkish Academy of Sciences-GEBİP program for financial support.

Figure Captions

Figure 1: Misfit strain *vs*. temperature phase diagram of epitaxial monodomain (001) $SrTiO_3$ films. The order parameters of the phases appearing in this map are: HT: $P_1=P_2=P_3=0$, $q_1=q_2=q_3=0$; ST: $P_1=P_2=P_3=0$, $q_1=q_2=0$, $q_3\neq0$; FTI: $P_1=P_2=0$, $P_3\neq0$, $q_1=q_2=q_3=0$; FTII: $P_1=P_2=0$, $P_3\neq0$, $q_1=q_2=0$, $q_3\neq0$; FOI: $|P_1|=|P_2|\neq0$, $P_3=0$, $q_1=q_2=q_3=0$.

Figure 2: **(a)** The adiabatic temperature change ΔT of an epitaxial (001) $SrTiO_3$ film in a MIM configuration as a function of u_m and T for E_a=50 kV/cm and ΔE=120kV/cm; **(b)** the out-of plane polarization P_3 as a function of temperature at u_m= −0.02 for E_a=0 kV/cm and E_a=50 kV/cm.

Figure 3: The room-temperature adiabatic temperature change ΔT of epitaxial (001) $SrTiO_3$ films with MIM (u_m= −0.020, open squares) and [100]/[010] and [110] IDE configurations (u_m=0.015, open circles and triangles, respectively) as a function of ΔE for E_a= 50 kV/cm.

Figure 4: The adiabatic temperature change ΔT of an epitaxial (001) $SrTiO_3$ film in a [100] IDE configuration as a function of u_m and T for E_a=50 kV/cm and ΔE=120 kV/cm.

Figure 5: The adiabatic temperature change ΔT of an epitaxial (001) $SrTiO_3$ film in a [110] IDE configuration as a function of u_m and T for E_a=50 kV/cm and ΔE=120 kV/cm.

[a] Corresponding author, electronic mail: rossetti@ims.uconn.edu

References

[1] J. D. Childress, J. Appl. Phys. **33**, 1793 (1962).

[2] E. Fatuzzo, H. Kiess, and R. Nitsche, J. Appl. Phys. **37**, 510 (1966).

[3] P. D. Thacher, J. Appl. Phys. **39**, 1996 (1968).

[4] R. Chukka, J. W. Cheah, Z. Chen, P. Yang, S. Shannigrahi, J. Wang, and L. Chen, Appl. Phys. Lett. **98**, 242902 (2011).

[5] A. S. Mischenko, Q. Zhang, J. F. Scott, R. W. Whatmore, and N. D. Mathur, Science **311**, 1270 (2006).

[6] Z. Feng, D. Shi, R. Zeng, and S. Dou, Thin Solid Films **519**, 5433 (2011).

[7] A. S. Mischenko, Q. Zhang, R. W. Whatmore, J. F. Scott, and N. D. Mathur, Appl. Phys. Lett. **89**, 242912 (2006).

[8] T. M. Correia, J. S. Young, R. W. Whatmore, J. F. Scott, N. D. Mathur, and Q. Zhang, Appl. Phys. Lett. **95**, 182904 (2009).

[9] S. G. Lu, B. Rozic, Q. M. Zhang, Z. Kutnjak, and B. Neese, Appl. Phys. Lett. **98**, 122906 (2011).

[10] H. Chen, T.-L. Ren, X.-M. Wu, Y. Yang, and L.-T. Liu, Appl. Phys. Lett. **94**, 182902 (2009).

[11] D. Q. Xiao, Y. C. Wang, R. L. Zhang, S. Q. Peng, J. G. Zhu, and B. Yang, Mater. Chem. Phys. **57**, 182 (1998).

[12] G. Akcay, S. P. Alpay, J. V. Mantese, and G. A. Rossetti, Jr., Appl. Phys. Lett. **90**, 252909 (2007).

[13] G. Akcay, S. P. Alpay, G. A. Rossetti, Jr., and J. F. Scott, J. Appl. Phys. **103**, 024104 (2008).

[14] J. Zhang, A. A. Heitmann, S. P. Alpay, and G. A. Rossetti, Jr., J. Mater. Sci. **44**, 5263 (2009).

[15] J. Karthik and L. W. Martin, Appl. Phys. Lett. **99**, 032904 (2011).

[16] Q. Peng and R. E. Cohen, Phys. Rev. B **83**, 220103 (2011).

[17] B. Li, J. B. Wang, X. L. Zhong, F. Wang, and Y. C. Zhou, J. Appl. Phys. **107**, 014109 (2010).

[18] S. Lisenkov and I. Ponomareva, Phys. Rev. B **80**, 140102 (2009).

[19] S. Prosandeev, I. Ponomareva, and L. Bellaiche, Phys. Rev. B **78**, 052103 (2008).

[20] H. Uwe and T. Sakudo, Phys. Rev. B **13**, 271 (1976).

[21] J. Hemberger, M. Nicklas, R. Viana, P. Lunkenheimer, A. Loidl, and R. Bohmer, J. Phys.: Condens. Matter **8**, 4673 (1996).

[22] J. G. Bednorz and K. A. Muller, Phys. Rev. Lett. **52**, 2289 (1984).

[23] N. A. Pertsev, A. K. Tagantsev, and N. Setter, Phys. Rev. B **61**, R825 (2000).

[24] N. A. Pertsev, A. K. Tagantsev, and N. Setter, Phys. Rev. B **65**, 219901 (2002).

[25] J. H. Haeni, P. Irvin, W. Chang, R. Uecker, P. Reiche, Y. L. Li, S. Choudhury, W. Tian, M. E. Hawley, B. Craigo, A. K. Tagantsev, X. Q. Pan, S. K. Streiffer, L. Q. Chen, S. W. Kirchoefer, J. Levy, and D. G. Schlom, Nature **430**, 758 (2004).

[26] I. B. Misirlioglu, S. P. Alpay, M. Aindow, and V. Nagarajan, Appl. Phys. Lett. **88**, 102906 (2006).

[27] J. S. Speck, A. Seifert, W. Pompe, and R. Ramesh, J. Appl. Phys. **76**, 466 (1994).

[28] D. Ligny and P. Richet, Phys. Rev. B **53**, 3013 (1996).

[29] W. K. Simon, E. K. Akdogan, A. Safari, and J. A. Bellotti, Appl. Phys. Lett. **87**, 082906 (2005).

(a)
HT
FTI
FTII
ST
T (K)
u_m
(b)
HT
FOI
u_m

(a)

T (K)

u_m

(b)

u_m=-0.02

E_a=0 kV/cm

E_a=50 kV/cm

FTII

FTI

HT

P_3 (C/m^2)

T (K)

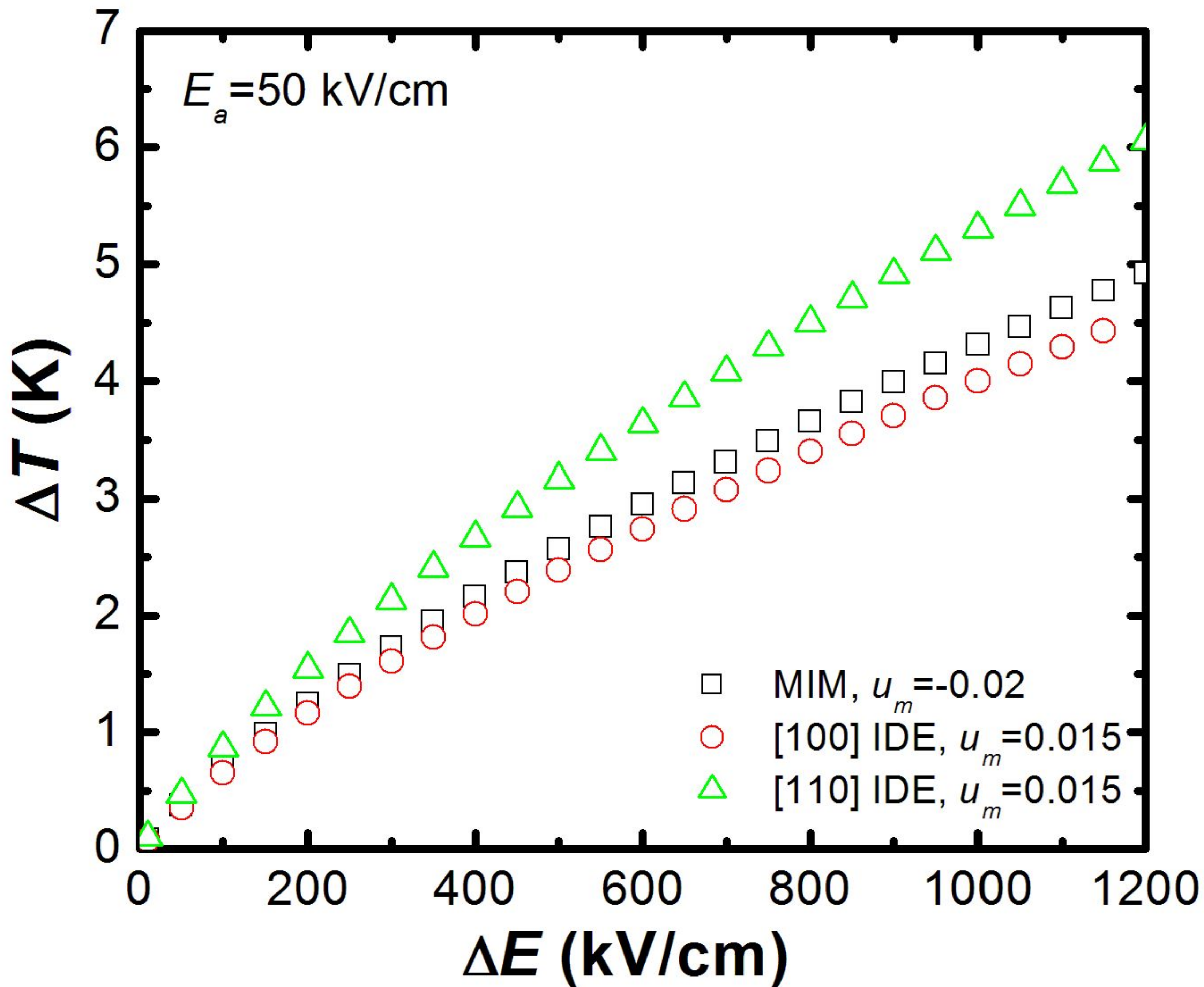

E_a=50 kV/cm
ΔT (K)
ΔE (kV/cm)
MIM, u_m=-0.02
[100] IDE, u_m=0.015
[110] IDE, u_m=0.015
0
1
2
3
4
5
6
7
0
200
400
600
800
1000
1200

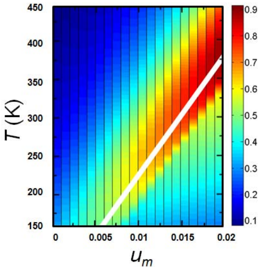

450
400
350
300
250
200
150
T (K)
0
0.005
0.01
0.015
0.02
u_m
0.9
0.8
0.7
0.6
0.5
0.4
0.3
0.2
0.1

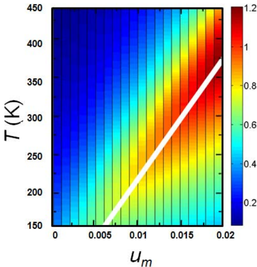

450
400
350
300
250
200
150
T (K)
0
0.005
0.01
0.015
0.02
u_m
1.2
1
0.8
0.6
0.4
0.2

Effects of depolarizing field in perforated film of two-axial ferroelectric

E. Mishina[1], A. Sigov[1], A. P. Levanyuk[1,2,3] and I. B. Misirlioglu[3]

[1] Moscow Institute of Radioengineering, Electronics and Automation, Moscow 117454, Russia.

[2] Departamento de Fisica de la Materia Condensada, C-III, Universidad Autonoma de Madrid, 28049 Madrid. Spain

[3] Faculty of Engineering and Natural Sciences, Sabancı University, Tuzla/Orhanlı 34956 Istanbul, Turkey.

Numerical simulations based on phenomenological theory of ferroelectricity together with the electrostatic equations within the frameworks of Gauss-Seidel iteration method are used to study domain structure in a film of two-axial ferroelectric perforated by air holes. The both polar axes are in the film plane as it is expected in sufficiently thin epitaxial films of $BaTiO_3$ and $(Ba_{1-x}Sr_x)TiO_3$ on MgO. The parameters of $BaTiO_3$ are used in the simulations what is of no importance taking into account the qualitative character of the results: the electrostatic problem is considered as two-dimensional, i.e., it refers formally to infinitely thick and not to very thin layers. The main attention is paid to systems systems containing 16 channels. We study two different orientations of the polar axes with respect to the lattice of channels. It is shown that the character of the domain structure is different for the two orientations. In particular, when the line with the minimum distance between the channels is perpendicular to the bisector of angle between the polar axes this structure contains in the repeating motif one channel and one vortex of the polarization. When one of the polar axes is perpendicular is perpendicular to the line of minimal distance between the channels the situation is less clear. There are indications that the repeating motif in a system of many channels contains two channels and no vortices. There are also indications on a strong influence of the electrodes on the domain structure in this case.

Introduction

Photonic crystals on the base of ferroelectric materials attract now a lot of attention. One of the possibilities of creation of a switchable two-dimensional photonic crystal implies in using of a ferroelectric with the spontaneous polarization laying in the plane of the film as the main optic material. Obtaining of a photonic crystal is achieved, e.g., by the film perforation to get a two-dimensional lattice of holes. Papers 1,2 report about works of this type. Specifically, the authors studied epitaxial films of $(Ba_{0.8}Sr_{0.2})TiO_3$ on MgO perforated by ionic beam to obtain a two-dimensional lattice of holes with 300nm diameter and 450nm period. The properties of thus obtained photonic crystal were promising but not well understood at the same time. This motivates us to begin a theoretical analysis of phenomena which can be expected in such systems. In this paper we study domain structures which can be expected in perforated thin films of two-axial ferroelectrics with the both polar axes laying in the film plane. According to Ref.3 in films of $(Ba_{0.8}Sr_{0.2})TiO_3$ on MgO this situation takes place for thicknesses less than 20nm. We are not aware of experimental data for such films because in Ref. 1,2 films of 70nm thickness have been studied. It is a part of the reasons why do not try to interpret experimental data using the results of the present work.

Emphasize that even if such data were available any direct comparison of them with the presented theoretical results would be imprudent because of complexity of the expected domain structure and its dependence on many factors including those beyond a control at present. The complexity of the domain structure is due to that the discontinuities at the hole surfaces of the polarization lying in the film plane lead to strong depolarizing fields. Being long-range these depolarizing fields influence the polarization in broad regions. Even for inhomogeneous polarization directed strictly parallel to the plane the electric field is three-

dimensional what strongly complicates the calculations and we have to neglect this circumstance. As a result our “two-dimensional” calculations are relevant not to very thin but to very thick layers perforated by very long cylindrical channels. This perforation is the common feature which exists both in thick and in thin films. The perforation effects are much simpler in very thick films and, to the best of our knowledge, they were not studied before what forces us to begin with this case. One can hope that the qualitative character of the results will be the same for thin films though, of course, this is not evident and is worth a separate study.

Note that turning to the case of thin films would premature at present because there are a number of questions which remained unanswered even in the more simple case of thick layers. We mean, e.g., the question about sensitivity of the depolarizing field to conditions of its screening at the surface of the channels. The effectiveness of screening of the depolarizing field by ion absorption at the surfaces of ferroelectric films has been convincingly demonstrated recently (see, e.g., ref.4). Noting is known about presence of such a screening, not to mention its specific features, at the surfaces produced by ion beams. Before studies of this question it would be useful to understand, at least qualitatively, specific features of this influence for very thick layers. One more important question is about the effects of the solid state elasticity which often define the possible orientations of the domain walls. Also of interest is the evolution of the domain structure under application of the external electric field including the polarization switching. All these questions which are important, at the end, for thin films are reasonable to study first for very thick layers.

Even for 2-D case the effects of influence of the depolarizing fields due to several channels prove to be complicated and not treatable analytically. That is why the main method used in this paper is to resolve numerically the system of the constituent equation of the ferroelectric

together with the electrostatic equations. Application of this method to large systems is very costly computationally and overcoming of these difficulties is hardly reasonable at present because of the said above. That is why we study systems with channels whose diameter is much less than in the experiments mentioned above. Turning to systems with larger channel diameter is another possible direction of further investigations.

In the works similar to the presented it is natural to begin with the simplest systems in which the factors defining formation of the domain structures reveal themselves the most clearly. We begin with consideration of square tablets (columns) with one hole (channel) and already for these systems by introducing artificially periodic boundary conditions we try to reveal the domain structures which are expected in large systems. Next we study the domain structures in systems with 16 channels. We are interested in the effects of the depolarizing fields due to the channels and not due to external surface of the prismatic column and that is why we restrict ourselves by two types of electrostatic boundary conditions: a fixed electrical potential at its lateral surface what physically corresponds to metallization of the surface or periodic boundary conditions in order to try to understand the behavior of large systems. Since we take into account the gradients of the polarization in the equations of state we have to define non-electrostatic ("additional") boundary conditions for the polarization. Since we are interested in the electrostatic phenomena we suppose that the surface is neutral with respect to the polarization what corresponds to zero of the normal components of gradients of the polarization components at the surface (infinity of the so-called extrapolation length) and to neglecting of the internal polarity of the surface. In the numerical calculations we use the parameters of ideal epitaxial films of $BaTiO_3$ on MgO.

Preliminary considerations and method

Consider a column of cylindrical form in vacuum. The material is two-axial ferroelectric with the polar axes perpendicular to the axis of the cylinder. A phase transition into a single domain state in this system is impossible because of a huge depolarizing field. For an infinite cylinder polarized perpendicular to the axis this field is:

$$E_{dep} = -\frac{P}{2\varepsilon_0}.$$

Substituting into the equation of state for the ferroelectric

$$AP + BP^3 = E,$$

where it is sufficient, at the moment, to take into account one polarization component only we obtain

$$\left(A + \frac{1}{2\varepsilon_0}\right)P + BP^3 = 0.$$

This equation gives always $P = 0$ because the second term in the parentheses is huge.

As a result it is natural to expect that the polarization distribution arising in such a disk at phase transition will have a form of a vortex. No field arises here what is well known for the analogous case of ferromagnetic. There is vast literature devoted to magnetic vortices and other field-free domain structures ("structures with closed magnetic flux"), see, e.g. ref.5. Here it is important to mention that the magnetic vortices are observed mainly in circular tablets whose height is much smaller than their diameter what is valid also for the polarization vortices, see, e.g., ref.6. This underlines ones more similarity of phenomena in real systems of small size and in "mathematically 2-D" systems are studied in the present work.

A specific feature of magnetic systems is the constancy of the length of the magnetization vector practically at all temperatures below the Curie temperatures. This is far from being so for the polarization in ferroelectric. Because of this some questions which are not very important for ferromagnetics become important for ferroelectrics, in particular, distribution of the polarization in the vortex just after the phase transition which has been found in ref.7. A specific feature of this distribution which is worth mentioning here is zero of the polarization at the vortex center. If the phase transition occurs not in a solid cylinder but in a cylinder with a cylindrical channel at the center the zero of the polarization does not have place but, of course, the value of the polarization is smaller near the internal surface than near the external one. This will be seen which has in the results of our simulations but we shall pay no attention to this because the difference between the two polarizations is the smaller the more are the radius of the hole which quite large experimentally, about 300nm, in the photonic crystals.

If the external surface of the cylinder is metallized the depolarizing field can be exited due to the internal channel only and the simplest way to avoid this is, once more, to create a vortex. If the radius of the internal channel is sufficiently small this does not occur and something similar to a single domain state is formed. However, it is not a state with homogeneous polarization because the latter, anyway, tends to have zero component perpendicular to the channel surface at the surface. As a result the rotation of the polarization vector around the channel axis takes place in one direction, e.g. clockwise, near one of the semicircles of the channel contour and in the opposite direction, anticlockwise, close to the other semicircle. To distinguish from vortex we shall call this distribution “bypassing”. A smooth distribution of the polarization near the transition converts into a domain structure with clearly visible domain walls when we move away from the phase transition since only four directions of

the spontaneous polarization are the most profitable energetically and the energetic loss due to other directions of the polarization increases with lowering of the temperature. It is exactly these domain structures in systems with lattices of the channels which we are interested in in this paper. That is why we are interested in the phenomena in small systems as far they can help us to understand what happens in large systems.

We begin our study with an "elementary brick" of a large system, i.e. a square prism with a central channel. Ratio of the channel radius to square side is the same as for the photonic crystals mentioned before though the sizes are much smaller because of computational limitations and our intention to consider the simplest systems at this stage. We shall see that the character of the polarization distribution in the simplest system at different temperatures and for different boundary conditions sheds some light on what will be observed in systems with 16 channels. It seems that such systems are sufficiently large to illustrate to a certain extent the properties of lattices of experimental interest.

Two-axial ferroelectric which we are considering are described by the constitutive equations

$AP_x + B_1P_x^3 + B_2P_xP_y^2 - G\left[\frac{\partial^2 P_x}{\partial x^2} + \frac{\partial^2 P_x}{\partial y^2}\right] = E_x$ and the second equation with the interchange of x and y. For the values of the coefficients we assume those of Ba TiO_3 on MgO (Ref. 7):

$A = A_1(T - T_c) = 7 \times 10^5\ C^{-2}m^2N \times (T - T_c)$

$B_1 = 20 \times 10^8 \frac{m^5}{FC^2}, \qquad B_2 = -1 \times 10^8 \frac{m^5}{FC^2}, G = 6 \times \frac{10^{-10}m^3}{F}$ but, of course, we use the coefficients for the sake of illustration and nothing more. That is why no higher order terms are taken into account in the equations. Together with the constitutive equations we use electrostatic equations: ***divD*** = 0 and $rot\vec{E} = 0$.

To perform the numerical calculations we discretize the differential equations using a grid with the unit cell $0.5nm \times 0.5nm$. Since the constitutive equations are nonlinear we use point-by-point Gauss-Seidel iterative procedure starting with "guessed" or "initial" values of P_x, P_y and the electric potential φ at all nodes of the grid. Then successively considering in an elementary operation one site or two sites near the boundary we find corrections to the initial values. Typical number of the iterations was 10000 and the difference of the polarization values at final successive iteration was typically of order of 10^{-8} times the polarization itself. We indicate the cases where the number of the iterations was different. The boundary conditions for the differential equations have been already mentioned. We perform the numerical simulations for two cases: "close to the transition", i.e. $(T_c - T) = 10°C$, and "far from the transition", i.e., $(T - T_c) = 150°C$. As an initial state close to the transition we assumed homogeneously polarized state. The found distribution was then used as initial configuration for the simulations far from the transition. We tried to reveal the domain structures for short-circuited electrodes with different orientations with respect to the polar axes. The analysis of behavior of the domain structure under external field has remained beyond the scope of this research.

Square prism with one channel

Recall that we consider two types of the boundary conditions: metallized lateral surface of the prism, i.e. zero potential at all the surfaces and the periodic boundary conditions for all the quantities what has no direct physical meaning for an isolated prism. As it was already mentioned the surfaces with zero potential are assumed to be neutral with respect to polarization, i.e. the normal derivatives of the both components of polarization are zero at the surface. Assuming periodic boundary conditions we try to guess polarization distribution

in such a square forming part of a lattice and surrounded by other identical squares. We shall analyze two variants of orientation of the polar axes with respect to the square sides.

Consider first the case of the polar axes parallel/perpendicular to the square diagonals. The distribution of polarization near the transition in the case of metallized lateral surface is shown at Fig.1a. A distribution of the bypassing type arises here with the dominating direction coinciding with one of the directions of the spontaneous polarization. Far from the transition the general character of the distribution becomes non-trivial with 8 domain walls originating from the hole. Even a more complicated situation appears for periodic boundary conditions. Near the phase transition the distribution is similar to the previous case (Fig.2a) which is quite natural since the crystalline anisotropy, which is presented by the nonlinear terms in the equations of state, has little influence on the polarization distribution close to the transition point. However, it becomes important far from the transition and as a result there appears a distribution presented in Fig.2b. Pay attention to a polarization vortex in the upper left corner of the figure. It is easy to see that it is possible to obtain another variant of the same structure by reflection in the plane perpendicular to the figure plane and containing the diagonal of the square containing lower left and upper right vertices of the square. Instead of situating up and to the left of the hole the vortex will be situated below and to the right and the mean polarization remains the same. We shall below that in a large system (with 16 channels in our case) the both structures can be realized. Another specific feature of the discussed case is that for smaller number of iterations (1000) another structure arises which is also regular but without a vortex and which is also realized in a system with 16 channels. This structure is shown in Fig.2c. It is tempting to interpret this structure as long living no equilibrium one though such a conclusion does not have sufficient base within our approach.

Now we shall consider the case where the polar axes parallel/perpendicular to the square sides. The distribution of polarization near the transition in the square for metallized lateral surface of the prism is shown in Fig.3a. It is seen that the distribution of polarization near the hole is of the bypassing type. The same type of the polarization distribution takes place also far from the transition with a smaller part of regions with non-profitable polarization (Fig.3b). For periodic boundary conditions the polarization distribution close (far) to the transition point is shown in Fig. 4a(b). Here, as well in the case of other orientation, one can obtain another, equivalent variant of structure by reflection in a plane perpendicular to the plane and containing the square diagonal. We shall see similar distributions in the system with 16 channels but this will be not all the story, the domain structure for this orientation of the polar axes seems to be fairly complicated and the chosen system of 16 channels proves insufficient to reveal it unlike to what is possible to do for other orientation of polar axes.

Square prism with 16 channels

We approach now to systems studied experimentally, i.e., to films with regular lattice of holes. Specifically, we studied system of 4x4 channels in a square infinite prism. We fix two types of the boundary conditions at the prism surface, i.e. at the boundaries of the square. To model systems with short-circuited electrodes we fix zero potential and neutrality with respect to polarization at the horizontal sides of the square and periodic boundary conditions at its vertical sides. We shall refer to these conditions as to the mixed ones. Also, we use periodic conditions both for vertical and horizontal sides to try to understand the character of the polarization distribution when the studied system forms part of a much larger system.

Consider first the case of the polar axes parallel/perpendicular to the square diagonals. For the periodic boundary conditions the polarization distribution near the phase transition point

is also periodic (Fig.5). Far from the transition the structure is also periodic with the repeating motif containing one hole (Fig.6). The polarization distribution in the repeating square is the same as in Fig.2b. For smaller iteration number (1000) we obtain another periodic structure with the polarization distribution within every square shown in Fig.2c. For mixed boundary conditions the polarization distribution close to the transition is almost the same as in the previous case (not shown). In our numerical experiment this modification proved to be somewhat different for upper and lower electrodes. It seems that this modification has led to different (than for the case of periodic boundary conditions) domain structure far from the transition (Fig.7). It is natural to interpret this structure as containing two "domains of the domain structure" with the boundary between the "domains" coinciding with second upper row of the holes. The structure of one of the "domains" (the upper row) corresponds to repeating of the distribution shown in Fig. 2b while that of the other domain corresponds to repeating of the second variant of this distribution with the vortex in the right lower part of the repeating square as we discussed in the previous Section.

In the case of the polar axes parallel/perpendicular to the square sides the simplest situation is observed for the mixed boundary conditions. That is why we discuss this case first. Close to the transition the polarization distribution is quite close to that shown in Fig.5 for the other orientation of the polar axes. This is quite natural; see our comments in the previous Section. Far from the transition we obtain almost periodic structure with violation of the periodicity close to the lower electrode (Fig.8 a,b). The polarization distribution "in the bulk" is shown in Fig.8c. It is seen that the distribution does not contain vortices. The same is valid for the vicinity of holes neighboring to electrodes.

For periodic boundary conditions the situation proves qualitatively different from the recently described. Even after 30000 iterations we failed to obtain a regular distribution with

clearly visible periodicity. The distribution of polarization near the holes neighboring to the upper boundary of the system contains vortices (Fig.9). Pay attention to the polarization distribution near four internal holes (Fig.10). It suggests that the large system tends to order with a periodicity $\sqrt{2}$ larger than the minimum distance between the channels. This hypothetical structure does not contain vortices, supposedly they are present at Fig.9 because of unfortunate way of “cutting out” of the part with 16 channels from the large system. For another way of the cutting out, i.e. for another orientation of the cutting line with respect to the line with the minimal distance between the holes, our numerical experiment could be more successful. However, we were unable to continue our simulations. It seems significant that there is a big difference in the results for the mixed and purely periodical boundary conditions. This indicates to a region of influence of the short-circuited electrodes on the domain structure which is considerably larger than for the case of the other orientation of the polar axes which has been considered in the present work.

Concluding remarks

We consider as the most remarkable result of the present work is essential difference in the domain structures for two studied orientations of the polar axes with respect to the lattice of channels. Also, some results indicate to influence of orientation of electrodes with respect to the lattice of channels, however, this question is not studied, in fact. One can expect large difference in switching and other characteristics for different orientations of polar axes and the electrodes with respect to the lattice but these expectations should be confirmed by further studies. Theoretical problem of the domain structure in two-axial ferroelectrics with channels perpendicular to the polar plane proves to be fairly complicated and multi-aspect and the way to its solution seems to be fairly long. From the other side no possibility is seen

to avoid thins long journey if we want to understand the properties of switchable phonon crystals on the base of two-axial ferroelectrics. The present work is no more than the first step along this way. Of course, experimental investigations, in particular, study of influence of orientation of electrodes and of polar axes with respect to the polar axes on properties of phonon crystals is of considerable interest. However, at present it would be difficult to interpret univocally the results of such investigations. For example, the absence of the orientation dependence in the experiment mean both inapplicability of the results of this work to large systems with large number of channels in thin films and the effectiveness of compensation of the depolarizing field due to absorption of ions from air or other processes at the surfaces of channels.

References

1. E. Mishina, A.Zaitsev, N.Ilyin, N.Sherstyuk, A.Sigov, Yu.Golovko, V.Muhortov, A.Kolesnikov, Yu.Lozovik, M.Yemtsova, Th. Rasing, Appl. Phys. Lett. 91, 041107 (2007).

2. Е.Д. Мишина, Н.Э. Шерстюк, А.А.Зайцев, В.М.Мухортов, А.С.Сигов, Известия РАН, Серия Физика Т.71, N 10, 1424 (2007).

3. В.М.Мухортов, Ю.И.Головко, В.В.Колесников и С.В.Бирюков, Письма в ЖТФ т.31, в.23, стр.75 (2005).

4. . D.D.Fong, A.M.Kolpak, J.A.Eastman, S.K. Streifer, P.H.Fuoss, G.B.Stephenson, Carol Thomson, D.M.Kim, K.J.Choi, C.B.Eom, I.Grinberg, and A.M.Rappe, Phys. Rev.Lett. т.96, стр. 127601 (2006).

5. A.Hubert and R.Schafer, Magnetic domains: the analysis of magnetic microstructures, Springer, Berlin, 2009.

6. I.Naumov, L.Bellaiche, and H.Fu, Nature (London) 432, 737 (2004).

7. A.P.Levanyuk, R.Blinc, and R.Pirc, unpublished

8. N.A.Pertsev, A.G.Zembilgotov, and A.K.Tagantsev, Phys.Rev.Lett. 80, 1988 (1998).

9.A.M.Bratkovsky and A.P.Levanyuk, J. Comput. Theor. Nanosci., т.6, стр.465 (2009).

Figure captions

Figure 1. Vectorial map of polarization in infinite square prism with a central channel and metallized surface (a) near the phase transition (b) far from the transition. The polar axes are parallel/perpendicular to the square diagonals. Here and at other figures the origins of the vectors are at a small part of the sites of lattice which discretizes the numerical problem. The maximum magnitude of the plotted vectors is 0.01 C/m^2 for near the transition and 0.17 C/m^2 for far from the transition.

Figure 2. Vectorial map of polarization in infinite square prism with a central channel for periodic boundary conditions at the prism latteral surface (a) near the phase transition (b) far from the transition (c) the same but for a less number of iterations (see text). The polar axes are parallel/perpendicular to the square diagonals. The maximum magnitude of the plotted vectors is 0.01 C/m^2 for near the transition and 0.17 C/m^2 for far from the transition.

Figure 3. Vectorial map of polarization in infinite square prism with a central channel and metallized surface (a) near the phase transition (b) far from the transition. The polar axes are parallel/perpendicular to the square sides. The maximum magnitude of the plotted vectors is 0.01 C/m^2 for near the transition and 0.17 C/m^2 for far from the transition.

Figure 4. Vectorial map of polarization in infinite square prism with a central channel for periodic boundary conditions at the prism latteral surface (a) near the phase transition (b) far from the transition. The polar axes are parallel/perpendicular to the square diagonals. The maximum magnitude of the plotted vectors is 0.01 C/m^2 for near the transition and 0.17 C/m^2 for far from the transition.

Figure 5. Map of polarization in infinite square prism with 16 channels near the phase transition. The boundary conditions are periodic. The polar axes are parallel/perpendicular to the square diagonals; (a) map of the component of polarization along the vertical axis of the figure (b) map of the component of polarization along the horizontal axis of the figure. The unit of the colorbar is C/m^2.

Figure 6. Map of polarization in infinite square prism with 16 channels far from the phase transition. The boundary conditions are periodic. The polar axes are parallel/perpendicular to the square diagonals; (a) map of the component of polarization along the vertical axis of the figure (b) map of the component of polarization along the horizontal axis of the figure. The unit of the colorbar is C/m^2..

Figure 7. Map of polarization in infinite square prism with 16 channels far from the phase transition. The boundary conditions are mixed, the horizontal square sides are at zero potential. The polar axes are parallel/perpendicular to the square diagonals; (a) map of the component of polarization along the vertical axis of the figure (b) map of the component of polarization along the horizontal axis of the figure. The unit of the colorbar is C/m^2..

Figure 8. Map of polarization in infinite square prism with 16 channels far from the phase transition. The boundary conditions are mixed, the horizontal square sides are at zero potential. The polar axes are parallel/perpendicular to the square sides; (a) map of the component of polarization along the vertical axis of the figure (b) map of the component of polarization along the horizontal axis of the figure (c) vectorial map of polarization near of one of the internal channel. The unit of the colorbar is C/m^2..

Figure 9. Vectorial map of polarization near the channels neighboring the upper side of the square. The boundary conditions are periodic, the iteration number is 30000. The polar axes

are parallel/perpendicular to the square sides. The maximum magnitude of the plotted 0.17 C/m^2.

Figure 10. Vectorial map of polarization near the internal channels. The boundary conditions are periodic, the iteration number is 30000. The polar axes are parallel/perpendicular to the square sides. The maximum magnitude of the plotted 0.17 C/m^2.

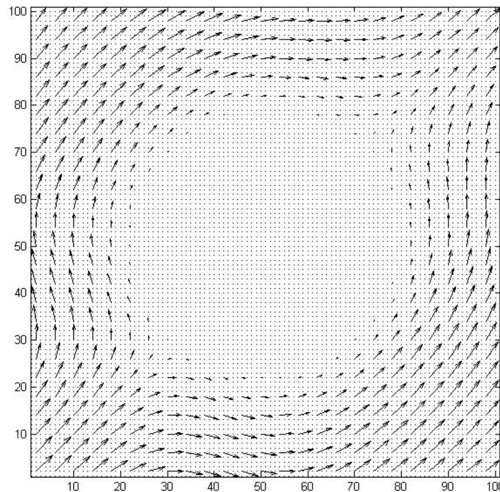

(a)

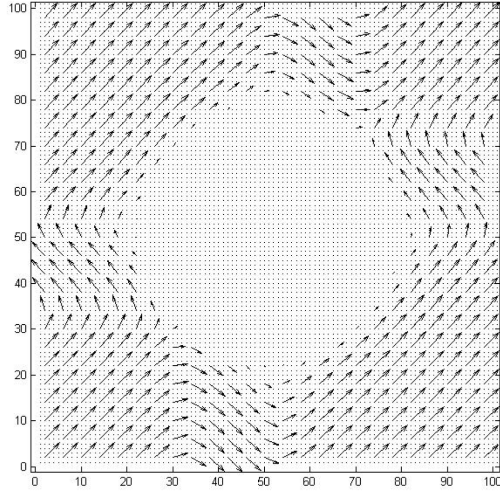

(b)

Figure 1

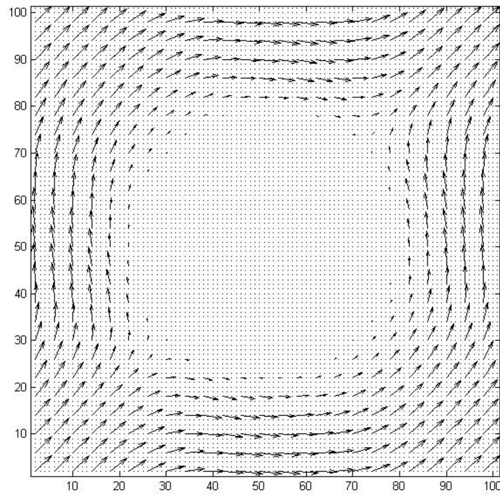

(a)

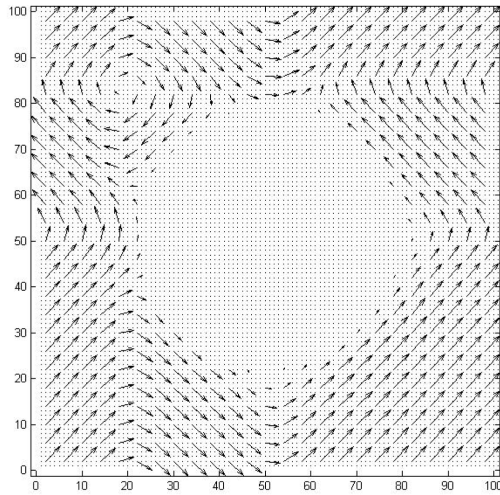

(b)

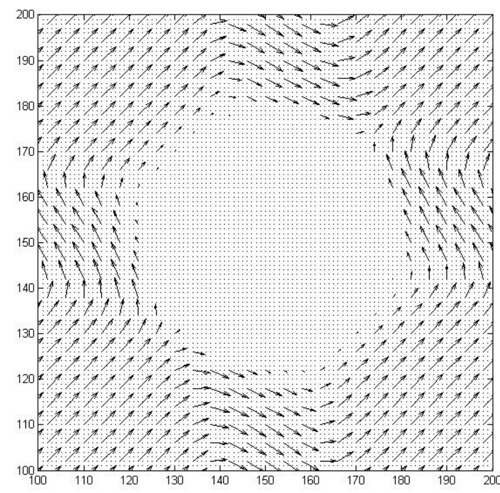

(c)

Figure 2

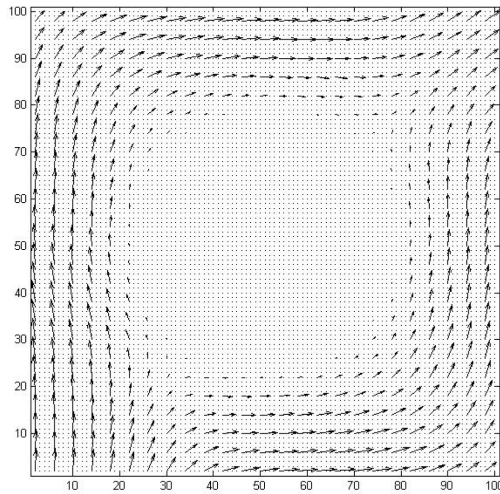

(a)

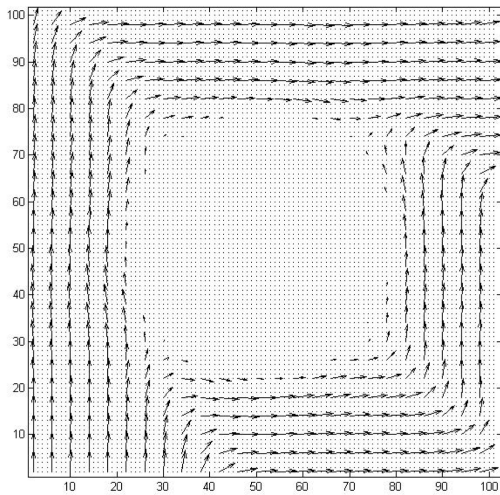

(b)

Figure 3

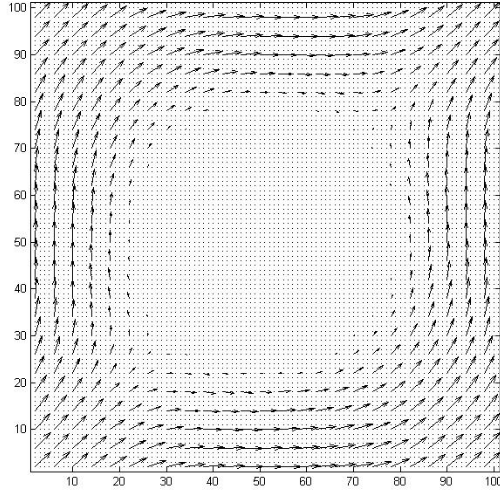

(a)

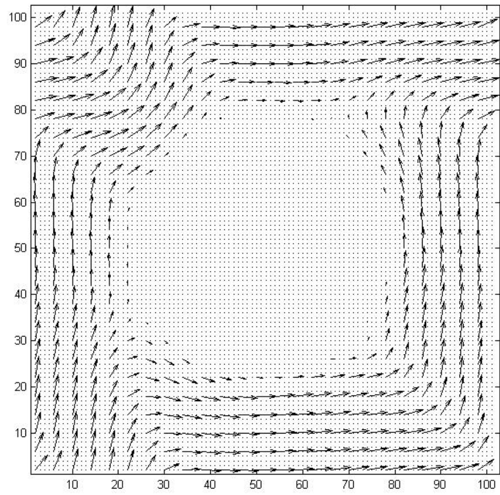

(b)

Figure 4

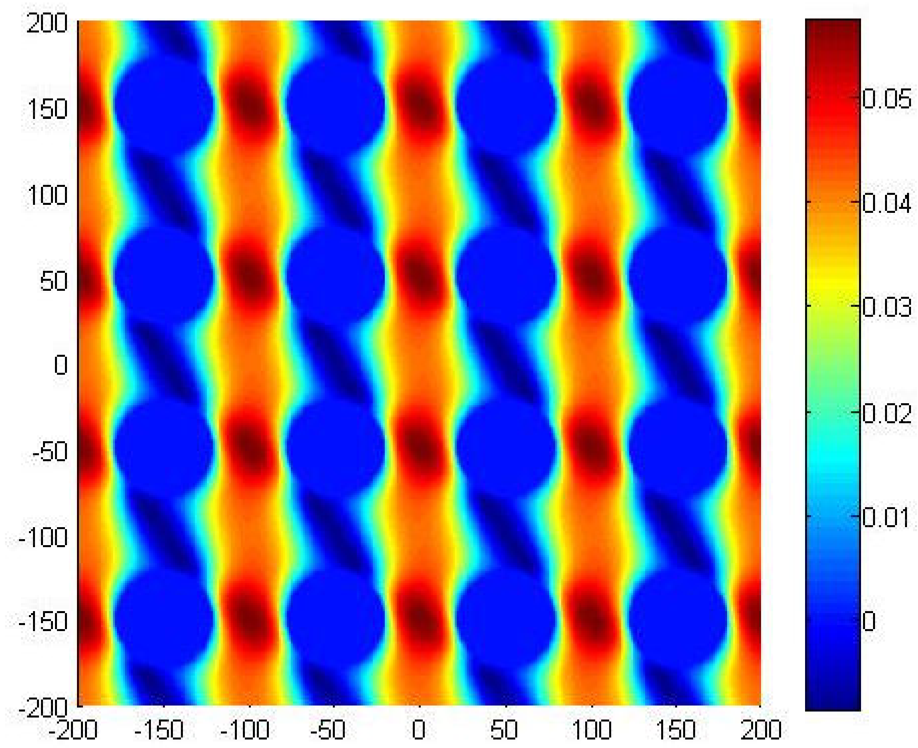

(a)

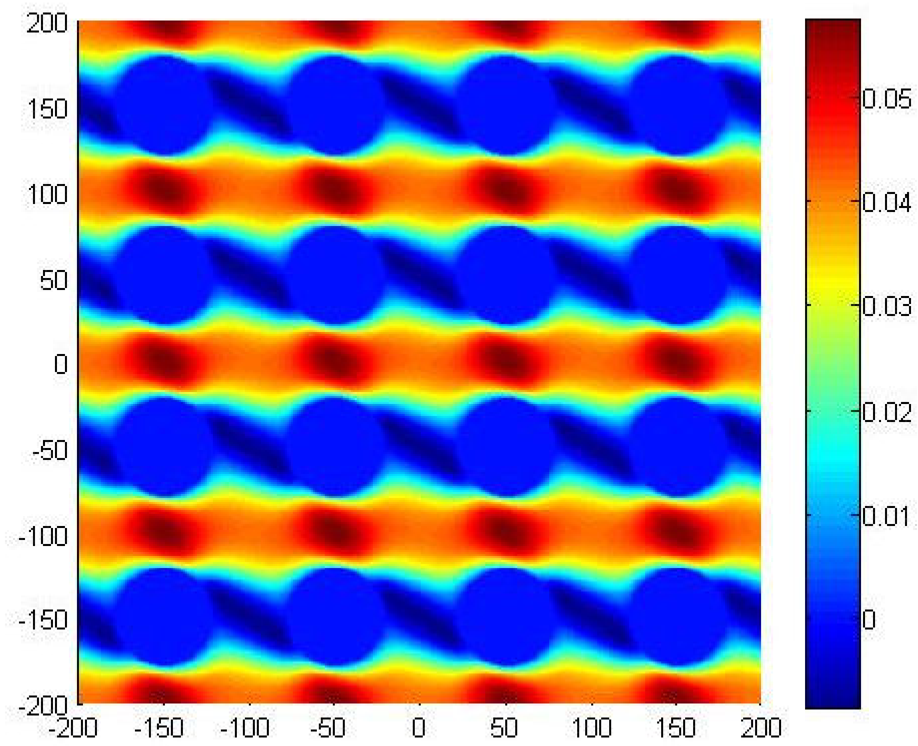

(b)

Figure 5

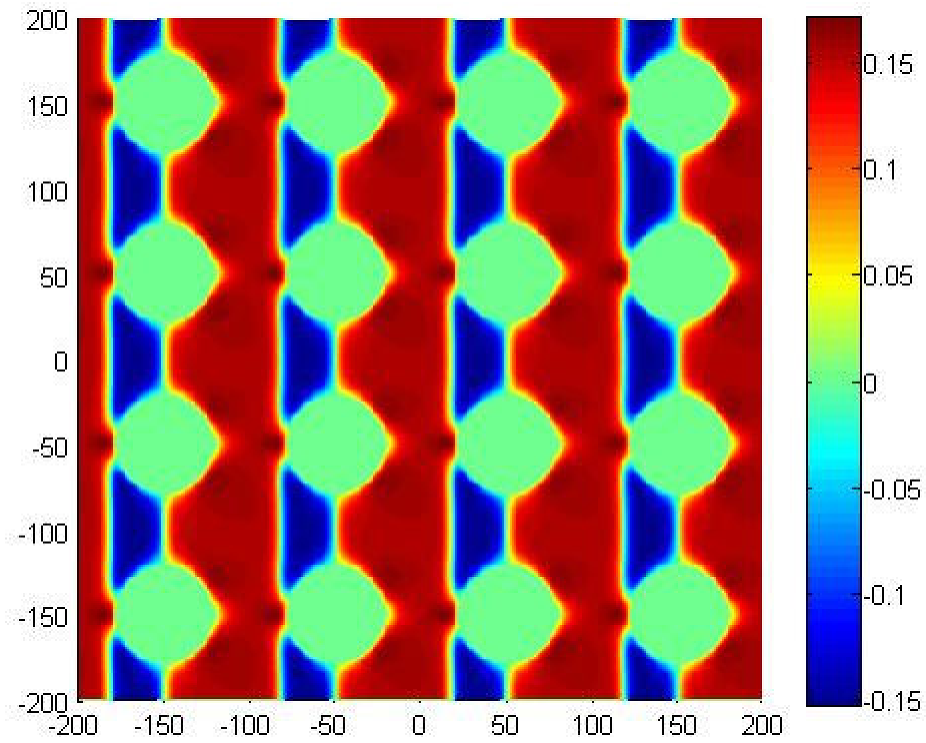

(a)

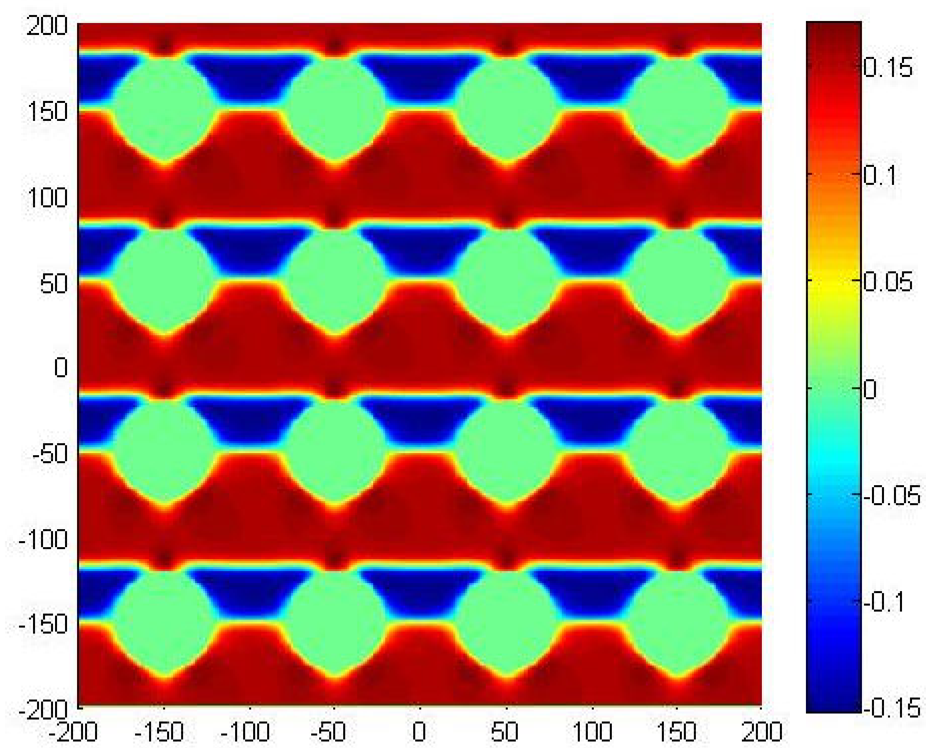

(b)

Figure 6

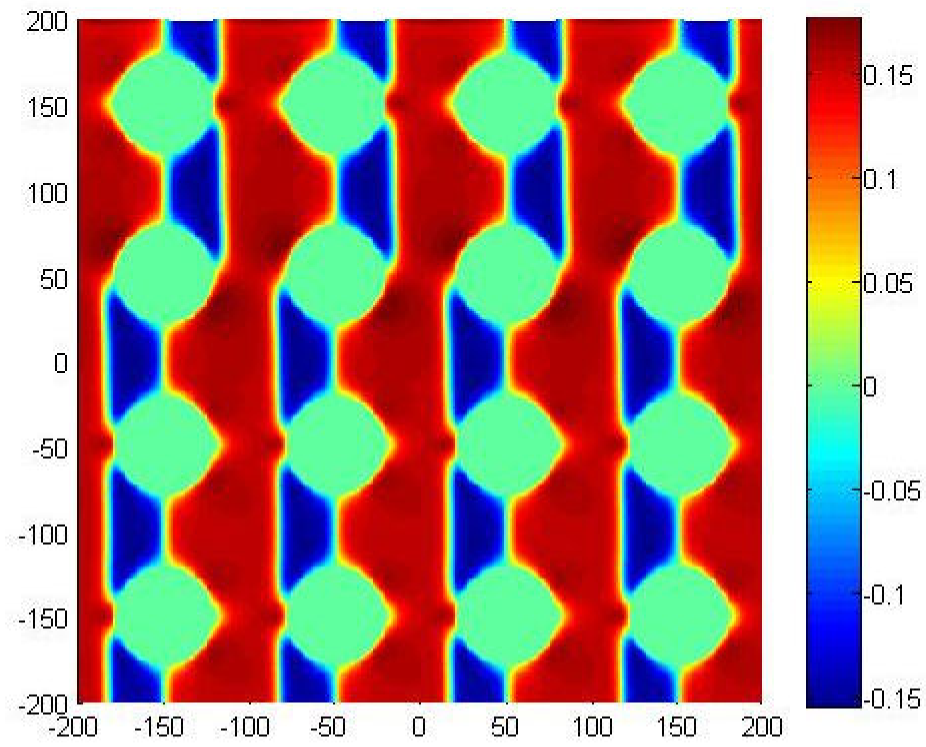

(a)

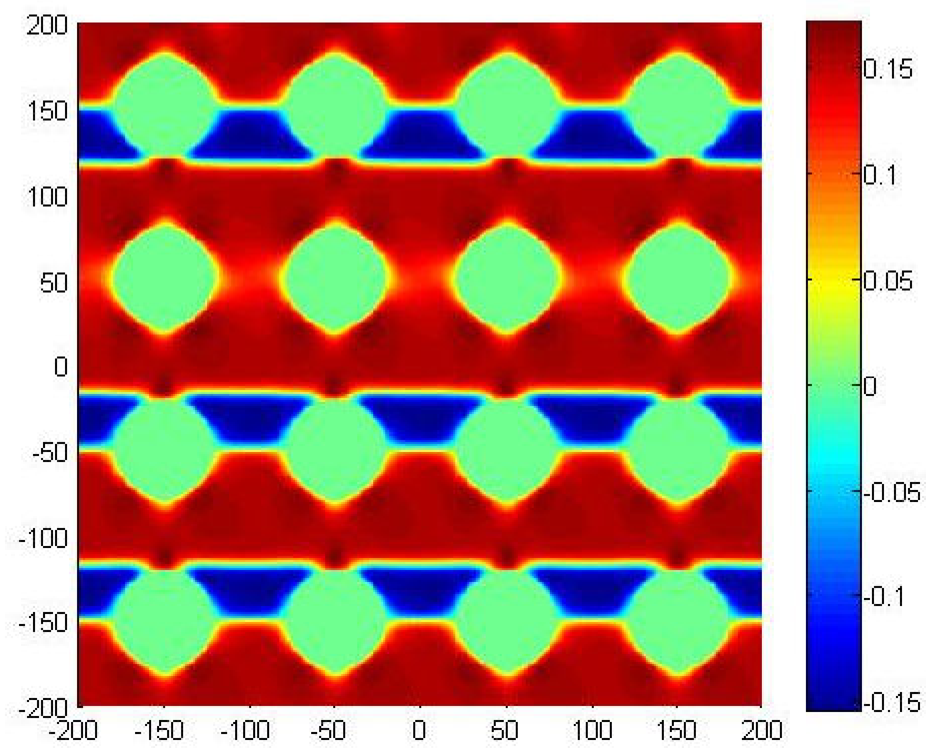

(b)

Figure 7

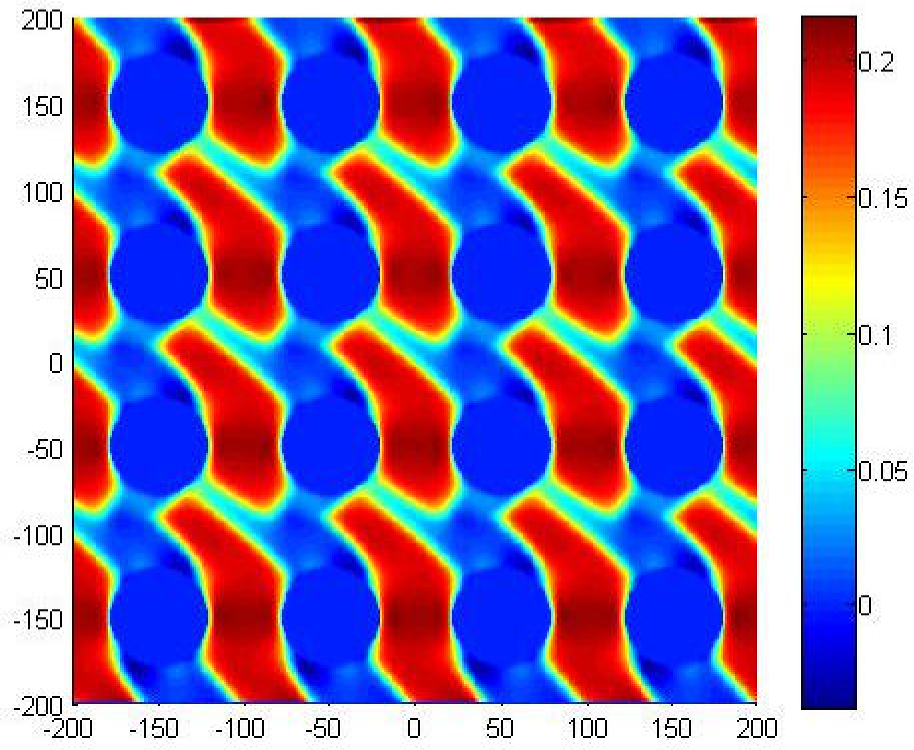

(a)

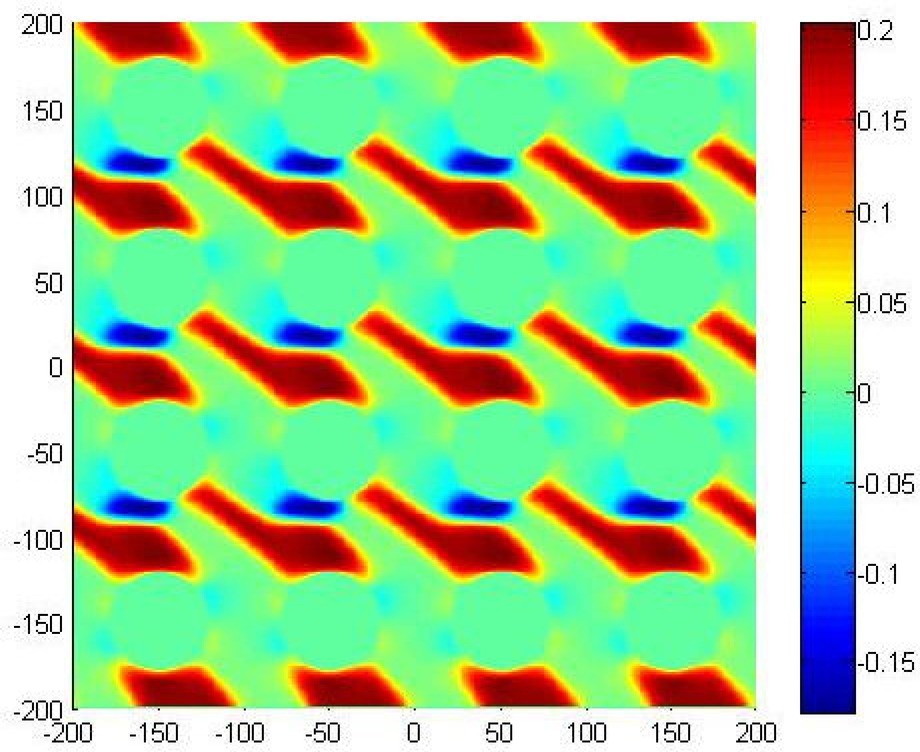

(b)

Figure 8

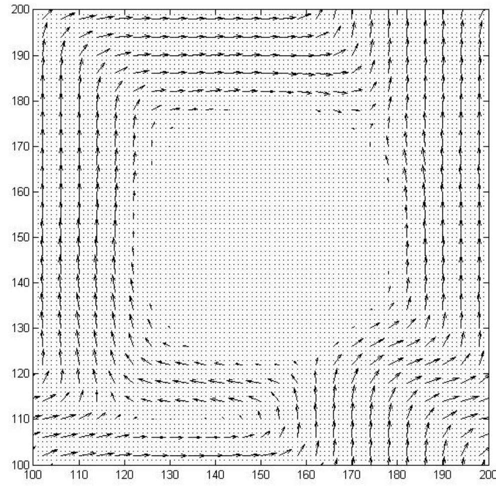

(a)

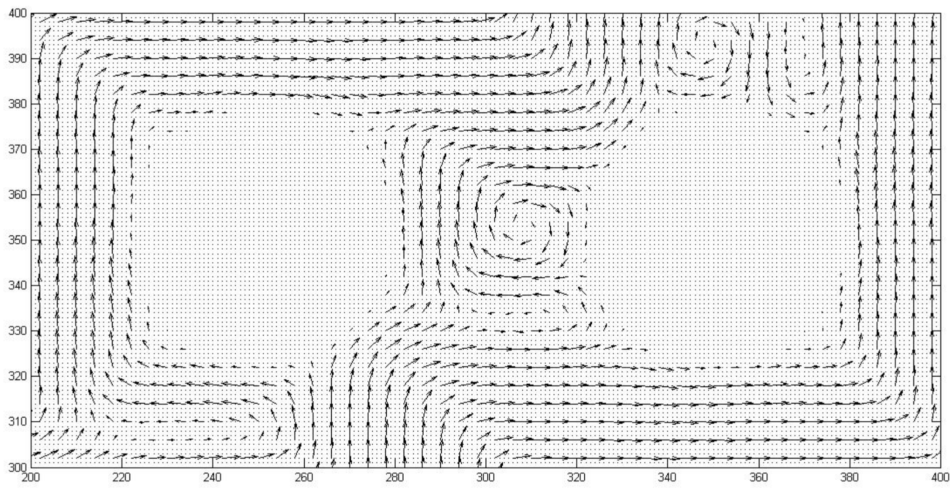

(b)

Figure 9

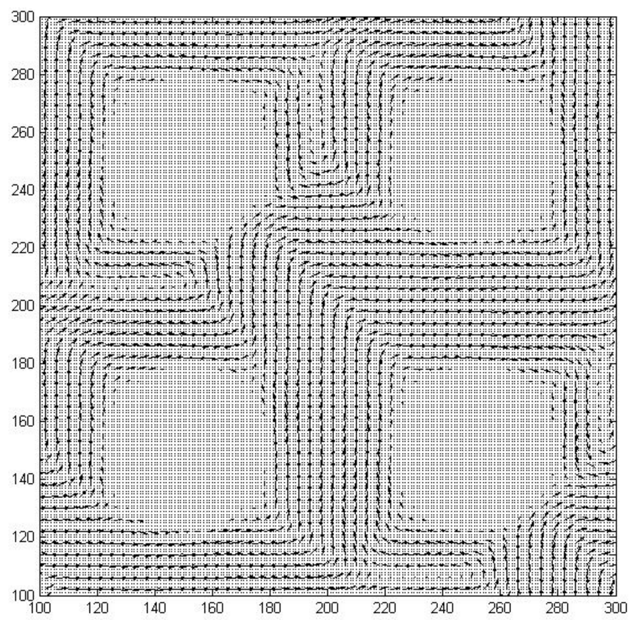

Figure 10

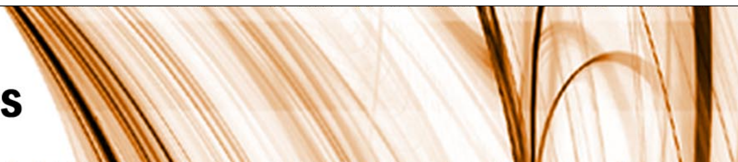

Thickness driven stabilization of saw-tooth–like domains upon phase transitions in ferroelectric thin films with depletion charges

I. B. Misirlioglu, H. N. Cologlu, and M. Yildiz

Citation: J. Appl. Phys. **111**, 064105 (2012); doi: 10.1063/1.3691938
View online: http://dx.doi.org/10.1063/1.3691938
View Table of Contents: http://jap.aip.org/resource/1/JAPIAU/v111/i6
Published by the American Institute of Physics.

Related Articles

Correlation between growth dynamics and dielectric properties of epitaxial BaTiO3 films
Appl. Phys. Lett. 100, 102904 (2012)

Strong red emission in lead-free ferroelectric Pr3+-doped Na0.5Bi0.5TiO3 thin films without the need of charge compensation
J. Appl. Phys. 110, 034102 (2011)

Influence of thermal stresses on the electrocaloric properties of ferroelectric films
Appl. Phys. Lett. 98, 132907 (2011)

Antiphase boundaries in Ba0.75Sr0.25TiO3 epitaxial film grown on (001) LaAlO3 substrate
Appl. Phys. Lett. 98, 091910 (2011)

Effects of electron irradiation on the ferroelectric 180° in-plane nanostripe domain structure in a thin film prepared from a bulk single crystal of BaTiO3 by focused ion beam
J. Appl. Phys. 109, 014104 (2011)

Additional information on J. Appl. Phys.

Journal Homepage: http://jap.aip.org/
Journal Information: http://jap.aip.org/about/about_the_journal
Top downloads: http://jap.aip.org/features/most_downloaded
Information for Authors: http://jap.aip.org/authors

ADVERTISEMENT

Downloaded 22 Mar 2012 to 193.255.135.1. Redistribution subject to AIP license or copyright; see http://jap.aip.org/about/rights_and_permissions

Thickness driven stabilization of saw-tooth–like domains upon phase transitions in ferroelectric thin films with depletion charges

I. B. Misirlioglu,[a] H. N. Cologlu, and M. Yildiz
Faculty of Engineering and Natural Sciences, Sabanci University, Tuzla/Orhanli, Istanbul 34956, Turkey

(Received 5 October 2011; accepted 4 February 2012; published online 22 March 2012)

Ionized impurities have nearly always been neglected in discussing the limit of functionality of ferroelectric thin films. One would certainly expect that the thickness limit for functionality would be altered in the presence of ionized impurities, but how this would occur remains unclear. In this article, we analyze the domain structures as well as the phase transition temperatures in films with depletion charges for various film thicknesses. Depletion charges induce a position-dependent built-in field that leads to an inhomogeneous distribution of ferroelectric polarization. Such an inhomogeneity in the polarization results in strong depolarizing fields in films. We show that formation of saw-tooth–type domains is a way to circumvent the depolarizing fields, even in films with ideal electrodes. There is a critical film thickness above which the saw-tooth domains develop. On the other hand, the phase transition of the ultrathin structures with electrodes having a finite screening length, namely real electrodes, is always into the multidomain state during cooling from the paraelectric state, regardless of the presence of depletion charges. An important finding we have is that the transition temperature in films with real electrodes does not depend nearly at all on the depletion charge density unless it is very high ($>10^{26}$ ionized impurities/m^3). Relatively thick films (>8 nm in this work) with real electrodes that have very high depletion charge densities have transition temperatures very similar to those with the same charge density, but with ideal electrodes, making us conclude that thick films with high depletion charge densities will hardly feel the finite screening effects. The results are provided for (001) $BaTiO_3$ films grown on (001) $SrTiO_3$ substrates with pseudomorphic top and bottom metallic electrodes. *© 2012 American Institute of Physics*. [http://dx.doi.org/10.1063/1.3691938]

I. INTRODUCTION

The intrinsic limit of ferroelectricity in thin films has been a topic of extensive discussions in many reports. A strained, planarly confined, thin ferroelectric (FE) structure exhibits dramatic changes in the dipole configurations commensurate with strong deviations from bulk states. One fact is that the formation of defects, such as ionic vacancies, interstitials, and dislocation networks, are inevitable, owing to both the process conditions and the developing strains in the film on misfitting substrates during fabrication. The defect fields and their impact on the physical properties of FEs both in bulk and film form have been the focus of numerous studies, including dedicated book chapters.[1–14] It has been well understood that the vacancy or impurity-type point defects lead to a depletion zone upon formation of the metal-film contact during electroding. The motivation to study such material systems has been to understand the limit of existence of ferroelectricity as a function of thickness and electrode-interface conditions, particularly focusing on depolarizing field effects.[15–25] A recent study, for example, based on a first principles approach, reports that a possible asymmetry in the material type for the top-bottom film electrode contacts could compete with the depolarizing effects through an internal bias field and reduce the critical thickness of a switchable ferroelectric polarization's existence to about two unit cells.[26] Besides applications in nano-scale memory devices, field effect transistors, and tunable layers in integrated circuits,[4,24,27] these materials have also become a test bed in the past few decades for studying phase transitions and critical behavior in the solid state, probably only second to magnetic materials.

Fabrication of these systems in capacitor geometries naturally results in the equilibration of the chemical potential at the metal-ferroelectric interfaces in ferroelectric films that often have impurity states, and the formation of a charged region on the film side is nearly inevitable. This has been mostly analyzed experimentally in addition to a few theoretical studies,[11,28–31] including attempts in artificially graded structures.[32] As will be shown, the depletion charge itself acts as a source of inhomogeneity and the situation is not very different from introducing compositional gradients to the system. Recently, several works have been devoted to especially understand the evolution of these charges under limited lattice diffusivities, but how such phenomena will be impacted by size effects remain an important aspect to be understood.[33,34] Furthermore, it is well known that charged defects, such as impurities and vacancies, will be quite immobile at temperatures near room temperature (RT) and might get populated at interfaces and defect sites probably only after several thousands of applied field cycles.[7,35]

In a real ultrathin ferroelectric film, due to the very short distances at which potential drops occur, it becomes very

[a]Author to whom correspondence should be addressed. Electronic mail: burc@sabanciuniv.edu.

 © 2012 American Institute of Physics

Downloaded 22 Mar 2012 to 193.255.135.1. Redistribution subject to AIP license or copyright; see http://jap.aip.org/about/rights_and_permissions

crucial to elaborate the interaction between depletion charges and the consequences of the extent of screening at the film-electrode interface. Film thicknesses at the order of a few tens of nanometers are comparable to the depletion zone widths expected in ferroelectric films, with metallic electrodes inducing a depletion potential of around 1 V. For typical densities of impurities (between 10^{24} and 2×10^{26}) we consider in this paper, we estimate depletion widths of around 100 nm to around 8 nm at each electrode interface. As the total of these depletion width values at each interface are quite close to the film thickness ranges of interest in our work, we assume fully depleted films when stated, particularly when finding the phase transition temperatures. The discussion on the effect of partial depletion on the domain structures is an exception to the full depletion assumption, but we show that the two situations are not very different for films not thicker than 28–30 nm. Depletion widths of around 30 nm and ionized impurity densities of around $10^{25-27}/m^3$ have been reported by Pintilie *et al*. using interfacial capacitance measurements for $PbZr_{0.2}Ti_{0.8}O_3$ films.[36,37]

The attempts to clarify the depletion charge effects have mostly been confined to very simple charge distributions as analysis of realistic distributions, even when depletion charge density is homogeneous, via analytical approaches can become a formidable problem. Only a few studies exist that try to analyze the effects of continuous depletion charge distributions on the observable properties in relatively thick films[7,38–41] but these studies have considered the single domain states. The possibility that, due to the inhomogeneous nature of the system owing to depletion charges, the transition could be into multidomain states even in structures with ideal electrodes would make a prominent difference in the calculated transition temperatures, which is one of the main emphases given in this paper. The way in which phase transition characteristics would be altered is discussed rigorously by Bratkovsky and Levanyuk[29] in the absence of dead layers. Reduction in the critical temperature commensurate with smaller coercivities in the ferroelectric state was demonstrated along with a qualitative discussion on the possibility of domain formation. One could easily foresee that the conclusions withdrawn for systems with ideal electrodes will have to be modified, for instance, for systems that have imperfect film-electrode interfaces, namely real electrodes. The real electrodes with finite Thomas-Fermi screening can be modeled as a thin dead layer between the electrode and the FE film, as demonstrated by Bratkovsky and Levanyuk in their 2009 paper (See Ref. 29). This latter statement is indeed a very important one when discussing experimental results on ferroelectric stability in the light of electrostatic considerations.

In this article, we address the question as to whether or not depletion charge effects could compete and overwhelm dead layer effects due to conditions at the film-electrode interfaces. To probe the competing energies, we use the Landau-Ginzburg-Devonshire (LGD) formalism for ferroelectric materials coupled with the interface conditions and presence of depletion charges. Firstly, films of various thicknesses with perfect film-electrode interfaces, namely ideal electrodes, but with depletion charges, are analyzed. A saw-tooth–type domain structure forms in relatively thick films due to the inhomogeneous internal field. At the transition temperature, thick films with ideal electrodes, but high depletion charge density always exhibit the saw-tooth domains. The period of this domain structure grows with increasing film thickness. Following this analysis, we introduce thin dead layers at the film-electrode interfaces to find out the possible alterations to the domain configurations and sensitivity of the domains to thickness effects. We found out that the domain period in a film having dead layers is altered upon introduction of a homogeneous depletion charge density to the system. At high depletion charge densities, domains with a saw-tooth type structure develop regardless of the presence of the dead layers. We also show that the transition temperatures are significantly lowered in relatively thick films with high depletion charge densities and dead layers, while this lowering is minimal in the thinner films and remain nearly unchanged with respect to charge-free films with dead layers. This behavior is a direct consequence of the dead layer effects dominating at low thicknesses, while thicker films are under a heavier influence of depletion charges. Our results reveal the magnitudes of changes that can be expected in the transition temperatures for films with depletion charges, considering, especially, the transition into multidomain states.

II. THEORY AND METHODOLOGY

In this section, we give the governing equations and boundary conditions used to obtain field- and temperature-dependent characteristics of the ferroelectric thin film capacitors. The schematic of the geometry considered is given in Fig. 1. A two-dimensional grid is constructed that has $200n \times kn$ cells, where $k(n)$ is the number of cells along the film thickness (width) and each cell has a dimension of 0.4 nm, nearly the lattice parameters of well-known pseudocubic perovskites, such as $BaTiO_3$ (BT), to imitate the order of lengths at which P can vary in the system compared to real systems. Polarization is obtained by solving the equations of state derived from the LGD free energy for all P in our system for an epitaxial monodomain (001) BT

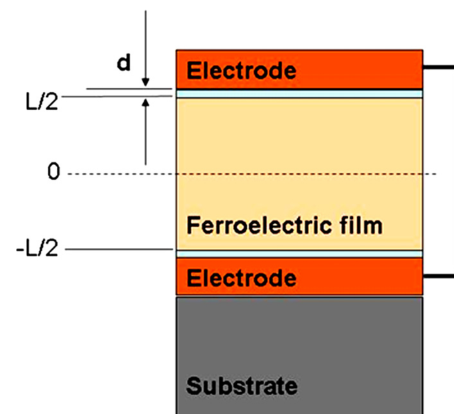

FIG. 1. (Color online) The schematic of the ferroelectric capacitor considered in this study.

Downloaded 22 Mar 2012 to 193.255.135.1. Redistribution subject to AIP license or copyright; see http://jap.aip.org/about/rights_and_permissions

ferroelectric film on a (001) $SrTiO_3$ cubic substrate along with the Maxwell equation for dielectric displacement, employing a finite difference discretization. The strain states of the films determine the stable P components. We partition the thin film capacitor system along the thickness axis, z, as follows:

$$w = 1 \quad \text{when} \quad -h/2 \leq z \leq +h/2, \quad w = 0 \quad \text{when} \quad -h/2 - d < z < -h/2 \quad \text{and} \quad +h/2 < z < d + h/2, \tag{1}$$

where w is a step-wise function defining the interface between the dead layer and the ferroelectric, d is the dead layer thickness (taken as 1-unit cell-thick, ~0.4 nm in this work), and $|h|$ is the thickness of the ferroelectric layer. The electrode-dead layer interfaces are at $-h/2 - d$ and $d + h/2$, respectively. Note that $d = 0$ indicates the absence of a dead layer, i.e., a perfect film-electrode contact interface. The equations of state for the system to define the relation between the fields in the layers and the P components as well as ε_r of the dead layers using the definition of w in Eq. (1) are

$$w\left[2\alpha_3^m P_3 + 4\alpha_{13}^m P_3 P_1^2 + 4\alpha_{33}^m P_3^3 + 6\alpha_{111} P_3^5 + \alpha_{112}(4P_3P_1^4 + 8P_3^3P_1^2) + 2\alpha_{123}P_3P_1^4 - G\left(\frac{\partial^2 P_3}{\partial z^2} - \frac{\partial^2 P_3}{\partial x^2}\right)\right] + (1-w)\frac{D_3}{\varepsilon_r\varepsilon_0} = wE_3^F + (1-w)E_3^d, \tag{2a}$$

$$w\left[2\alpha_1^m P_1 + 2(2\alpha_{11}^m + \alpha_{12}^m)P_1^3 + 2\alpha_{13}^m P_1 P_3^2 + 6\alpha_{111}P_1^5 + 2\alpha_{112}[3P_1^5 + 3P_1^3P_3^2 + P_1P_3^4] + 2\alpha_{123}P_1^3P_3^2 - G\left(\frac{\partial^2 P_1}{\partial z^2} + \frac{\partial^2 P_1}{\partial x^2}\right)\right] + (1-w)\frac{D_1}{\varepsilon_r\varepsilon_0} = wE_1^F + (1-w)E_1^d, \tag{2b}$$

where P_i ($i = 1,3$) are the components of P in the ferroelectric state, α_3^m, α_{13}^m, α_{33}^m, α_1^m, α_{11}^m, and α_{12}^m are the renormalized dielectric stiffness coefficients modified by the misfit strain and the two-dimensional clamping of the film, while α_{111}, α_{112}, and α_{123} are the dielectric stiffness coefficients in the bulk,[42] and G is the gradient energy coefficient and is assumed to be isotropic for convenience with a value of 3×10^{-10} m^3/F. E_3^F, E_1^F and E_3^d, E_1^d are the fields along the z- and x-axis in the ferroelectric layer and the dead layer, respectively. The equality between the field and the dielectric displacement in the dead layer ($w = 0$) reads

$$D_3 = \varepsilon_r\varepsilon_0 E_3^d \quad \text{and} \quad D_1 = \varepsilon_r\varepsilon_0 E_1^d \tag{3}$$

and, for $w = 1$ (ferroelectric layer),

$$D_3 = \varepsilon_b\varepsilon_0 E_3^F + P_3 \quad \text{and} \quad D_1 = \varepsilon_b\varepsilon_0 E_1^F + P_1. \tag{4}$$

The dead layer, when present, is assumed to be a high-k dielectric, whose dielectric constant, ε_r, is 20 to exemplify its effects and ε_b is the background dielectric constant of the ferroelectric (taken as 7 in this work[43]). The electric fields in both the ferroelectric layer and the dead layer are computed from the gradients of the electrostatic potential from

$$E_3^F = -\frac{\partial \phi^F}{\partial z}, \quad E_1^F = -\frac{\partial \phi^F}{\partial x} \tag{5}$$

for the ferroelectric and

$$E_3^d = -\frac{\partial \phi^d}{\partial z}, \quad E_1^d = -\frac{\partial \phi^d}{\partial x} \tag{6}$$

in the dead layers, with ϕ^F and ϕ^d being the electrostatic potential in the ferroelectric and the dead layer, respectively. The electrostatic potential in each layer can be found at each point as a function of P and the dielectric constant of the dead layer using the Maxwell relation in the absence of free charges $\nabla \cdot \hat{\mathbf{D}} = 0$ and $\nabla \cdot \hat{\mathbf{D}} = \rho$ when depletion charges due to ionized impurities are present. ρ is the volumetric charge density (0 when no impurities are present). Thus, one has

$$\frac{\partial^2 \phi^F}{\partial z^2} + \frac{\partial^2 \phi^F}{\partial x^2} = \frac{1}{\varepsilon_b\varepsilon_0}\left(\frac{\partial P_3}{\partial z} + \frac{\partial P_1}{\partial x} - \rho\right) \tag{7}$$

in the ferroelectric layer and

$$\frac{\partial^2 \phi^D}{\partial z^2} + \frac{\partial^2 \phi^d}{\partial x^2} = -\frac{\rho}{\varepsilon_r\varepsilon_0} \tag{8}$$

for the dead layer. We assume that each impurity contributing to ρ has only one positive unit charge (the charge of one electron) in all cases. The depletion charge density in this work, both in full and partial depletion cases, is assumed to be constant throughout the film volume, which is indeed realistic enough, especially for thicknesses at the order of a few tens of nanometers (See Refs. 30, 36, and 37), where full depletion is possible. The boundary conditions we employed for $P_{1,3}$ are

$$\left[P_1 + \lambda\frac{\partial P_1}{\partial z}\right]_{z=-\frac{h}{2},\frac{h}{2}} = 0, \quad \left[P_3 + \lambda\frac{\partial P_3}{\partial z}\right]_{z=-\frac{h}{2},\frac{h}{2}} = 0, \tag{9}$$

Downloaded 22 Mar 2012 to 193.255.135.1. Redistribution subject to AIP license or copyright; see http://jap.aip.org/about/rights_and_permissions

at the top and bottom electrode-film interface of the ferroelectric, where the extrapolation length, λ, is taken as infinite. Periodic boundary conditions are used along the x-axis, i.e.,

$$P_3(z, x = 0) = P_3(z, x = L), P_1(z, x = 0) = P_1(z, x = L). \tag{10}$$

We apply Dirichlet boundary conditions in the electrostatic equations to solve P in the thin film capacitors. At the dead layer-electrode interfaces, $-h/2 - d$ and $h/2 + d$ ($d = 0$ corresponds to ideal electrodes), $\phi = 0$ corresponds to short-circuit boundary conditions between the electrodes. Figure 1 shows the geometry adopted. Note that the entire "capacitor system" is neutral as the charges from ionized impurities, whose density is ρ, accumulate on the electrodes, and, thus, the number of positive and negative charges are equal.

Equations of state [Eqs. (2a) and (2b)] along with the equations of electrostatics in [Eqs. (7) and (8)] using relations given in Eqs. (3) and (6) are solved simultaneously for P components employing a Gauss-Seidel iterative scheme subject to boundary conditions mentioned above in Eqs. (9) and (10). The simulations always start with small fluctuations of z and x components of P around zero that later on develop into the domain structure, depending on dead layer and film thickness. We limit ourselves to 10 000 iterations converging to a difference of about 10^{-8} between consecutive iterative P solution steps when ferroelectricity exists. Owing to the compressive in-plane misfit in (001) $BaTiO_3$ on (001) $SrTiO_3$ (about 2.5%), only P_3 is the spontaneous polarization that, in addition to when depletion charge exists, also contains the built-in polarization, P_b. Thus, from here onwards, the ferroelectric part of P_3 will be denoted as P_f and the built-in part as P_b. Note that, when $\rho = 0$, there is only one solution and it is $P_3 = P_f$.

III. RESULTS AND DISCUSSION

A. Room temperature domain structures when $d = 0$ (ideal electrodes)

We start discussing our results for three different film thicknesses, 12 nm, 16 nm, and 20 nm, with perfect film-electrode interfaces obtained at room temperature (RT), assuming that these films are fully depleted (Part of our results are also given in Ref. 44). This assumption can be justified by noting that, for instance, in the case of impurity densities around 10^{26}, one might expect depletion zone thickness of around 8–10 nm, depending on the dielectric constant attaining values around 100–200 in a typical ferroelectric at room temperature, which indicates a total depletion zone of 16 to 20 nm for a film with top and bottom electrodes if the interfaces are symmetric. Structures with depletion charge at the max density limit considered in our work (2×10^{26} ionized impurities/m^3) that are thinner than 10-nm thickness are nearly always found to exist in an imprinted single domain state and are not of interest here. The reason for this outcome is discussed in the proceeding paragraphs. The films without any depletion charge also exist in a homogeneous monodomain state and are not discussed here again for brevity. In general, throughout this work, we chose to study two different depletion charge densities that reflect moderate-high and very high impurity densities reported for such structures. Depletion charge densities as high as 10^{25-27} ionized impurities/m^3 were reported,[31] and we remain around these (5×10^{25} ionized impurities/m^3 for the moderate-high limit and 2×10^{26} for the high limit) values in our simulations.

Figure 2 displays the domain structures that form in films of various thicknesses that have a fixed volumetric depletion charge density corresponding to 2×10^{26} ionized impurities/m^3. Upon finding that low densities of depletion charge yield only a unidirectional P_f in thin films, we focus on the densities that do trigger domains in thick structures (>10 nm). As a comparison, for example, the 8-nm-thick film with the aforementioned depletion charge density (2×10^{26} ionized impurities/m^3) does not undergo a domain stabilization, owing to the "insufficient extent of inhomogeneity", meaning it is not thick enough for the built-in field to render a highly inhomogeneous structure considering full depletion. By inhomogeneous, we mean here the dependence of the local Curie temperature on the built-in electric field at that location. Extremely high densities of depletion charge (>10^{27} ionized impurities/m^3) could perhaps stabilize domains in thicker films (>28 nm) with ideal electrodes, but are out of the main scope of our study.

In Fig. 2, we give the total polarization along with the ferroelectric polarization, and the latter is obtained by subtracting P_b from P_3 for 12 nm, 16 nm, and 20 nm films. The P_b is found by running our calculations above the Curie point, as it is nearly temperature insensitive and is the only corresponding solution satisfying Eqs. (2a), (7), and (8) [please see Fig. 3(a) for P_b when full depletion is assumed for a 20-nm film]. At 2×10^{26} ionized impurities/m^3, a saw-tooth–type domain pattern develops at RT, whose period is a function of thickness. Relatively lower depletion charge densities (<10^{26} ionized impurities/m^3) do not tend to stabilize domains and result in a uniaxial P_f whose amplitude is less in one half of the film than in the other half, concomitant

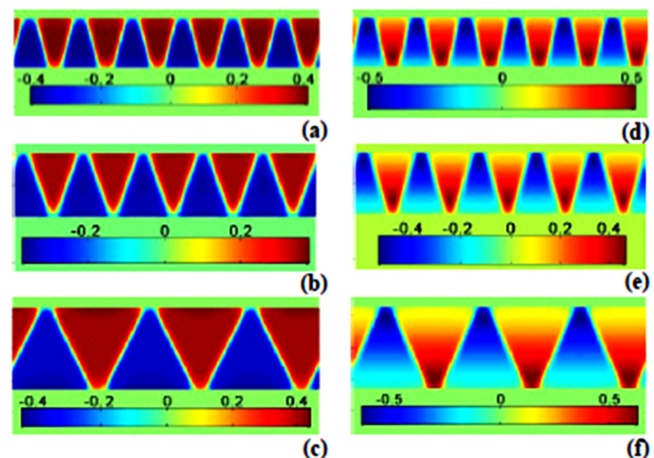

FIG. 2. (Color online) The RT domain total polarization configurations of the (a) 12-nm, (b) 16-nm, and (c) 20-nm-thick films with 2×10^{26} ionized impurities/m^3 (on the left-hand side) and the extracted ferroelectric polarization given for (d) 12-, (e) 16-, and (f) 20-nm-thick films on the right-hand side. Scales are given to display the range of P_3 in C/m^2.

Downloaded 22 Mar 2012 to 193.255.135.1. Redistribution subject to AIP license or copyright; see http://jap.aip.org/about/rights_and_permissions

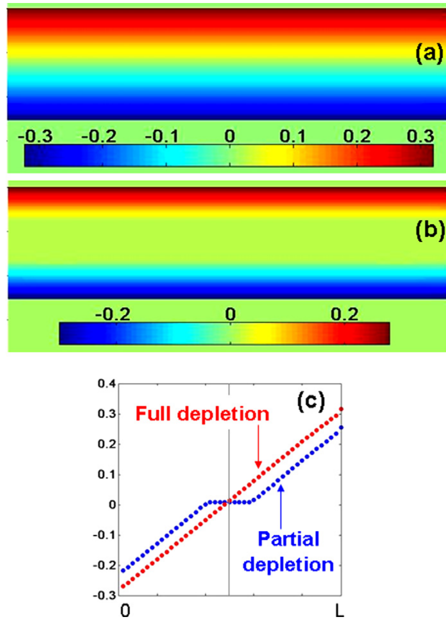

FIG. 3. (Color online) Schematic of the built-in field plotted as a function of position along the thickness of the ferroelectric film for a 2×10^{26} impurity/m^3 charge density in the case of (a) full depletion, (b) partial depletion, and (c) comparison of the built-in polarization along the thickness of full and partial depletion cases.

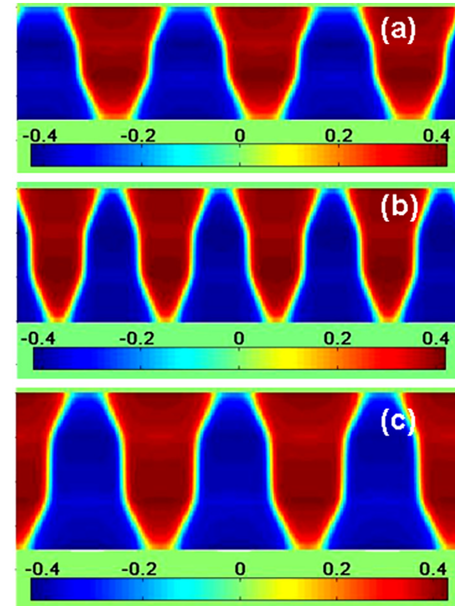

FIG. 4. (Color online) Domain structures in the case of (a) 20-nm, (b) 24-nm, and (c) 28-nm-thick films for partial depletion consideration for a 2×10^{26} impurity/m^3 charge density. The depleted layers are 8-nm-thick into the film starting from the film-electrode interfaces.

with the internal field distribution. Therefore, the formation of domains in thicker films is due to the highly inhomogeneous nature of the built-in field renormalizing the linear term in P_3 in Eq. (2a). Here, the amplitude of the variation in the local transition temperature naturally becomes more profound toward the film boundaries, with increasing thickness for a given constant charge density. The situation described that applies to our analysis is also schematically depicted in Figs. 3(a)–3(c) for clarity. Hence, thicker structures are forced to undergo domain stabilization to minimize the depolarizing fields emanating from the gradient of the polarization induced by the inhomogeneous built-in field. The domain period in such a high inhomogeneous system becomes a function of position, somewhat similar to what has been reported for discrete, artificially graded structures,[45] where the authors calculated domain fractions.

Those results reveal that the domain structures forming due to the depletion charge–induced fields in systems with ideal electrodes is quite different from what occurs when dead layers are present. For instance, in the latter, ferroelectric polarization amplitude attains a maximum in the middle section of the film, while saw-tooth–type domains have the maximum amplitude of the ferroelectric polarization wave near the electrode interfaces.

We find it important to add that, for depletion zone widths smaller, but comparable to film thickness where a charge-free region exists, we still see a similar behavior to a fully depleted film. P_b in the case of partial depletion is provided in Figs. 3(a)–3(c) for a 20-nm film with 8 nm depletion at each interface. If one carries out a more complete depletion width, w_d, calculation within the assumption that the ionized impurities have a constant density in the depletion zone using

$$w_d = \left[\frac{2\varepsilon_0\varepsilon_r(\phi_d - \phi_a)}{N_d q}\right]^{1/2} \quad (11)$$

for a dielectric constant of the ferroelectric (ε_r) being at the order of 200 and for the number of ionized impurities around 2×10^{26}/m^3, one finds that depletion width starting from the electrode-film interface is about 8 nm in the film. In Eq. (11), ϕ_d and ϕ_a are the depletion potential (or barrier from the metal side) and external applied potential, respectively, (zero when discussing w_d in this formulation). Domain structures far below the transition (room temperature) for the aforementioned partial depletion in the case of a 20-nm-thick film is provided in Fig. 4. For the full-depletion assumption, we had found that a saw-tooth–type domain configuration is stabilized. For a 20-nm-thick film, this would mean that there is a depleted region having a thickness of 2×8 nm = 16 nm at the interfaces, with a charge free region in the middle section. Our calculation shows that the saw-tooth domain structure is still present despite the charge-free region in the middle of the film, as given in Fig. 4 for 20-nm, 24-nm, and 28-nm-thick films. This behavior is quite straightforward to justify: The domains emanating at the interfaces where a strong built-in field exists do now want to terminate in the charge-free middle section with either a head-to-head or a tail-to-tail domain configuration, which is energetically costly. Moreover, the domain walls in the charge-free middle section are perpendicular to the film plane to minimize the total energy. In films with thickness being equal to or smaller than $2 \times w_d$, the situation converges to full depletion, already analyzed in this work.

For sufficiently thick films with high impurity density, the depletion zone in the film will be confined to a relatively small volume near the electrodes and the entire film could be

Downloaded 22 Mar 2012 to 193.255.135.1. Redistribution subject to AIP license or copyright; see http://jap.aip.org/about/rights_and_permissions

free from saw-tooth–type domains existing in a single domain state. Moreover, in the case of low impurity density and thicker films ($2 \times w_d \cong t$, where t is film thickness), a domain-forming built-in field might not be expected, but the built-in field will shift the hysteresis along the field axis and smear the transition anomalies, as demonstrated in a previous work,[39] as well as reducing the Curie temperature.

B. Room temperature domain structures when $d = 1$ (dead layers present)

In the presence of dead layers ($d = 1$ unit cell) and depletion charge, a competition between the two formations, each of which is a source of inhomogeneity, takes place. Here, we focus on fully depleted films with dead layers. A set of structures at RT for three different thicknesses and two depletion charge densities are provided in Fig. 5. The left-hand side gives the domain structure in the absence of depletion charge, while the right-hand side is when depletion charge is present. Subtracting the P_b at each site from P_3, we again get the P_f, as we did in Subsection III A. Among the analyzed structures, relatively moderate density of depletion charge (5×10^{25} ionized impurities/m^3 in this work) slightly alters the domain wall angles with respect to the film normal along with a period change, as will be discussed next. A charge density of 2×10^{26} stabilizes the saw-tooth domain structure that has the prominent maxima in the P_f profile at the domain tips, similar to the case when $d = 0$. Such a formation indicates that thick films with high depletion charge densities are under "weaker influence" of the dead layers. Another effective way to enable the comparison of the domain periods in films with and without depletion charge for a given thickness would be to plot and discuss the wave vector k of domains ($k = 2\pi/\lambda$, where λ is domain period) as a function of thickness, as we do in the preceding paragraphs.

Before discussing the probable changes in domain period when depletion charges are present in thin films, we give the results for the domain wave vector, k, we obtained both in our simulations and using the approach presented in Ref. 46 to validate the trends of our simulations for charge-free films in Fig. 6(a). A summary of the approach in Ref. 46 in a modified form (see also Ref. 47) is given in the Appendix for convenience. Our numerical results are in excellent agreement with the results obtained using the methodology in the Appendix, confirming the reliability of the method. Note the approach in the Appendix adopted from Refs. 46 and 47 analyzes the phase transition point, considering linear equation of state. We find that the domain period does not nearly change at all with further cooling upon the transition from the paraelectric to the multidomain FE state and transforms from a sinusoidal pattern to a square-like one, making it feasible to compare k values at and below the transition. In other words, even when our simulation temperatures are not the same as the

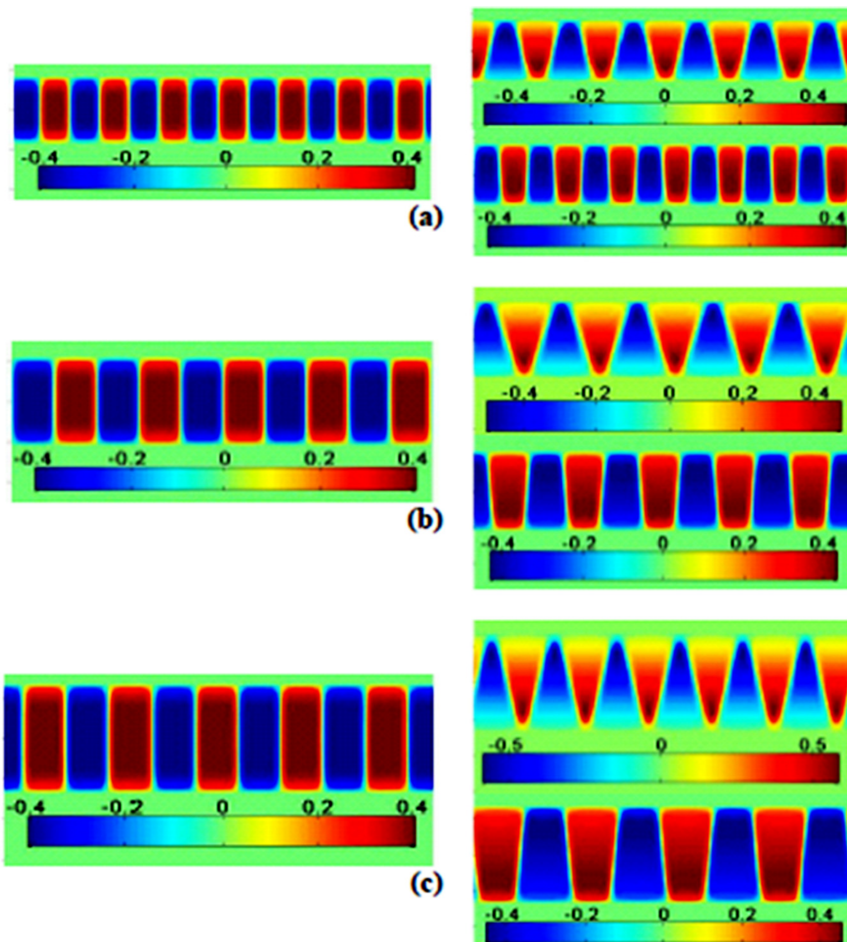

FIG. 5. (Color online) Domain structures for (a) 12-nm, (b) 16-nm, and (c) 20-nm-thick films with dead layers. On the left-hand side are the domain structures for 0 impurity density and $d = 1$. The right-hand side of each color map for a given thickness are the domain structures for impurity densities of 5×10^{25} (upper color map) and 2×10^{26} (lower color map). Scales are given to display the range of P_3 in C/m^2.

Downloaded 22 Mar 2012 to 193.255.135.1. Redistribution subject to AIP license or copyright; see http://jap.aip.org/about/rights_and_permissions

temperatures at which the k values were found using the approaches in Refs. 46 and 47, the k's in both their study and our simulations are directly comparable.

To visualize the impact of depletion charge on the domain structures in films with dead layers, we now discuss behavior of the wave vector, k, of the P_f wave plotted as a function of film thickness for ionized impurity densities of 5×10^{25} and 2×10^{26} /m^3. Our results for films at RT without and with depletion charge are in Fig. 6(b). The presence of electrical domains in films with depletion charge has persisted for the entire thickness range of interest in our study. Domain period for films thinner than 12 nm with 5×10^{25} ionized impurities/m^3 is smaller than the charge-free film, while 2×10^{26} ionized impurities/m^3 follows more or less the charge-free film, but with slightly larger k values (i.e., smaller domain period). The general trend of the increase in k values for films thinner than 12 nm in our work might be perceived as an indication that the depletion charge amplifies the depolarizing field for a given set of material parameters (domain wall energy, fixed dead layer thickness, dielectric constant, etc.). But this trend changes with increasing film thickness for the films having 5×10^{25} ionized impurities/m^3 with respect to the charge-free case. Around 15 nm, a crossover occurs, after which the thicker films with 5×10^{25} ionized impurities/m^3 carrier density develop a coarser domain structure. Here, from the data of our simulations, we can see that the domain period is altered in a way the depolarizing field appears to be amplified, leading to a finer domain period, hence, a larger k. Still, we cannot arrive at general conclusions for the entire thickness regime we considered, as thicker films (>16 nm) with moderate-high depletion charge density have a distinctly different domain period. Despite the thought that any formation giving rise to or amplifying depolarizing fields will reduce the transition temperature, comparing the k values for a given thickness does not lead us to conclude so. To analyze the effect of depletion charge effects on the transition temperature, we carry out cooling runs in our simulations and extract and discuss the transition temperatures in Subsection III C.

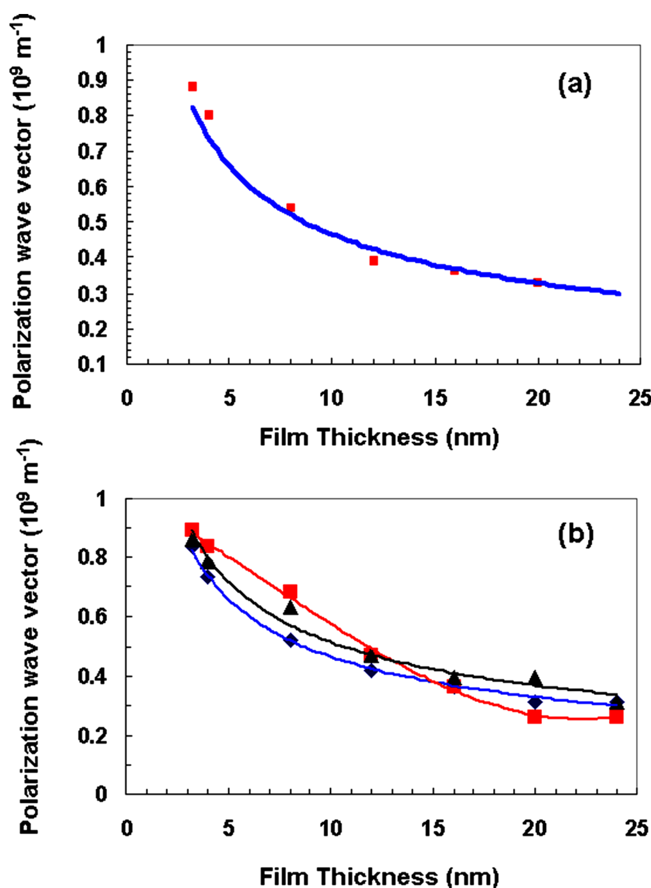

FIG. 6. (Color online) (a) Wave vector of the polarization along the film plane as a function of film thickness at the transition derived from solving Eq. (A16) for the point of loss of stability of the paraelectric phase summarized in the Appendix (solid curve) and the wave vector we found in our simulations (solid squares) for $d = 1$ unit cell. (b) Wave vector of the polarization along the film plane as a function of thickness for films without charge (curve with diamonds), films having 5×10^{25} ionized impurities/m^3 charge density (curve with squares), and films having 2×10^{26} ionized impurities/m^3 charge density (curve with triangles) for $d = 1$ unit cell. The curves in (b) passing through the data points are guides for the eyes.

C. Phase transition temperatures

This section considers the case of films where the entire volume is depleted, as we note that a further detailed discussion might be necessary to compare partial depletion and full depletion effects for various impurity densities. Furthermore, for asymmetrical film-electrode interfaces, it is clear that such effects might be altered significantly. We had already mentioned, for symmetrical film-electrode interfaces, that films with high impurity densities, where the depletion zones are confined to the near-electrode region, can exist in a single domain state and the transition temperatures will set accordingly. We leave this comparison for future work and focus on films with depletion zones being at the order of the film thickness, i.e., full depletion. The paraelectric-ferroelectric transition temperatures for films with full depletion are expected to be lowered in the presence of depletion charges, dead layers, or when both coexist. Film thickness importantly comes into play in all of the cases above (See Figure 7). Here, we emphasize the situation when dead layers and depletion charges are both present, but also run a case where the films at a thickness range of 3.2 nm to 24 nm have ideal electrodes for comparison. For reference, we first computed the transition temperature as a function of film thickness for a fixed dead layer thickness ($d = 1$) and dielectric constant (ε_r = 20) and our results are in Fig. 7(a) along with the results we obtained using the method prescribed in the Appendix. We find the transition temperatures by tracking $\langle |P_3| \rangle$ in our simulations. The transition temperatures computed from the numerical solution of Eq. (16a) in the Appendix have a very good match with the simulation results presented in this work, again confirming the validity of the prescribed method in Sec. II (Figure 7(a)). It must be borne in mind that the approach of Ref. 45 excludes the gradient of P_3 (total polarization) along the thickness of the film, which we do include in our study. This can be the possible cause of the slight deviation between the two results at small thicknesses. As expected, decreasing film thickness results

Downloaded 22 Mar 2012 to 193.255.135.1. Redistribution subject to AIP license or copyright; see http://jap.aip.org/about/rights_and_permissions

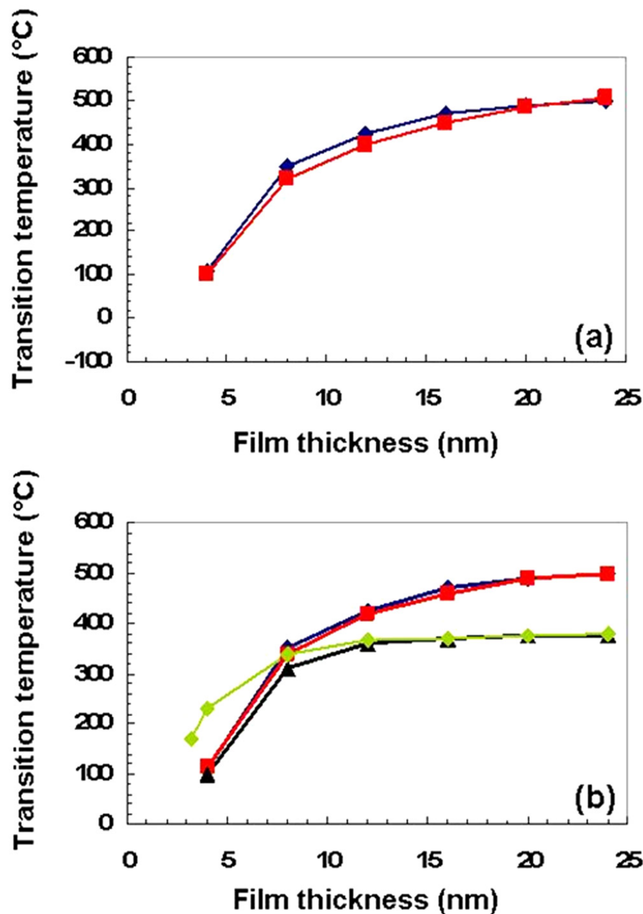

FIG. 7. (Color online) (a) Phase transition temperatures in films with dead layers as a function of thickness when (a) no charge is present. The curve with diamonds is the results of our simulations, and the curve with squares is the results obtained by solving Eq. (A16) in the Appendix after Ref. 43. (b) Comparison of the results for charge-free (curve with diamonds) films having 5×10^{25} ionized impurities/m^3 depletion charge (curve with squares) and films having 2×10^{26} ionized impurities/m^3 depletion charge (curve with triangles), and the curve with triangles is the case for $d = 0$ (no dead layer) and 2×10^{26} ionized impurities/m^3 depletion charge given for comparison. Note that, in (b), the curve with squares and the curve with the solid dark diamonds have a strong overlap, where the latter is just partially visible.

in a reduction of the transition temperature, with domain period subsequently becoming comparable or larger than the film thickness. Note that we do not go down to very low temperatures, where ultrathin films (<3.2 nm in this work) might be in a single domain state upon transition from the paraelectric phase and that this takes place at quite low temperatures.

Computing the phase transition temperatures in films with dead layers, but now with two different depletion charge densities, we note that films with a charge density of 5×10^{25} ionized impurities/m^3 have nearly the same transition temperature compared to the charge free ones for a given thickness [see Fig. 7(b)]. Note that a homogeneous charge distribution does not lead to any net bias fields between the electrodes, and no smearing of the transition exists, meaning the transition temperature is sharp. We then carried out the cooling runs for films having a depletion charge density of 2×10^{26} ionized impurities/m^3 both in the presence and absence of dead layers to detect the transition. As mentioned previously, tracking $\langle |P_3| \rangle$ and comparing it with $\langle P_3 \rangle$ allows us to detect the phase transition, if it is into a multidomain state. These films with 2×10^{26} ionized impurities/m^3 and dead layers have a similar trend with the charge-free films at small thickness, but then the transition temperature is significantly reduced for thicker films. Moreover, the transition temperatures in thicker films with and without dead layers are nearly the same. This scenario is certainly different for thinner films (<12 nm), and it is seen that the dead layers entirely dominate the transition characteristics [compare the curves for the films having 2×10^{26} ionized impurities/m^3 with and without dead layers in Fig. 7(b)]. This is solely due to the "degree of induced inhomogeneity" in the thicker films, where the built-in electric field due to depletion charges induce a strong gradient of the transition temperature via normalization of α_3^m in Eq. (2a), causing a larger amplitude variation of P_f, possibly overriding dead layer effects. Therefore, we provide quantitative evidence that the thicker films will be under a stronger influence of the depletion charge effects compared to thinner ones. One must remember here, however, that we discuss the case of rather high densities of depletion charge. For moderate-to-low densities (<10^{25} ionized impurities/m^3 in this work), the above discussion on transition temperatures merely converges to discussion of dead layer effects on the transition temperature as a function of film thickness.

IV. CONCLUSIONS

We have analyzed the phase transition characteristics of ferroelectric thin films with and without depletion charge, considering ideal electrodes and film-electrode interface with dead layers. Using the non-linear Landau-Ginzburg-Devonshire equation of state, simulations were carried out for films with different thicknesses at different temperatures to find the domain periodicities and transition temperatures as a function of depletion charge density at various thicknesses. The approach adopted from Refs. 46 and 47 has been used as a guide to check the validity of our simulation results. (001)$BaTiO_3$ grown on (001)$SrTiO_3$ with pseudomorphic electrodes was used as an example system. Films with high depletion charges split into saw-tooth–type domains, even when ideal electrodes are present. This happens when the film is above a critical thickness, below which a single domain, imprinted state is stabilized. Increase in film thickness naturally creates larger variations in the electric field, hence, in local transition temperatures, due to a constant density of depletion charge, and a saw-tooth–type domain structure is favored, even in films with ideal electrodes to minimize the depolarizing fields. Partially depleted films, when the depleted volume is comparable to the film volume, could still develop saw-tooth-type domains. The latter happens with the exception that the domain walls are parallel to the film normal to reduce domain wall energy. Presence of dead layers when depletion charge densities are not very high (<10^{26} ionized impurities/m^3) determine the transition temperature both for thin (<10 nm) and thick films (>10 nm). At charge densities not very high, domain periods are slightly altered, subsequent with tilted domain walls with

Downloaded 22 Mar 2012 to 193.255.135.1. Redistribution subject to AIP license or copyright; see http://jap.aip.org/about/rights_and_permissions

respect to domain configurations in charge-free films. Although high charge densities in films with dead layers stabilize saw-tooth–type domains, regardless of the presence of the dead layers, the fact that very thin films (<10 nm) exist in a fine period multidomain state as opposed to what happens in films with ideal electrodes reveals the domination of the dead layer effects in thin films. While transition temperatures of ultrathin films having depletion charge are set by the dead layers, high depletion charge densities (2×10^{26} ionized impurities/m^3 in this work) dominate over dead layer effects in thicker films. This can be judged by comparing the very similar results for these films with and without dead layers, i.e., the relatively thicker films with high depletion charge densities and dead layers have identical transition temperatures as those with the same depletion charge density, but ideal electrodes.

ACKNOWLEDGMENTS

I.B.M. has been partially supported by Turkish Academy of Sciences (TÜBA) through the GEBİP Program.

APPENDIX: ANALYTICAL TREATMENT OF THE SYSTEM NEAR THE TRANSITION TEMPERATURE

The system analyzed in Ref. 46 is already given in Fig. 1. The approach in Ref. 46 is based on finding the point of loss of stability of the paraelectric phase for a ferroelectric slab with dead layers. While the system in Ref. 46 is treated in one half of the film with dead layers as being vacuum and the film being very thick compared to the dead layers, this approach was generalized in Ref. 47, and we follow this general approach by full treatment of the film with high-k dead layers. Going back to the system in Fig. 1, for a given dead layer thickness, d (1 $BaTiO_3$ unit cell thick, $\sim$0.4 nm, in this work), the boundary conditions of the system can be written as

$$D_F^z - D_d^z = 0 \,@\, z = \pm L/2, \tag{A1}$$

where $D_F^z = \varepsilon_b \varepsilon_0 E_z^F + P$ and $D_d^z = \varepsilon_z^d \varepsilon_0 E_z^d$ are the dielectric displacements in the FE and dead layers, respectively, with ε_0 being the permittivity of vacuum in International system of units (SI) units, ε_z^d is the dielectric constant of the dead layer, ε_b is the background dielectric constant of the FE, P is the ferroelectric polarization in the FE along the film thickness, and L is the FE film thickness (see Fig. 1). The boundary conditions for the potential are as follows:

$$\phi_F = \phi_d @ z = \pm L/2, \tag{A2a}$$

$$\phi_d = 0 @ z = L/2 + d, \tag{A2b}$$

$$\phi_d = 0 @ z = -L/2 - d, \tag{A2c}$$

where $\phi_{F,d}$ are the potentials in the FE and the dead layer, respectively. The electric fields in the layers can then be found from the gradient of the potentials. From Eq. (1), one gets

$$-\varepsilon_b \varepsilon_0 \frac{\partial \phi_F}{\partial z} + P - \varepsilon_0 \varepsilon_z^d \frac{\partial \phi_d}{\partial z} = 0 @ z = L/2. \tag{A3}$$

In the absence of free charges, $divD = 0$ both in the FE and the dead layers. Writing these conditions in terms of the potential and polarization in the FE film, we get

$$\frac{\partial^2 \phi_F}{\partial z^2} + \frac{\varepsilon_\perp}{\varepsilon_b} \frac{\partial^2 \phi_F}{\partial x^2} = \frac{1}{\varepsilon_b \varepsilon_0} \frac{\partial P}{\partial z}, \tag{A4}$$

where $\varepsilon_\perp$ is the dielectric constant of the FE along the plane of the film (calculated as approximately 40 from the simulations, and this value is used) and

$$\varepsilon_0 \left(\varepsilon_z^P \frac{\partial^2 \phi_d}{\partial z^2} + \varepsilon_\perp^P \frac{\partial^2 \phi_d}{\partial x^2} \right) = 0 \tag{A5}$$

for the dead layer. For convenience, it is assumed that the dead layer is isotropic and $\varepsilon_z^d = \varepsilon_\perp^d$, with $\varepsilon_\perp^d$ being the dielectric constant of the dead layer along the film plane. The linear equation of state of the FE that is obtained by minimization of the Landau-Ginzburg free energy with its lowest order terms is

$$AP - g \frac{\partial^2 P}{\partial x^2} = -\frac{\partial \phi_F}{\partial z}, \tag{A6}$$

where the gradient of P along z has been neglected, as mentioned above, $A = (T - T_C)/\varepsilon_0 C + M$, where T is temperature, T_C is the transition temperature in bulk form, C is the Curie constant, M represents any contribution of strain in the case of a FE on a substrate (see the modified coefficient of the lowest order term in P in the free energy in Ref. 36), and g is the gradient energy coefficient. Note that the energy due to gradients along z is much less than the gradients of P along x, allowing one to safely neglect gradients along z. To solve the polarization and the potential using the differential equations above together with the equation of state in the FE, one can use the Fourier transform to express the polarization and the potentials in the layers in terms of harmonics,

$$P = \sum_k P_k e^{ikx}, \phi_F = \sum_k \phi_F^k e^{ikx}, \phi_d = \sum_k \phi_d^k e^{ikx}, \tag{A7}$$

where P_k, ϕ_F^k, and ϕ_d^k are the z-amplitudes of each harmonic in k. Inserting these Fourier transforms for a given k into Eqs. (A4), (A5), and (A6), we get

$$\frac{\partial^2 \phi_F^k}{\partial z^2} + q^2 \phi_F^k = 0, \tag{A8}$$

$$\frac{\partial^2 \phi_d^k}{\partial z^2} - k^2 \phi_d^k = 0, \tag{A9}$$

where $q = (\varepsilon_\perp \varepsilon_b \varepsilon_0 k^2 |A + gk^2|)^{1/2}$. The solutions of Eqs. (A8) and (A9) that satisfy the boundary conditions (BCs) given in Eq. (A2) are

$$\phi_F^k = A cosqz + B sinqz, \tag{A10}$$

$$\phi_d^k = C \sinh k(z - L - d) + D \cosh k(z - L), \tag{A11}$$

Downloaded 22 Mar 2012 to 193.255.135.1. Redistribution subject to AIP license or copyright; see http://jap.aip.org/about/rights_and_permissions

where A, B, C, and the D are the amplitudes in the general solution. Using the BCs given in Eqs. (A1) and (A2c), we get two equations with two unknowns, B and C from Eqs. (A10) and (A11),

$$B\left[q\cos\frac{qL}{2}+\frac{q}{\varepsilon_b\varepsilon_0(A+gk^2)}\cos\frac{qL}{2}\right]-\varepsilon_z^d kC\cosh-\frac{kd}{2}=0, \tag{A12a}$$

$$B\sin\frac{qL}{2}-C\sinh-\frac{kd}{2}=0. \tag{A12b}$$

For a non-trivial solution to exist, the determinants of the coefficients in Eqs. (A12a) and (A12b) have to be zero, giving us

$$B\left[\sinh\frac{kd}{2}\left(q\cos\frac{qL}{2}+\frac{q}{\varepsilon_b\varepsilon_0(A+gk^2)}\cos\frac{qL}{2}\right)+\varepsilon_z^d k\cosh-\frac{kd}{2}\sin\frac{qL}{2}\right]=0, \tag{A13}$$

meaning that

$$\sinh\frac{kd}{2}\left(q\cos\frac{qL}{2}+\frac{q}{\varepsilon_b\varepsilon_0(A+gk^2)}\cos\frac{qL}{2}\right)+\varepsilon_z^d k\cosh-\frac{kd}{2}\sin\frac{qL}{2}=0. \tag{A14}$$

After some algebra on Eq. (14), one gets

$$\tan\frac{qL}{2}=\frac{\sqrt{|\varepsilon_k|\varepsilon_\perp}}{\varepsilon_z^d}\tanh\frac{kd}{2}, \tag{A15a}$$

where

$$|\varepsilon_k|=\left(\frac{1}{\varepsilon_0(A+gk^2)}+1\right), \tag{A15b}$$

which was previously obtained by the authors of Ref. 46 through a similar route. Their approach is somewhat repeated here for tractability of results in our paper. We solve Eq. (15) using a numerical approach and seek the k value that yields the highest transition temperature from the paraelectric state into the ferroelectric state for a given d (1-unit cell-thick in this work). We do not carry out the calculations in the single domain state regime, which correspond to thicknesses smaller than 3 nm and are outside the scope of our analysis. Also note that the described method is applied for the validation of the simulation results and do not reflect any depletion charge–related effects, which are separately given only by the numerical simulation presented in this paper.

[1]S. Triebwasser, Phys. Rev. **118**, 100 (1960).
[2]A. P. Levanyuk and A. S. Sigov, "Defects and structural phase transitions," in *Ferroelectricity and Related Phenomena*, edited by W. Taylor (Gordon and Breach, New York, 1988), Vol. 6.
[3]W. L. Warren, D. Dimos, G. E. Pike, B. A. Tuttle, M. V. Raymond, R. Ramesh, and J. T. Evans, Appl. Phys. Lett. **67**, 866 (1995).
[4]T. M. Shaw, S. Troiler-McKinstry, and P. C. Mcintyre, Annu. Rev. Mater. Sci. **30**, 263 (2000).
[5]R. Ramesh, S. Aggarwal, and O. Auciello, Mater. Sci. Eng. R. **32**, 191 (2001).
[6]C. S. Ganpule, A. L. Roytburd, V. Nagarajan, B. K. Hill, S. B. Ogale, E. D. Williams, R. Ramesh, and J. F. Scott, Phys. Rev. B **65**, 014101 (2002).
[7]H. Z. Jin and J. Zhu, J. Appl. Phys. **92**, 4594 (2002).
[8]M.-W. Chu, I. Szafraniak, R. Scholz, C. Harnagea, D. Hesse, M. Alexe, and U. Gösele, Nature Mater. **3**, 87 (2004).
[9]X. Ren, Nature Mater. **3**, 91 (2004).
[10]E. Cockayne and B. P. Burton, Phys. Rev. B **69**, 144116 (2004).
[11]A. N. Morozovska and E. A. Eliseev, J. Phys: Condens. Matter **16**, 8937 (2004).
[12]D. Balzar, P. A. Ramakrishnan, and A. M. Hermann, Phys. Rev. B **70**, 092103 (2004).
[13]S. P. Alpay, I. B. Misirlioglu, V. Nagarajan, and R. Ramesh, Appl. Phys. Lett. **85**, 2044 (2004).
[14]Y. Zheng, B. Wang, and C. H. Woo, Appl. Phys. Lett. **88**, 092903 (2006).
[15]I. P. Batra and B. D. Silverman, Solid State Commun. **11**, 291 (1972).
[16]R. Kretschmer and K. Binder, Phys. Rev. B **20**, 1065 (1979).
[17]A. M. Bratkovsky and A. P. Levanyuk, Phys. Rev. Lett. **84**, 3177 (2000).
[18]J. Junquero and P. Ghosez, Nature **422**, 506 (2003).
[19]Z. Q. Wu, N. D. Huang, Z. R. Liu, J. Wu, W. H. Duan, B. L. Gu, and X. W. Zhang, Phys. Rev. B **70**, 104108 (2004).
[20]D. J. Kim, J. Y. Jo, Y. S. Kim, Y. J. Chang, J. S. Lee, J. G. Yoon, T. K. Song, and T. W. Noh, Phys. Rev. Lett. **85**, 237602 (2005).
[21]G. Gerra, A. K. Tagantsev, N. Setter, and K. Parlinski, Phys. Rev. Lett. **96**, 107603 (2006).
[22]R. Ahluwalia and D. J. Srolovitz, Phys. Rev. B **76**, 174121 (2007).
[23]A. Artemev and A. Roytburd, Acta Mater. **58**, 1004 (2010).
[24]Y. Wang, M. K. Niranjan, K. Janicka, J. P. Velev, M. Y. Zhuravlev, S. S. Jaswal, and E. Y. Tsymbal, Phys. Rev. B **82**, 094114 (2010).
[25]Y. Zheng, M. Q. Cai, and C. H. Woo, Acta Mater. **58**, 3050 (2010).
[26]M. Q. Cai, Y. Zheng, P.-W. Ma, and C. H. Woo, J. Appl. Phys. **109**, 024103 (2011).
[27]N. G. Nathaniel, R. Ahluwalia, H. B. Su, and F. Boey, Acta Mater. **57**, 2047 (2008).
[28]M. Dawber, K. M. Rabe, and J. F. Scott, Rev. Mod. Phys. **77**, 1083 (2005).
[29]A. M. Bratkovsky and A. P. Levanyuk, Phys. Rev. B. **61**, 15042 (2000). For the treatment of real electrodes, see A. M. Bratkovsky and A. P. Levanyuk, J. Comp. Theor. Nanosci., 6, 465 (2009).
[30]H. Matsuura, New J. Phys. **2**, 8 (2000).
[31]Y. Xiao, V. B. Shenoy, and K. Bhattacharya, Phys. Rev. Lett. **95**, 247603 (2005).
[32]M. B. Okatan, J. V. Mantese, and S. P. Alpay, Acta Mater. **58**, 39 (2010).
[33]Y. Zhang, J. Li, and D. Fang, Phys. Rev. B **82**, 064103 (2010).
[34]L. Hong, A. K. Soh, Q. G. Du, and J. Y. Li, Phys. Rev. B **77**, 094104 (2008).
[35]M. Dawber and J. F. Scott, Appl. Phys. Lett. **76**, 1060 (2000).
[36]L. Pintilie and M. Alexe, J. Appl. Phys. **98**, 124103 (2005).
[37]L. Pintilie, I. Boerasu, M. J. M. Gomez, T. Zhao, R. Ramesh, and M. Alexe, J. Appl. Phys. **98**, 124104 (2005).
[38]P. Zubko, D. J. Jung, and J. F. Scott, J. Appl. Phys. **100**, 114112 (2006).
[39]I. B. Misirlioglu, M. B. Okatan, and S. P. Alpay, J. Appl. Phys. **108**, 034105 (2010).
[40]M. D. Glinchuk, E. A. Eliseev, and A. N. Morozovska, Ferroelectrics **354**, 86 (2007).
[41]M. D. Glinchuk, B. Y. Zaulychny, and V. A. Stephanovich, Phys. Status Solidi **243**, 542 (2006).
[42]N. A. Pertsev, A. G. Zembilgotov, and A. K. Tagantsev, Phys. Rev. Lett. **80**, 1988 (1998).
[43]J. Hlinka and P. Marton, Phys. Rev. B **74**, 104104 (2006); A. K. Tagantsev, Ferroelectrics **375**, 19 (2008).
[44]I. B. Misirlioglu and M. Yildiz, *Proceedings of IEEE ISAF/PFM in Vancouver*, Canada, July 24–27, 2011.
[45]M. B. Okatan, A. L. Roytburd, J. V. Mantese, and S. P. Alpay, J. Appl. Phys. **105**, 114106 (2009).
[46]E. V. Chensky and V. V. Tarasenko, Sov. Phys. JETP **56**, 618 (1982); Zh. Eksp. Teor. Fiz. **83**, 1089 (1982).
[47]A. S. Sidorkin, *Domain Structure in Ferroelectrics and Related Materials* (Cambridge International Science, Moscow 2006).

Downloaded 22 Mar 2012 to 193.255.135.1. Redistribution subject to AIP license or copyright; see http://jap.aip.org/about/rights_and_permissions